VISCOELASTIC–VISCOPLASTIC DAMAGE MODEL FOR ASPHALT CONCRETE

A Thesis

by

MICHAEL ANTHONY GRAHAM

Submitted to the Office of Graduate Studies of
Texas A&M University
in partial fulfillment of the requirements for the degree of

MASTER OF SCIENCE

August 2009

Major Subject: Civil Engineering

VISCOELASTIC–VISCOPLASTIC DAMAGE MODEL FOR ASPHALT CONCRETE

A Thesis

by

MICHAEL ANTHONY GRAHAM

Submitted to the Office of Graduate Studies of
Texas A&M University
in partial fulfillment of the requirements for the degree of

MASTER OF SCIENCE

Approved by:

Co-Chairs of Committee,	Rashid K. Abu Al-Rub
	Eyad Masad
Committee Members,	Anastasia Muliana
	Zachary C. Grasley
Head of Department,	David Rosowsky

August 2009

Major Subject: Civil Engineering

ABSTRACT

Viscoelastic–Viscoplastic Damage Model for Asphalt Concrete. (August 2009)

Michael Anthony Graham, B.S., Texas A&M University

Co-Chairs of Advisory Committee: Dr. Rashid K. Abu Al-Rub
Dr. Eyad Masad

This thesis presents a continuum model for asphalt concrete incorporating nonlinear viscoelasticity, viscoplasticity, mechanically-induced damage and moisture-induced damage. The Schapery single-integral viscoelastic model describes the nonlinear viscoelastic response. The viscoplastic model of Perzyna models the time-dependent permanent deformations, using a Drucker–Prager yield surface which is modified to depend on the third deviatoric stress invariant to include more complex dependence on state of stress. Mechanically-induced damage is modeled using continuum damage mechanics, using the same modified Drucker–Prager law to determine damage onset and growth. A novel moisture damage model is proposed, modeling moisture-induced damage using continuum damage mechanics; adhesive moisture-induced damage to the asphalt mastic–aggregate bond and moisture-induced cohesive damage to the asphalt mastic itself are treated separately.

The analytical model is implemented numerically for three-dimensional and plane strain finite element analyses, and a series of simulations is presented to show the performance of the model and its implementation. Sensitivity studies are conducted for all model parameters and results due to various simulations corresponding to laboratory tests are presented.

In addition to the continuum model, results are presented for a micromechanical model using the nonlinear-viscoelastic–viscoplastic–damage model for asphalt mastic

and a linear elastic model for aggregates. Initial results are encouraging, showing the strength and stiffness of the mix as well as the failure mode varying with moisture loading. These initial results are provided as a an example of the model's robustness and suitability for modeling asphalt concrete at the mix scale.

ACKNOWLEDGMENTS

I am incredibly grateful to the many people who helped me as I researched this topic and prepared this thesis. There are for too many to mention all of them, but I would like to thank several here.

I gratefully acknowledge the Southwest University Transportation Center for funding my research.

The guidance of my advisory committee co-chairs, Drs. Eyad Masad and Rashid Abu Al-Rub, has been beyond invaluable both for their technical expertise for this subject and their overall nurturing of me as an engineer and researcher. I would also like to thank Drs. Zachary Grasley and Anastasia Muliana, my other advisory committee members, who, like my chairs, were always available, helpful, and guiding.

I also wish to thank all my fellow researchers who helped me, four of whom I will mention. I truly value Silvia Caro's help and encouragement, teaching me so much of what I needed to know about asphalt concrete and encouraging me along the way. I thank Dr. Chien-Wei Huang, whose work served as a basis for mine presented here and whose help allowed me to understand it faster and better. Masoud Darabi was supportive, helpful, and very insightful—look forward to his work on this topic! I also appreciate the help of Sun-Myung Kim.

I would like to offer special thanks to Dr. Gordon Airey for providing us data from a wide range of mechanical tests performed on asphalt concrete, and Dr. Emad Kassem for providing his data for mechanical tests on dry and moisture-conditioned asphalt concrete, and for his time explaining them to me. These data strongly aided my understanding of the mechanical response of asphalt concrete.

TABLE OF CONTENTS

Page

LIST OF FIGURES

FIGURE Page

FIGURE Page

FIGURE Page

LIST OF TABLES

1 INTRODUCTION

Roadways are designed to last until rehabilitation or replacement, and it is their degraded performance that dictates the design of pavements. It is, therefore, essential to be able to predict the degradation of an asphalt concrete through the development of a robust computational model that can effectively simulate the performance of an asphalt pavement under mechanical (e.g., traffic) and environmental (e.g., moisture, temperature) loading.

Although all materials are heterogeneous, continuum models describe many materials' behavior in a way that allows computation of much more complex physical problems than otherwise feasible. To create a model capable of simulating whole sections of a roadway, this study will use a continuum approach to describe all facets of material behavior. Many past studies have characterized asphalt concrete and its phases using various models (some using continuum models and some using micromechanical approaches), and this section will describe several of these studies and models.

1.1 Literature Review

1.1.1 Mechanical constitutive modeling of asphalt concrete

Experiments show that asphalt concretes deform in a time-dependent manner with recoverable and irrecoverable components and that they sustain losses of stiffness when subjected to extreme loads (for example, see Perl et al. 1983, Sides et al. 1985, Collop et al. 2003, Grenfell et al. 2008). Cheung and Cebon (1997) and Airey et al. (2002a,b, 2004) studied asphalt binder and determined its response was nonlinear, depending on a combination of temperature and load rate and level. The irrecoverable dilation

This thesis follows the style of Mechanics of Time-Dependent Materials.

response of asphalt concrete is overestimated by viscoplasticity with an associated flow rule, so nonassociated viscoplasticity must be used to achieve accurate predictions (Masad et al. 2007a).

Sousa et al. (1993) developed a nonlinear viscoelastic model for asphalt concrete which was improved by Sousa et al. (1994) to include plasticity with a von Mises yield surface and isotropic and kinematic hardening. However, this model did not include a pressure-sensitive yield surface or a time-dependent plastic response (viscoplasticity). Ha and Schapery (1998) developed a nonlinear viscoelastic model with damage for particulate composites, but did not model permanent deformations. Seibi et al. (2001) developed a model which used Perzyna's theory of viscoplasticity with a (pressure-sensitive) Drucker–Prager yield surface for the irrecoverable component of deformation, but did not model the time-dependent character of the recoverable response. Lu and Wright (1998) and Oeser and Moller (2004) developed elastoviscoplastic constitutive models for asphalt concrete, but did not include a nonassociated plastic flow rule. Sadd et al. (2004) used the Schapery nonlinear viscoelasticity model to describe the nonlinear viscoelastic behavior of asphalt concrete with damage in a micromechanical framework, but did not consider irreversible plastic deformations. Kringos, Scarpas, and their collaborators modeled asphalt concrete at a micromechanical level including viscoelasticity and plasticity (for finite strains) and damage, with an emphasis on moisture-induced damage (Kringos 2007, Kringos and Scarpas 2008, Kringos et al. 2008b).

Tashman (2003) developed a model for hot mix asphalt which utilized a nonassociated viscoplastic flow rule to describe the irreversible component of the deformation. This model accounted for damage, work hardening, and material anisotropy. Levenberg and Uzan (2004) developed a cross-anisotropic viscoelastic-viscoplastic constitutive model for asphalt concrete, but this model did not include viscoplasticity

and damage criteria featuring all the dependence on state of stress observed in asphalt conrete, nor did it consider nonlinear viscoelastic response. Dessouky (2005) developed a model that used a modified Drucker–Prager viscoplastic yield surface, which captures the pressure-sensitivity of asphalt concrete, but did not model the nonlinear viscoelastic character for the response.

Park et al. (1996) and Park and Schapery (1997) developed a viscoelastic continuum damage model for asphalt concrete, but neglected permanent deformations which are observed in experiments, and their model was limited to uniaxial loading. Chehab et al. (2003) developed a continuum viscoelastoplastic model for undamaged asphalt concrete, but its scope was also limited to uniaxial characterization. Uzan (2005) developed a damaged viscoelastic, viscoplastic, continuum model using the work of Park and Schapery (1997) and Schapery (1999) for asphalt concrete, but did not model three dimensional response.

Masad, Huang, and their collaborators developed a nonlinear-viscoelastic–viscoplastic model for asphalt concrete (Masad et al. 2007b, Huang et al. 2007, Huang 2008). Schapery's single-integral theory modeled the nonlinear viscoelastic character of the reversible response and Perzyna's theory modeled the viscoplastic response using a modified Drucker–Prager yield surface and a nonassociated flow rule. The Drucker–Prager yield surface was modified to describe the effect of stress state in a more advanced way than the classical Drucker–Prager yield surface, so that extensions lead to more viscoplastic flow, apart from hydrostatic pressure state. However, this model did not include damage to the material.

1.1.2 Moisture damage

Moisture damage of asphalt concrete is the degradation of mechanical properties due to the presence of moisture. Moisture damage contributes significantly to the degradation of asphalt pavements; in the US, this leads to additional vehicle costs

Figure 1.1 Moisture-induced damage in pavements results in raveling (left) and potholing (right) (Kringos 2007)

over $54 billion annually (Copeland 2005). Moisture damage has been studied using a microscale perspective since 1932 and in the field since 1967 (Nicholson 1932, Field and Phang 1967). Much experimental research has sought to determine the degrading effects of moisture, but all purely empirical studies suffer from inability to predict performance, so a description of such work is not included here.

An asphalt mix is a composite material comprised of coarse aggregates, fine aggregates, asphalt binder, and air, and may be understood as a particulate composite of coarse aggregates and a matrix of *asphalt mastic* comprised of the other mix constituents. When an asphalt mix is exposed to moisture through water present at its surface (e.g. from rainfall), internally from wet constituents, or through environmental humidity, the moisture disperses through the mix into its air voids and through its solid portion by diffusion and permeation. Once infiltrated by moisture, the mix may be degraded due to several processes: chemical, physical, and mechanical (Kandhal 1994, Kassem 2006, Bhasin 2006, Kringos 2007, Kringos and Scarpas 2008, Caro et al. 2008a).

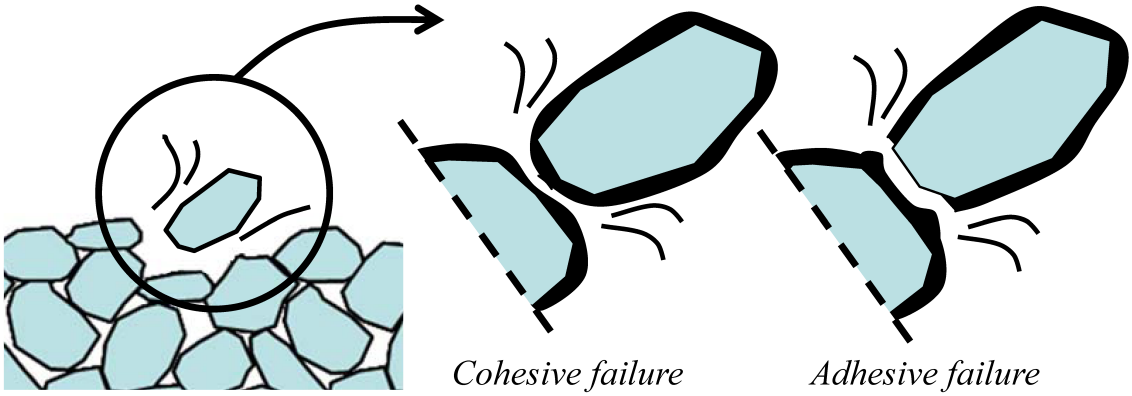

Figure 1.2 Adhesive and cohesive failure (Kringos 2007)

Figure 1.1 shows the severe moisture damage resulting in raveling, where aggregates separate from each other individually and potholing, where entire chunks of pavement are removed. Raveling may occur as adhesive failure, where aggregates separate from the mastic, or cohesive failure, where fracture occurs in the mastic between aggregates (Kandhal 1994, Kringos 2007, Caro et al. 2008a). Figure 1.2 illustrates the difference between adhesive and cohesive failure.

The chemical reactions occurring between moisture and asphalt mix constituents may lead to loss of material that gives the mix its overall cohesion. The overall cohesion is due to a combination of the cohesion of the mastic and maintaining the mastic's adhesion to the aggregates. The cohesion of the aggregates is not included because the matrix cohesion is more essential and because aggregates tend to be very strong and stable compared to the mastic or the aggregate–mastic bond (Little and Jones 2003, Kringos 2007, Caro et al. 2008a).

Physical moisture-induced damage mechanisms are more readily understood and have been studied in some detail (Zollinger 2005, Lytton et al. 2005, Bhasin 2006, Masad et al. 2006c). Physical damage due to moisture occurs when the moisture

bonds to the asphalt mix, breaking mastic cohesive or aggregate–mastic adhesive physical bonds. This may lead to debonding of the mastic from aggregates, dispersion of the mastic, possibly lost to flow, and the formation of microcracks in the mix (Kringos 2007, Kringos et al. 2008b, Kringos and Scarpas 2008, Caro et al. 2008a).

Moisture-induced mechanical degradation of occurs when the presence of nearly-incompressible water in air voids leads to fast-flowing water through the mix upon mechanical loading, which can cause unfavorable stress distributions and erosion of the mastic (Kandhal 1994, Kringos 2007, Kringos et al. 2008b, Kringos and Scarpas 2008).

Recent work studied the fundamental mechanisms of moisture damage, including the role of air voids (Masad et al. 2006b, Kassem 2008), the effects of the physical characteristics of the material and aggregate–binder adhesive bond (Little and Jones 2003, Masad et al. 2006c, Bhasin et al. 2006), and moisture transport in asphalt concrete (Chen et al. 2006, Kassem 2006, Masad et al. 2006a). Caro et al. (2008a,b) modeled asphalt concrete microstructurally, with degradation in the mastic and at the aggregate–mastic interface using cohesive elements to consider the effect of moisture at the interface and a simple law for damage in the mastic matrix which does not account for irreversibly of moisture-induced damage.

Kringos, Scarpas, and their collaborators studied asphalt concrete at the microscale, predicting the infiltration of moisture and the degradation of the material (Kringos and Scarpas 2005, Kringos et al. 2007, Kringos 2007, Kringos and Scarpas 2008, Kringos et al. 2008a,b). Asphalt mastic was modeled using a finite deformation, viscoelastoplastic model. They studied damage at the aggregate–mastic bond and in the body of the mastic due to direct moisture effects and mechanical–moisture coupling effects (pumping). This model neglected irreversibility of moisture damage effects (i.e., moisture-induced damage was recovered upon drying), which is not

realistic.

Moisture-induced damage in other materials has also been studied, though generally this research has been microscale rather than continuum modeling. Roy and Xu (2001) and Roy and Benjamin (2004) studied moisture diffusion and damage for polymer matrix composites and graphite/epoxy laminate composites with macroscale application, but this research studied the change in diffusivity of materials due to damage, not the damaging effects of moisture. Chiarelli et al. (2003) developed an elastoplastic damage material model for claystone with properties varying on moisture content, but did not model damage due to moisture independent of mechanical loading.

Tang et al. (2005) studied diffusion and moisture-induced damage in woven polymer composites using microscale finite element simulations, but this study focused on the moisture transport due to the special geometry of woven composites, not constitutive modeling of moisture-damaged materials. Roels et al. (2006) proposed a fully coupled mechanical–moisture–damage model and numerical implementation for porous materials, but this model did not include viscoelastic or viscoplastic effects in its mechanical response, and cracks were modeled discretely.

1.2 Research Approach

The constitutive model uses continuum damage mechanics (CDM) (Kachanov 1958, 1985), which is a framework for modeling the nucleation, growth, and propagation of numerous micro-cracks and their evolution into macro-cracks that ultimately leads to failure. CDM is a robust technique which has been used to model degradation in a wide range of materials. CDM can be effectively used in predicting the onset (site and time or where and when) of damage nucleation (cracking potential) and its evolution (crack propagation).

In CDM, the effects of the material degradation are explained by explicitly modify-

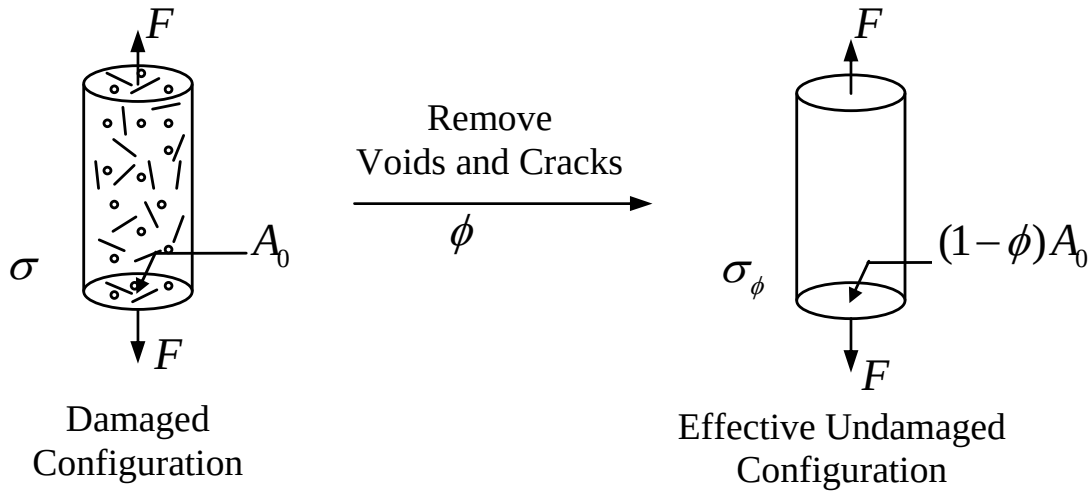

Figure 1.3 Damaged and effective undamaged configurations (Abu Al-Rub 2004)

ing the stiffness of the material sustaining damage. Two configurations are specified: the actual configuration and an equivalent, undamaged configuration which obeys an undamaged material law. The two configurations may be related in various ways, usually based on the assumption that either the strain or the elastic strain energy of the two configurations are equal. The difference between the damaged and undamaged configurations is calculated based on a new parameter, usually called the *damage density* (and this thesis will use the more general term *damage variable*), which can be calculated due to laws ranging from very simple to laws which incorporate a high degree of realistic physical information for a given material. See Voyiadjis and Kattan (1999), Abu Al-Rub and Voyiadjis (2003) and Lemaitre (2005) for a more complete treatment of continuum damage mechanics.

The simplest example for understanding continuum damage mechanics is the axial bar. Consider a bar with area A_0 and length L subjected to a force F. The stress in the bar is $\sigma = F/A_0$. Now suppose that another bar is identical except that it contains

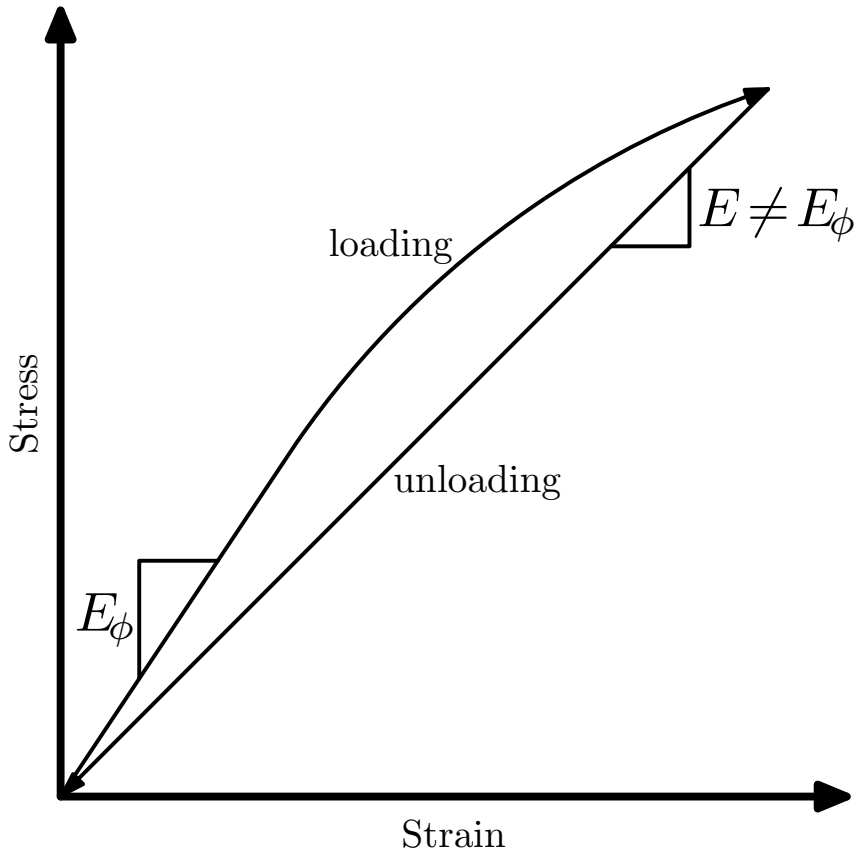

Figure 1.4 Damaged material response

randomly-distributed microcracks and microvoids, so that a proportion ϕ (the damage variable) of the cross-sectional area of the bar is removed, so that the area of that bar is $(1-\phi)A_0$. (See Figure 1.3.) The stress in this bar is $\sigma_\phi = F/[(1-\phi)A_0] = \sigma/(1-\phi)$. Both bars an apparent (*nominal*) area A_0, but because of their different areas that are effective in resisting loads, the bar with the microcracks and microvoids will be weaker (lower stiffness and strength).

Since the bars are made out of the same material, they have the same material (*effective*) stiffness E_ϕ, but since they have different areas, they respond differently to loads, so a damaged bar with area $(1-\phi)A_0$ has an apparent (*nominal*) stiffness E. Figure 1.4 shows an example stressstrain diagram for a bar that sustains damage

damage upon increased load. Initially the material is undamaged, so the nominal and effective stiffness are equal $E = E_\phi$, but upon increased loading the material sustains damage and its stiffness decreases $E < E_\phi$. Upon unloading, the material remains damaged and unloads at the (damaged) nominal stiffness E.

How is the difference in the mechanical response quantified? The most classical assumption (Kachanov 1958, 1985, Lemaitre 2005) to understand the stiffness change is to hypothesize the strains for the two bars must be equal, so for the strain in the first bar ϵ and the strain in the bar with the reduced area ϵ_ϕ,

$$\epsilon = \epsilon_\phi \implies \frac{\sigma_0}{E} = \frac{\sigma_\phi}{E_\phi} \implies \frac{F/A_0}{E} = \frac{F/[(1-\phi)A_0]}{E_\phi} \implies E = (1-\phi)E_\phi. \quad (1.1)$$

The relationships $\epsilon = \epsilon_\phi$, $\sigma = (1-\phi)\,\sigma_\phi$, and $E = (1-\phi)\,E_\phi$ define the modified constitutive law. This is a common description for the effect of damage, but it will not be used in this research.

Suppose instead that the strain energy densities the two bars are equal. Then

$$\sigma\epsilon = \sigma_\phi\epsilon_\phi \implies \frac{\sigma^2}{E} = \frac{\sigma_\phi^2}{E_\phi} \implies \frac{\sigma^2}{E} = \frac{\sigma^2}{(1-\phi)^2 E_\phi} \implies E = (1-\phi)^2\,E_\phi, \quad (1.2)$$

and we also recognise

$$\sigma_\phi = E_\phi\epsilon_\phi \implies \frac{\sigma}{1-\phi} = \frac{E}{(1-\phi)^2}\epsilon_\phi \implies \epsilon_\phi = (1-\phi)\,\epsilon_0. \quad (1.3)$$

The relationships $(1-\phi)\,\epsilon = \epsilon_\phi$, $\sigma = (1-\phi)\,\sigma_\phi$, and $E = (1-\phi)^2\,E_\phi$ define the modified constitutive if the strain energy densities for the two cases are equal. For convenience, we wish to perform computations in terms of the nominal strain ϵ. To

do this, we define the effective stress, strain, and stiffness

$$\begin{aligned} \bar{\sigma} &= \frac{\sigma_\phi}{1-\phi} = \frac{\sigma}{(1-\phi)^2} \\ \bar{\epsilon} &= \epsilon \\ \bar{E} &= \frac{E}{(1-\phi)^2} \end{aligned} \tag{1.4}$$

so that

$$\bar{\sigma} = \bar{E}\bar{\epsilon} = \bar{E}\epsilon. \tag{1.5}$$

This definition is consistent hypothesis that the strain energy densities are equal (as presented in Equations (1.2) and (1.3)), but is expressed in terms of the nominal (observable) strain.

CDM can be extended to multiple dimensions. The simplest extension is isotropic damage, in which case (1.4) becomes

$$\begin{aligned} \bar{\sigma}_{ij} &= \frac{1}{(1-\phi)^2}\sigma_{ij} \\ \bar{\epsilon}_{ij} &= \epsilon_{ij} \\ \bar{E}_{ijkl} &= \frac{1}{(1-\phi)^2}E_{ijkl} \end{aligned} \quad . \tag{1.6}$$

(Throughout this thesis, tensors are represented using indicial notation. Repeated indices imply summation.)

In general, damage need not be isotropic, but can be arbitrarily anisotropic, in which case in may be represented as a second- or fourth-order tensor. This concept is explained by Voyiadjis and Kattan (1999), Abu Al-Rub and Voyiadjis (2003) and Lemaitre (2005). Material isotropy in all facets (viscoelasticity, viscoplasticity, and damage) is assumed in this study for the sake of simplicity. If experiments show that

anisotropic damage is necessary to describe the response of asphalt concrete, the proposed model can be adapted.

To determine the damage variable ϕ, material-specific laws govern the evolution based on loading. Section 3 presents the model for predicting the damage due to mechanical loading and Section 4 presents the model for predicting the damage due to the presence of moisture.

1.3 Research Tasks

The research objectives will be accomplished by the following tasks:

- The viscoelastic–viscoplastic response will be modeled using Schapery's single-integral nonlinear viscoelastic model and Perzyna's viscoplasticity model with a non-associated flow rule, using the same approach as Huang (2008).

- An analytical model for mechanically-induced damage will be developed, predicting the onset and growth of damage using laws that reflect the physically expected dependence on loading. In particular, damage will be pressure-sensitive, state-of-stress–sensitive, and grow with a physically reasonable law which can be tuned to experimental results.

- An analytical model for damage due to moisture loading will be developed. The model will meet physical expectations in that the mechanisms of adhesive damage (degradation of the bond between the aggregates and the mastic) and cohesive damage (degradation within the asphalt mastic) will be treated separately, with their initiation and growth described separately, with the option to have the two phenomena behave differently in the model.

- The undamaged material model will be discretized and implemented for finite element simulations in the commercial finite element package Abaqus. Guidelines

for this implementation are provided by Huang (2008).

- The mechanical and moisture damage laws will likewise be discretized and the undamaged material model implementation will be modified to include damage effects.

- The model and will be tested by running simulations using the numerical implementation in Abaqus corresponding to realistic loading conditions for mechanical tests.

This thesis is organized into five sections. This section has introduced and motivated the challenge of modeling the response of asphalt concrete. Section 2 presents the undamaged constitutive model (Huang et al. 2007, Huang 2008) featuring nonlinear viscoelasticity and viscoplasticity. Section 3 proposes the model for mechanically-induced damage and Section 4 proposes the model for moisture-induced damage. Section 5 reviews the proposed model and suggests future work for modeling asphalt concrete. Appendix A presents micromechanical simulations which use the proposed material model to describe asphalt mastic.

2 VISCOELASTIC–VISCOPLASTIC CONSTITUTIVE MODEL

The proposed damaged constitutive model is based on a model that has been developed for asphalt concrete mixes which describes its nonlinear viscoelastic and viscoplastic response. The viscoelastic model is derived by Masad et al. (2007b) and Huang et al. (2007) and the viscoelastic–viscoplastic model is presented by Huang (2008), but the model is described in this section for completeness.

Asphalt concretes are modeled as viscoelastic materials because the recoverable response of asphalt changes with time under constant load and varies for various load rates (Sides et al. 1985, Grenfell et al. 2008) and specifically as nonlinear viscoelastic materials because experiments have shown asphalt binder's response varies with load level and temperature nonlinearly (Cheung and Cebon 1997, Airey et al. 2002a,b, 2004). It is readily observed that asphalt pavements in service frequently sustain load and recover deformations, so any accurate model for asphalt concrete must include viscoelasticity.

Asphalt concretes are modeled as viscoplastic materials because experiments and observation reveal that asphalt concretes undergo permanent deformation under high loads, and that the rate at which these permanent deformations accumulate varies with loading rate (Sides et al. 1985, Sousa et al. 1993, Dessouky 2005, Grenfell et al. 2008). Specifically, a modified Drucker–Prager yield surface and non-associated flow rule are used to conform to empirical observations of asphalt mix response (Dessouky 2005, Masad et al. 2007a). Because excessive permanent deformations may lead to unacceptable pavement performance, any accurate model for asphalt concrete must include viscoplasticity.

The Schapery single-integral nonlinear viscoelastic model (1969) is used for visco-

elasticity, and Perzyna's model (1963, 1966, 1971) is used for viscoplasticity. Asphalt concrete is assumed to be isotropic with constant Poisson's ratio for the development of this material model. The nonlinear viscoelastic–viscoplastic material model is adapted for numerical use using a recursive-iterative numerical algorithm (as proposed by Haj-Ali and Muliana (2004))and is implemented in the popular finite element code Abaqus using a user material subroutine UMAT. Results from finite element simulations in Abaqus are presented.

All values in this section are *effective* values because this section presents the model for the *undamaged material*. The superimposed bars ($\bar{\bullet}$) will be suppressed throughout this section for simplicity of notation, but are appropriate for all variables.

2.1 Nonlinear Viscoelasticity

Consider the single-integral, nonlinear viscoelastic response (Schapery 1969), which predicts the strain

$$\epsilon^{ve}(t) = g_0\, D_0\, \sigma(t) + \int_0^t g_1\, \Delta D(\psi(t) - \psi(\tau)) \frac{g_2\, \sigma(\tau)}{d\tau} d\tau, \tag{2.1}$$

where $\sigma(t)$ is the stress at time t, D_0 is the instantaneous compliance, ΔD is the transient compliance, $\psi(t)$ is the reduced time, and g_0, g_1, and g_2 are nonlinear parameters explained on the following page. Time $t = 0$ is some time before loading. A nonlinear viscoelastic model was chosen due to the observations of Cheung and Cebon (1997) and Airey et al. (2002a,b, 2004). *Throughout this thesis positive values of stress and strain represent* compression*, as is the typical convention for pressure-sensitive materials.*

The reduced time

$$\psi(t) = \int_0^t \frac{d\xi}{a_T(\xi)\, a_s(\xi)}$$

adjusts the time the transient compliance is evaluated using the temperature shift factor a_T and the stress or strain shift factor a_s, and other shift factors may be postulated if necessary. The reduced time adjusts the predictions of Equation (2.1) due to the effects of temperature and stress or strain (or any other inputs which are experimentally observed to modify response in a time-shifting manner) by conforming to the response predicted for a different loading rate.

The nonlinear parameter g_0 relates to the instantaneous compliance, the nonlinear parameter g_1 relates to the transient compliance, and the nonlinear parameter g_2 relates to the effect of the loading rate on response. The nonlinear parameters g_0, g_1, and g_2 may be functions of stress, strain, loading rate, temperature, moisture, etc., and may be empirically determined based on observed nonlinearity. g_0, g_1, and g_2 are positive and for small values of stress should be close to unity; if $g_0 = g_1 = g_2 = 1$, Equation (2.1) reduces to the Boltzmann integral in linear viscoelasticity (Haj-Ali and Muliana 2004).

To use this formulation to solve three-dimensional problems, we recall from linear elasticity that the strain ϵ_{ij}^{ve} for an isotropic material may be decomposed into deviatoric strain e_{ij}^{ve} and volumetric strain ϵ_{kk}^{ve}

$$\epsilon_{ij}^{ve} = \underbrace{\frac{1}{2} J S_{ij}}_{e_{ij}^{ve}} + \underbrace{\frac{1}{3} B \sigma_{kk}}_{\epsilon_{kk}^{ve}} \delta_{ij}, \tag{2.2}$$

where J is the shear compliance, B is the bulk compliance, S_{ij} is the deviatoric stress

$$S_{ij} = \sigma_{ij} - \frac{\sigma_{kk}}{3} \delta_{ij},$$

σ_{kk} is the volumetric stress, and δ_{ij} is the Kronecker delta

$$\delta_{ij} = \begin{cases} 1 & \text{if } i = j \\ 0 & \text{if } i \neq j \end{cases}.$$

Using the Schapery single-integral model (2.1), the viscoelastic deviatoric and volumetric strain are expressed as

$$\begin{aligned} e_{ij}^{ve}(t) &= \frac{1}{2}\, g_0(t)\, J_0\, S_{ij}(t) + \frac{1}{2}\, g_1(t) \int_0^t \Delta J\left(\psi(t) - \psi(\tau)\right) \frac{d\left(g_2(\tau)\, S_{ij}(\tau)\right)}{d\tau} d\tau \\ \epsilon_{kk}^{ve}(t) &= \frac{1}{3}\, g_0(t)\, B_0\, \sigma_{kk}(t) + \frac{1}{3}\, g_1(t) \int_0^t \Delta B\left(\psi(t) - \psi(\tau)\right) \frac{d\left(g_2(\tau)\, \sigma_{kk}(\tau)\right)}{d\tau} d\tau \end{aligned}, \tag{2.3}$$

where the meanings of the new terms should be obvious: J_0 is the instantaneous shear compliance, $\Delta J(t)$ is the transient shear compliance, B_0 is the instantaneous bulk compliance, and $\Delta B(t)$ is the transient bulk compliance.

Experimental measurements have shown that the Poisson's ratio ν for asphalt concrete varies some with time, temperature, or loading rate, but the simplification that ν is time-independent is adopted for this material model because the effect of this small variation is minor compared to other effects (ASTM 1995, Di Benedetto et al. 2007). This leads to the modulus interrelations

$$\begin{array}{ll} J_0 = 2(1-\nu)D_0 & B_0 = 3(1-2\nu)D_0 \\ \Delta J(t) = 2(1-\nu)\Delta D(t) & \Delta B(t) = 3(1-2\nu)\Delta D(t) \end{array}. \tag{2.4}$$

Note only one independent function of time is part of the analysis.

The transient compliance $\Delta D(t)$ is represented by the Prony series

$$\Delta D(t) = \sum_{n=1}^{N_p} D_n \left(1 - e^{-\lambda_n t}\right), \tag{2.5}$$

where for the N_p modes, D_n is the coefficient of the Prony series in mode n and λ_n is

the retardation time in mode n.

Substituting the transient compliance from (2.5) into (2.3) yields

$$\begin{aligned} e_{ij}^{ve}(t) &= \frac{g_0(t)J_0S_{ij}(t)}{2} + \frac{g_1(t)}{2}\int_0^t \sum_{n=1}^{N_p} J_n\left(1 - e^{-\lambda_n\left(\psi(t)-\psi(\tau)\right)}\right)\frac{d\big(g_2(\tau)S_{ij}(\tau)\big)}{d\tau}d\tau \\ \epsilon_{kk}^{ve}(t) &= \frac{g_0(t)B_0\sigma_{kk}(t)}{3} + \frac{g_1(t)}{3}\int_0^t \sum_{n=1}^{N_p} B_n\left(1 - e^{-\lambda_n\left(\psi(t)-\psi(\tau)\right)}\right)\frac{d\big(g_2(\tau)\sigma_{kk}(\tau)\big)}{d\tau}d\tau \end{aligned} \tag{2.6}$$

which serve as the governing equations for the viscoelastic strain.

2.2 Viscoplasticity

In addition to the recoverable viscoelastic strain, experiments indicate some strain in asphalt concrete is irrecoverable with time-dependent response, so we divide the strain ϵ_{ij} into recoverable viscoelastic strain ϵ_{ij}^{ve} and irrecoverable viscoplastic strain ϵ_{ij}^{vp} (assuming small strains)

$$\epsilon_{ij} = \epsilon_{ij}^{ve} + \epsilon_{ij}^{vp}. \tag{2.7}$$

Taking the time derivative of this expression, the strain rate is

$$\dot{\epsilon}_{ij} = \dot{\epsilon}_{ij}^{ve} + \dot{\epsilon}_{ij}^{vp}, \tag{2.8}$$

for the viscoelastic strain rate $\dot{\epsilon}_{ij}^{ve}$ and the viscoplastic strain rate $\dot{\epsilon}_{ij}^{vp}$.

This study uses Perzyna's model (1963, 1966, 1971) to calculate the viscoplastic strain rate

$$\dot{\epsilon}_{ij}^{vp} = \begin{cases} \Gamma\left(\dfrac{f}{\sigma_y^0}\right)^N \dfrac{\partial g}{\partial \sigma_{ij}}, & \text{if } f \geq 0 \\ 0, & \text{if } f < 0 \end{cases}, \tag{2.9}$$

where f is the yield surface, g is the viscoplastic potential energy function, Γ is a viscosity parameter, σ_y^0 is a parameter which normalizes stress values, and N is a parameter describing rate-dependence. The rate of viscoplastic strain is controlled by

the scalar $\Gamma \left\langle \frac{f}{\sigma_y^0} \right\rangle^N$ when the overstress function $\left\langle \frac{f}{\sigma_y^0} \right\rangle^N$ is positive, and the direction is controlled by the tensor $\frac{\partial g}{\partial \sigma_{ij}}$. If the yield surface function does not coincide with the potential energy function ($f \neq g$), Equation (2.9) is a non-associated viscoplastic flow rule.

2.2.1 Yield surface

The yield surface determines whether a stress state results in viscoplastic strain. This study uses a modified Drucker–Prager yield surface

$$f = \tau - \alpha I_1 - \kappa(\epsilon_e^{vp}), \tag{2.10}$$

where τ and I_1 are stress invariants, α is a pressure-sensitivity parameter related to the angle of friction in the mix, and κ is the viscoplastic hardening function, which depends on the *equivalent viscoplastic strain*[1] ϵ_e^{vp}.

Consider $\tau - \alpha I_1$. I_1 is the first stress invariant

$$I_1 = \frac{1}{3}\sigma_{ii}, \tag{2.11}$$

which is the hydrostatic pressure. τ is the deviatoric shear stress modified for the stress state

$$\tau = \frac{\sqrt{J_2}}{2}\left(1 + \frac{1}{d} + \left(1 - \frac{1}{d}\right)\frac{J_3}{\sqrt{J_2^3}}\right), \tag{2.12}$$

where J_2 and J_3 are the second and third deviatoric stress invariants

$$\begin{aligned} J_2 &= \frac{3}{2}S_{ij}S_{ij}, \\ J_3 &= \frac{9}{2}S_{ij}S_{jk}S_{ki} \end{aligned}, \tag{2.13}$$

[1]The equivalent plastic strain is sometimes called the "effective plastic strain", as in previous works to model asphalt concrete, but this language is not used to avoid confusion with the use of the term *effective* in continuum damage mechanics.

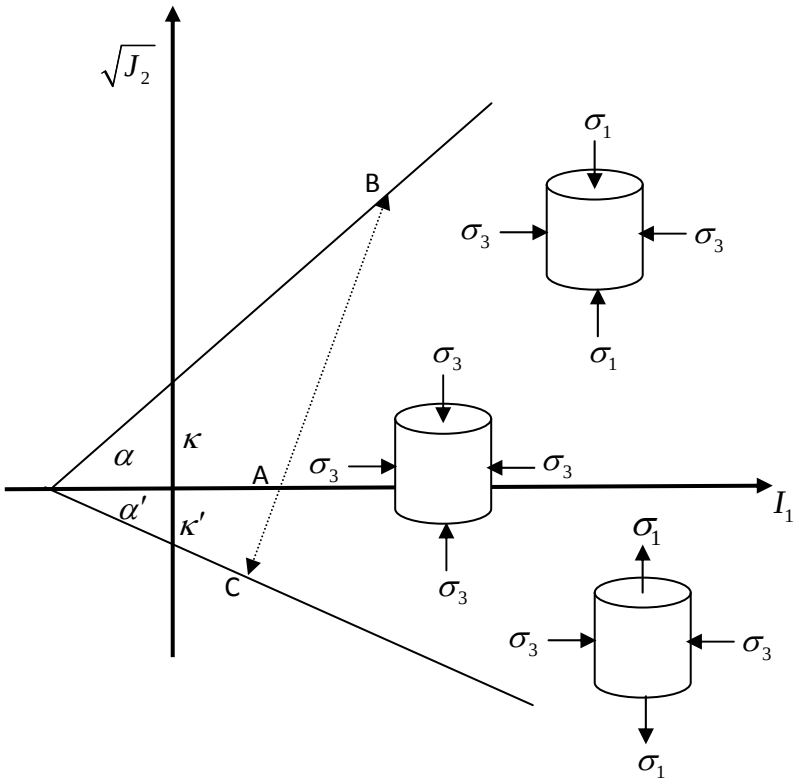

Figure 2.1 Influence of stress path on the modified Drucker–Prager yield surface (Huang 2008)

and d is a material parameter describing sensitivity to extension, regardless of hydrostatic state.

Figure 2.1 shows the influence of stress path on the response using the modified Drucker–Prager yield surface, plotted in the I_1–$\sqrt{J_2}$ plane. For a classical Drucker–Prager yield surface, $\alpha = \alpha'$ and $\kappa = \kappa'$, but the parameter d causes them to differ, resulting in a modified Drucker–Prager yield surface.

To better understand the yield surface, consider a body loaded in plane stress

with principal stresses σ_1 and σ_2 (all other stress components are zero). Then

$$\begin{aligned} I_1 &= \frac{1}{3}(\sigma_1 + \sigma_2) \\ J_2 &= \sigma_1^2 - \sigma_1\sigma_2 + \sigma_2^2 \\ J_3 &= \frac{1}{2}(2\sigma_1 - \sigma_2)(\sigma_1 + \sigma_2)(\sigma_1 - 2\sigma_2), \end{aligned} \tag{2.14}$$

so the yield surface in Equation (2.10) becomes

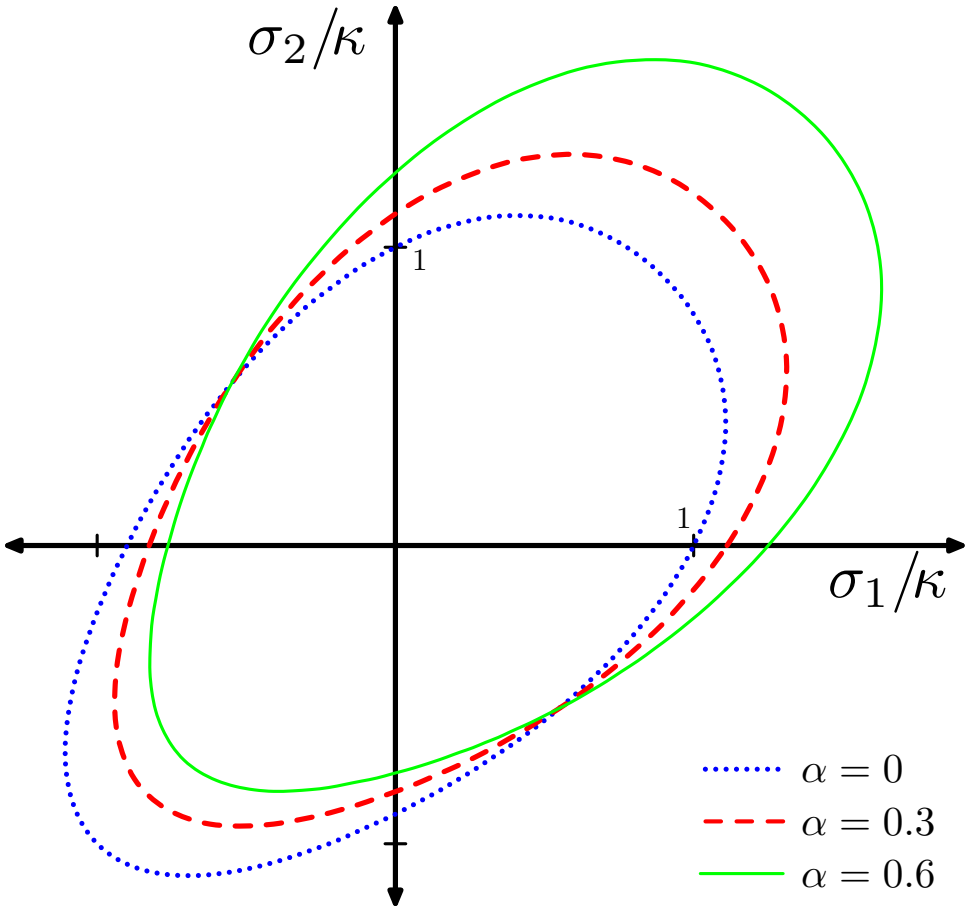

Figure 2.2 Yield surface for plane stress for $d = 0.9$ and various values of α

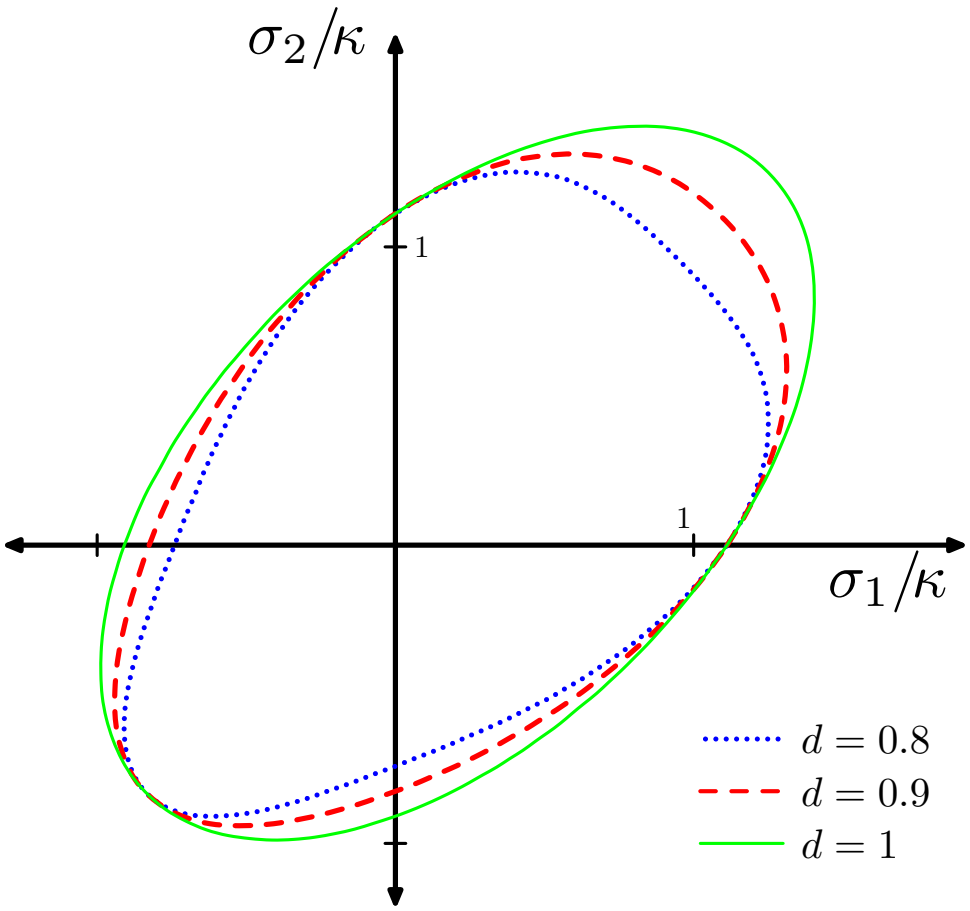

Figure 2.3 Yield surface for plane stress for $\alpha = 0.3$ and various values of d

$$\frac{\sigma_1^2 - \sigma_1\sigma_2 + \sigma_2^2}{2}\left(1 + \frac{1}{d} + \left(1 - \frac{1}{d}\right)\frac{(2\sigma_1 - \sigma_2)(\sigma_1 + \sigma_2)(\sigma_1 - 2\sigma_2)}{2\left(\sigma_1^2 - \sigma_1\sigma_2 + \sigma_2^2\right)^{3/2}}\right) - \frac{\alpha}{3}(\sigma_1 + \sigma_2) - \kappa\left(\epsilon_e^{vp}\right) = 0. \quad (2.15)$$

We may now plot the yield surface in the σ_1–σ_2 plane.

Figures 2.2 and 2.3 show the yield surface for plane stress with principal stresses σ_1 and σ_2 normalized by the isotropic hardening function $\kappa(\epsilon_e^{vp})$.

2.2.2 Viscoplastic potential energy function

In asphalt concrete, the direction of the viscoplastic strain growth is not normal to the yield surface, which is called non-associated flow, and an associated flow rule would overestimate the dilation compared to experimental measurements (Masad et al. 2007a). This study defines the viscoplastic potential energy function

$$g = \tau - \beta I_1, \tag{2.16}$$

which is similar to the yield surface, except the material parameter β governs the pressure sensitivity of the surface.

The derivative in (2.9) is calculated to be

$$\frac{\partial g}{\partial \sigma_{ij}} = \frac{1}{2}\Bigg[\left(1+\frac{1}{d}\right)\frac{3S_{ij}}{2\sqrt{J_2}} + \left(1-\frac{1}{d}\right)\frac{3\left(\frac{9}{2}S_{ik}S_{kj}-J_2\delta_{ij}\right)J_2 - 3S_{ij}J_3}{J_2^2} - \frac{2\beta}{3}\delta_{ij}\Bigg]. \tag{2.17}$$

2.2.3 Hardening function

The evolution of the yield surface (Equation (2.10)) depends on the isotropic hardening function κ, for which the isotropic hardening rule

$$\kappa(\epsilon_e^{vp}) = \kappa_0 + \kappa_1\Big(1 - \exp\left(-k_2\epsilon_e^{vp}\right)\Big) \tag{2.18}$$

is used (Lemaitre and Chaboche 1990), where κ_0 defines the initial yield stress, κ_1 describes the saturated stress for the fully-hardened material, κ_2 describes the transition rate between κ_0 and $\kappa_0 + \kappa_1$, and

$$\epsilon_e^{vp} = \int_0^t \dot{\epsilon}_e^{vp} dt$$

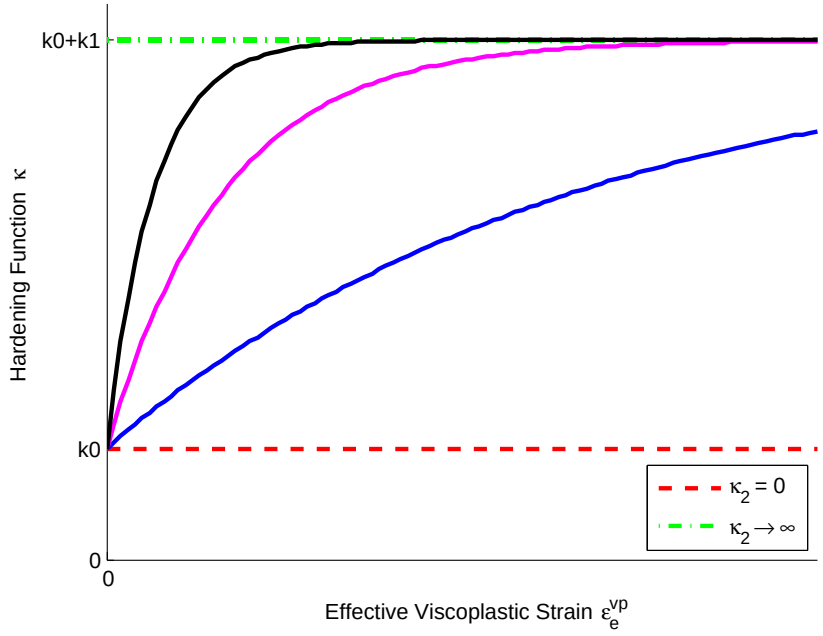

Figure 2.4 The hardening function $\kappa(\epsilon_e^{vp})$

is the equivalent viscoplastic strain, where time $t = 0$ is some time before viscoplastic deformation. Figure 2.4 shows the transition of κ from κ_0 to κ_1, which is accelerated for larger values of κ_2.

We define the equivalent viscoplastic strain ϵ_e^{vp} in terms of the equivalent stress σ_e, which in turn is defined by

$$F(\sigma_{ij}) = \tau - \alpha I_1 = C\sigma_e^n, \tag{2.19}$$

where C and n are constants. Considering the case of uniaxial compression in the 1 direction,

$$I_1 = \frac{1}{3}\sigma_{11},\ \tau = \sigma_{11} \implies \left(1 - \frac{\alpha}{3}\right)\sigma_{11} = C\sigma_e^n \implies C = 1 - \frac{\alpha}{3},\ n = 1. \tag{2.20}$$

Uniaxial compression is the mode chosen to define the equivalent plastic strain because it is the most common laboratory test; uniaxial tension or any other mode could have been chosen for this definition. Substituting this result into (2.19) yields

$$\tau - \alpha I_1 = \left(1 - \frac{\alpha}{3}\right)\sigma_e^1 \implies \sigma_e = \frac{3\left(\tau - \alpha I_1\right)}{3 - \alpha}. \tag{2.21}$$

From this equivalent viscoplastic stress we find the equivalent viscoplastic strain by appealing to the viscoplastic work rate

$$\dot{W}_{vp} = \sigma_{ij}\dot{\epsilon}_{ij}^{vp} = \sigma_{ij}\frac{\sqrt{\dot{\epsilon}_{kl}^{vp}\dot{\epsilon}_{kl}^{vp}}}{\sqrt{\frac{\partial g}{\partial \sigma_{mn}}\frac{\partial g}{\partial \sigma_{mn}}}}\frac{\partial g}{\partial \sigma_{ij}} = \sigma_e\dot{\epsilon}_e^{vp}. \tag{2.22}$$

Again considering the case of uniaxial compression,

$$\begin{aligned} \sqrt{\frac{\partial g}{\partial \sigma_{ij}}\frac{\partial g}{\partial \sigma_{ij}}} &= \left(1 - \frac{\beta}{3}\right)^2 + 2\left(\frac{1}{2} + \frac{\beta}{3}\right)^2 \\ \sigma_{ij}\frac{\partial g}{\partial \sigma_{ij}} &= \sigma_{11}\left(1 - \frac{\beta}{3}\right) \end{aligned}, \tag{2.23}$$

so (2.22) becomes

$$\dot{W}_{vp} = \frac{\sigma_{11}\left(1 - \frac{\beta}{3}\right)}{\sqrt{\left(1 - \frac{\beta}{3}\right)^2 + 2\left(\frac{1}{2} + \frac{\beta}{3}\right)^2}}\sqrt{\dot{\epsilon}_{ij}^{vp}\dot{\epsilon}_{ij}^{vp}} = \sigma_e\dot{\epsilon}_e^{vp} = \sigma_{11}\dot{\epsilon}_e^{vp}. \tag{2.24}$$

Canceling σ_{11} and rearranging yields the equivalent viscoplastic strain rate

$$\dot{\epsilon}_e^{vp} = \sqrt{\frac{\left(1 - \frac{\beta}{3}\right)^2\dot{\epsilon}_{ij}^{vp}\dot{\epsilon}_{ij}^{vp}}{\left(1 - \frac{\beta}{3}\right)^2 + 2\left(\frac{1}{2} + \frac{\beta}{3}\right)^2}}. \tag{2.25}$$

2.3 Numerical Implementation of the Viscoelastic–Viscoplastic Model

To numerically calculate viscoelastic–viscoplastic response, the model is discretized so it can be used in displacement-based finite element simulations. Consider the state of stress and strain at time t. Assuming small strains, we can express

$$\begin{aligned} \epsilon_{ij}^{t} &= \epsilon_{ij}^{ve,t} + \epsilon_{ij}^{ve,t} = \epsilon_{ij}^{t-\Delta t} + \Delta\epsilon_{ij}^{t} = \epsilon_{ij}^{ve,t-\Delta t} + \epsilon_{ij}^{ve,t-\Delta t} + \Delta\epsilon_{ij}^{ve,t} + \Delta\epsilon_{ij}^{vp,t} \\ \epsilon_{e}^{vp,t} &= \epsilon_{e}^{vp,t-\Delta t} + \Delta\epsilon_{e}^{vp,t} \\ \sigma_{ij}^{t} &= \sigma_{ij}^{t-\Delta t} + \Delta\sigma_{ij}^{t} \end{aligned} \quad , \tag{2.26}$$

where for some quantity x, Δx^t is the difference $x^t - x^{t-\Delta t}$. Time superscripts ($\bullet^t$) indicate a function is evaluated at time t.

2.3.1 Discrete viscoelastic strain

We calculate the incremental viscoelastic shear and volumetric strains

$$\begin{aligned} \Delta e_{ij}^{t} &= e_{ij}^{t} - e_{ij}^{t-\Delta t} \\ \Delta\epsilon_{kk}^{t} &= \epsilon_{kk}^{t} - \epsilon_{kk}^{t-\Delta t} \end{aligned} , \tag{2.27}$$

substituting in (2.6) for the strain to find the strains

$$\begin{aligned} e_{ij}^{ve,t} &= \frac{1}{2}\left[g_0^t + g_1^t g_2^t \sum_{n=1}^{N_p} J_n \left(1 - \frac{1-\exp(-\lambda_n \Delta\psi^t)}{\lambda_n \Delta\psi^t}\right)\right] S_{ij}^t \\ &\quad - \frac{1}{2} g_1^t \sum_{n=1}^{N} J_n \left[\exp(-\lambda_n \Delta\psi^t) q_{ij,n}^{t-\Delta t} - g_2^{t-\Delta t} \frac{1-\exp(-\lambda_n \Delta\psi^t)}{\lambda_n \Delta\psi^t} S_{ij}^{t-\Delta t}\right] \\ \epsilon_{kk}^{ve,t} &= \frac{1}{3}\left[g_0^t + g_1^t g_2^t \sum_{n=1}^{N_p} B_n \left(1 - \frac{1-\exp(-\lambda_n \Delta\psi^t)}{\lambda_n \Delta\psi^t}\right)\right] \sigma_{kk}^t \\ &\quad - \frac{1}{3} g_1^t \sum_{n=1}^{N} B_n \left[\exp(-\lambda_n \Delta\psi^t) q_{kk,n}^{t-\Delta t} - g_2^{t-\Delta t} \frac{1-\exp(-\lambda_n \Delta\psi^t)}{\lambda_n \Delta\psi^t} \sigma_{kk}^{t-\Delta t}\right] \end{aligned} , \tag{2.28}$$

where

$$q_{ij,n}^{t} = \exp\left(-\lambda_n \Delta\psi^t\right) q_{ij,n}^{t-\Delta t} + \left(g_2^t S_{ij}^t - g_2^{t-\Delta t} S_{ij}^{t-\Delta t}\right) \frac{1-\exp\left(-\lambda_n \Delta\psi^t\right)}{\lambda_n \Delta\psi^t}$$
$$q_{kk,n}^{t} = \exp\left(-\lambda_n \Delta\psi^t\right) q_{kk,n}^{t-\Delta t} + \left(g_2^t \sigma_{kk}^t - g_2^{t-\Delta t} \sigma_{kk}^{t-\Delta t}\right) \frac{1-\exp\left(-\lambda_n \Delta\psi^t\right)}{\lambda_n \Delta\psi^t}$$

are the discretized hereditary integrals. The incremental strains, then, are

$$\begin{aligned}
\Delta e_{ij}^t &= \widehat{J}^t S_{ij}^t - \widehat{J}^{t-\Delta t} S_{ij}^{t-\Delta t} - \frac{1}{2}\sum_{n=1}^{N} J_n \left[g_1^t\left(e^{-\lambda_n \Delta\psi^t}\right) - g_1^{t-\Delta t}\right] q_{ij,n}^{t-\Delta t} \\
&\quad - \frac{1}{2} g_2^{t-\Delta t} \sum_{n=1}^{N} J_n \left(g_1^{t-\Delta t}\left[\frac{1-e^{-\lambda_n \Delta\psi^{t-\Delta t}}}{\lambda_n \Delta\psi^{t-\Delta t}}\right] - g_1^t\left[\frac{1-e^{-\lambda_n \Delta\psi^t}}{\lambda_n \Delta\psi^t}\right]\right) S_{ij}^{t-\Delta t} \\
\Delta\epsilon_{kk}^t &= \widehat{B}^t \sigma_{kk}^t - \widehat{B}^{t-\Delta t} \sigma_{kk}^{t-\Delta t} - \frac{1}{2}\sum_{n=1}^{N} B_n \left[g_1^t \exp(-\lambda_n \Delta\psi^t) - g_1^{t-\Delta t}\right] q_{kk,n}^{t-\Delta t} \\
&\quad - \frac{1}{3} g_2^{t-\Delta t} \sum_{n=1}^{N} B_n \left(g_1^{t-\Delta t}\left[\frac{1-e^{-\lambda_n \Delta\psi^{t-\Delta t}}}{\lambda_n \Delta\psi^{t-\Delta t}}\right] - g_1^t\left[\frac{1-e^{-\lambda_n \Delta\psi^t}}{\lambda_n \Delta\psi^t}\right]\right) \sigma_{kk}^{t-\Delta t}
\end{aligned}, \quad (2.29)$$

defining

$$\begin{aligned}
\widehat{J}^t &= \frac{1}{2}\left[g_0^t J_0 + g_1^t g_2^t \sum_{n=1}^{N} J_n - g_1^t g_2^t \sum_{n=1}^{N} J_n \frac{1-e^{-\lambda_n \Delta\psi^t}}{\lambda_n \Delta\psi^t}\right] \\
\widehat{B}^t &= \frac{1}{3}\left[g_0^t B_0 + g_1^t g_2^t \sum_{n=1}^{N} B_n - g_1^t g_2^t \sum_{n=1}^{N} B_n \frac{1-e^{-\lambda_n \Delta\psi^t}}{\lambda_n \Delta\psi^t}\right]
\end{aligned}.$$

2.3.2 Discrete viscoplastic strain

From (2.9), we approximate the incremental viscoplastic strain

$$\Delta\epsilon_{ij}^{vp,t} = \Gamma\left(\frac{f}{\sigma_y^0}\right)^N \Delta t \frac{\partial g}{\partial \sigma_{ij}} = \Delta\gamma^{vp,t} \frac{\partial g}{\partial \sigma_{ij}}, \quad (2.30)$$

where this gives the definition of the viscoplastic multiplier $\Delta\gamma^{vp,t}$, which can be calculated discretely as

$$\Delta\gamma^{vp,t} = \Delta t\, \Gamma \left(\frac{f(\sigma_{ij}^t, \epsilon_e^{vp,t})}{\sigma_y^0} \right)^N . \tag{2.31}$$

Substituting into (2.26) yields

$$\epsilon_e^{vp,t} = \epsilon_e^{vp,t-\Delta t} + \Delta\gamma^{vp,t} \frac{\sqrt{\frac{\partial g}{\partial \sigma_{ij}} \frac{\partial g}{\partial \sigma_{ij}}}}{1 + 2\left(\frac{1/2+\beta/3}{1-\beta/3}\right)^2}. \tag{2.32}$$

2.3.3 Computational algorithm

For each strain, the algorithm starts with a trial stress (Simo and Hughes 1998) based on the nonlinear viscoelastic stress. If the trial stress exceeds the yield surface, the viscoplastic strain increment is calculated based on a dynamic yield surface (obtained from (2.9) and (2.10)),

$$\chi = \tau^{tr} - \alpha I_1^{tr} - \kappa\left(\epsilon_e^{vp,t-\Delta t}\right) - \sigma_y^0 \left(\frac{\Delta\gamma^{vp,t}}{\Delta t\, \Gamma} \right)^{\frac{1}{N}} . \tag{2.33}$$

To use the Newton-Raphson root-finding algorithm, we calculate the derivative

$$\frac{\partial \chi}{\partial \gamma^{vp}} = -\frac{\partial \kappa}{\partial \Delta\epsilon_e^{vp}} \frac{\partial \Delta\epsilon_e^{vp}}{\partial \gamma^{vp}} - \frac{\sigma_y^0}{N\, \Delta\gamma^{vp}} \left(\frac{\Delta\gamma^{vp}}{\Gamma\, \Delta t} \right)^{\frac{1}{N}}, \tag{2.34}$$

where we can calculate

$$\frac{\partial \kappa}{\partial \Delta\epsilon_e^{vp}} = \frac{\partial}{\partial \Delta\epsilon_e^{vp}} \kappa\left(\epsilon_e^{vp,t-\Delta t} + \Delta\epsilon_e^{vp,t}\right) = \kappa_1\kappa_2 \exp\left(-\kappa_2\left(\epsilon_e^{vp,t-\Delta t} + \Delta\epsilon_e^{vp,t}\right)\right)$$

and

$$\frac{\partial \Delta \epsilon_e^{vp}}{\partial \gamma^{vp}} = \frac{\sqrt{\frac{\partial g}{\partial \sigma_{ij}} \frac{\partial g}{\partial \sigma_{ij}}}}{\sqrt{1 + 2\left(\frac{\frac{1}{2} + \frac{\beta}{3}}{1 - \frac{\beta}{3}}\right)^2}}.$$

After $\frac{\partial \chi}{\partial \gamma^{vp}}$ is calculated, we can iterate the viscoplastic multiplier for the $k+1^{th}$ iteration

$$(\Delta \gamma^{vp})^{k+1} = (\Delta \gamma^{vp})^k - \frac{\chi^k}{\left(\frac{\partial \chi}{\partial \gamma^{vp}}\right)^k}. \tag{2.35}$$

To determine convergence, we calculate the residual strain

$$R_{ij}^t = \Delta \epsilon_{ij}^{ve,t} + \Delta \epsilon_{ij}^{vp,t} - \Delta \epsilon_{ij}^{ve,t}, \tag{2.36}$$

which is the difference between the predicted strain and the actual strain (which is supplied). The trial stress for the next increment is calculated based on residual strain R_{ij}^t to be

$$\left(\Delta \sigma_{ij}^t\right)^{k+1} = \left(\Delta \sigma_{ij}^t\right)^k - \left[\left(\frac{\partial R_{ij}^t}{\partial \sigma_{kl}^t}\right)^k\right]^{-1} \left(R_{kl}^t\right)^k, \tag{2.37}$$

where we can calculate the derivative

$$\frac{\partial R_{ij}^t}{\partial \sigma_{kl}^t} = \frac{\partial \epsilon_{ij}^{ve,t}}{\partial \sigma_{kl}^t} + \frac{\partial \epsilon_{ij}^{vp,t}}{\partial \sigma_{kl}^t}, \tag{2.38}$$

where

$$\frac{\partial \epsilon_{ij}^{ve,t}}{\partial \sigma_{kl}^t} = \widehat{J}^t \delta_{ik} \delta_{jl} + \frac{1}{3}\left(\widehat{B}^t - \widehat{J}^t\right) \delta_{ij} \delta_{kl} + \frac{\partial \hat{\sigma}^t}{\partial \sigma_{kl}^t}\left[\frac{\partial \widehat{J}^t}{\partial \hat{\sigma}^t} + \frac{1}{3}\left(\frac{\partial \widehat{B}^t}{\partial \hat{\sigma}^t} - \frac{\partial \widehat{J}^t}{\partial \hat{\sigma}^t}\right) \sigma_{kk}^t \delta_{ij}\right.$$

$$
\begin{aligned}
&- \frac{1}{2}\frac{\partial g_1^t}{\partial \hat{\sigma}^t}\sum_{n=1}^{N_p} J_n \left(e^{-\lambda_n \Delta\psi^t} q_{ij,n}^{t-\Delta t} - g_2^{t-\Delta t}\frac{1-e^{-\lambda_n\Delta\psi^t}}{\lambda_n\Delta\psi^t} S_{ij}^{t-\Delta t} \right) \\
&- \frac{1}{2}\frac{\partial a_\sigma^t}{\partial \hat{\sigma}^t} g_1 \sum_{n=1}^{N_p} J_n \left(e^{-\lambda_n \Delta\psi^t} \left(\frac{\lambda_n q_{ij,n}^{t-\Delta t}\Delta t}{\left(a_\sigma^t\right)^2} S_{ij}^{t-\Delta t} + g_2^{t-\Delta t}\frac{S_{ij}^{t-\Delta t}}{a_\sigma^t} \right) \right. \\
&\qquad\qquad \left. - g_2^{t-\Delta t}\frac{1-e^{-\lambda_n\Delta\psi^t}}{\lambda_n\Delta\psi^t} S_{ij}^{t-\Delta t} \right) \\
&- \frac{1}{9}\frac{\partial g_1^t}{\partial \hat{\sigma}^t}\sum_{n=1}^{N_p} B_n \left(e^{-\lambda_n \Delta\psi^t} q_{kk,n}^{t-\Delta t} - g_2^{t-\Delta t}\frac{1-e^{-\lambda_n\Delta\psi^t}}{\lambda_n\Delta\psi^t} \sigma_{kk}^{t-\Delta t} \right) \delta_{ij} \\
&- \frac{1}{9}\frac{\partial a_\sigma^t}{\partial \hat{\sigma}^t} g_1 \sum_{n=1}^{N_p} B_n \left(e^{-\lambda_n \Delta\psi^t} \left(\frac{\lambda_n q_{kk,n}^{t-\Delta t}\Delta t}{\left(a_\sigma^t\right)^2} \sigma_{kk}^{t-\Delta t} + g_2^{t-\Delta t}\frac{\sigma_{kk}^{t-\Delta t}}{a_\sigma^t} \right) \right. \\
&\qquad\qquad \left. - g_2^{t-\Delta t}\frac{1-e^{-\lambda_n\Delta\psi^t}}{\lambda_n\Delta\psi^t} \sigma_{kk}^{t-\Delta t} \right) \delta_{ij} \Bigg] \qquad (2.39)
\end{aligned}
$$

(where $\hat{\sigma}^t$ is a scalar measure of stress which may be used for the nonlinear and shift parameters) and

$$
\begin{aligned}
\frac{\partial \epsilon_{ij}^{vp,t}}{\partial \sigma_{kl}^t} &= \frac{\partial}{\partial \sigma_{kl}^t}\left(\Delta\gamma^{vp,t} \frac{\partial g}{\partial \sigma_{ij}} \right) \\
&= \frac{\Delta t \Gamma N}{\sigma_y^0}\left(\frac{f}{\sigma_y^0}\right)^{N-1} \frac{\partial g}{\partial \sigma_{ij}}\frac{\partial f}{\partial \sigma_{kl}} + \Delta t\Gamma\left(\frac{f}{\sigma_y^0}\right)^N \frac{\partial^2 g}{\partial \sigma_{ij}\partial\sigma_{kl}}. \qquad (2.40)
\end{aligned}
$$

Huang (2008) verified this numerical model as derived here and implemented using a UMAT subroutine in the commercial finite element code Abaqus by comparing it to analytical results.

Figure 2.5 shows the numerical algorithm for calculating the stress. If viscoplasticity occurs, Figure 2.5 requires calculation of the viscoplastic strain increment, the calculation of which is illustrated by the flow chart in Figure 2.6.

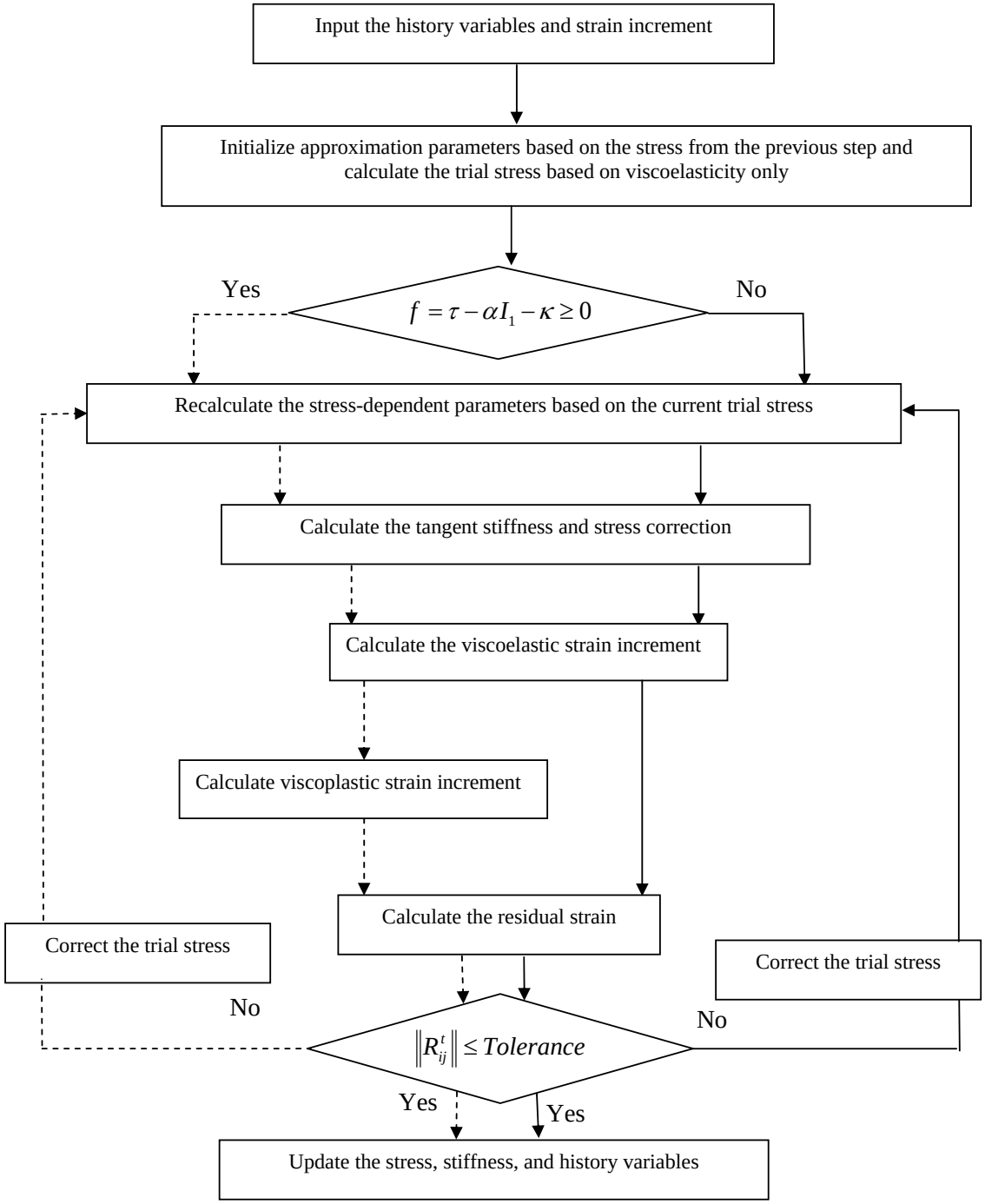

Figure 2.5 Flow chart showing the numerical algorithm to calculate the stress (Huang 2008)

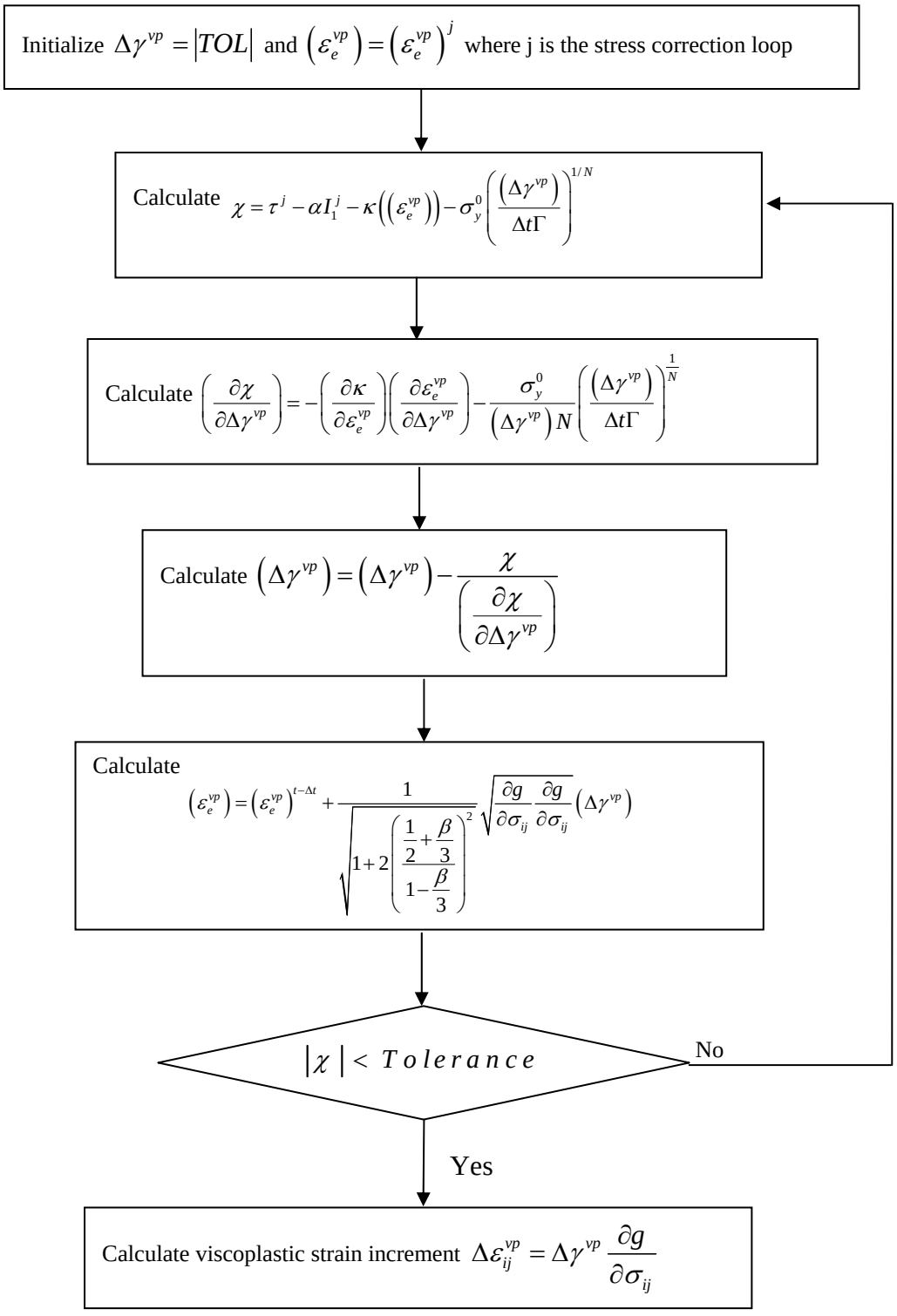

Figure 2.6 Flow chart showing the numerical algorithm to calculate the viscoplastic strain increment (Huang 2008)

Table 2.1 Viscoelastic Material Parameters

n	λ_n (1/s)	J_n (1/kPa)
1	1.0	1.15×10^{-6}
2	0.1	1.49×10^{-6}
3	0.01	3.17×10^{-6}
4	0.001	6.37×10^{-6}
5	0.0001	2.61×10^{-6}
6	0.00001	96.1×10^{-6}
J_0	—	0.675×10^{-6}

2.4 Parametric Study

2.4.1 Viscoelastic parameters

This section presents the results of a parametric study of the viscoelastic nonlinear parameters from a series of compressive creep–recovery simulations in Abaqus. The results are reported at one integration point subjected to uniaxial stress of 50 kPa for 30 s then allowed to recover for 30 s. The material properties used in the simulations are presented in Table 2.1.

Figure 2.7 shows the strain response for varying the parameter g_0. Figure 2.8 shows the strain response for varying the parameters g_1 and g_2 coupled as $g_1 g_2$.

2.4.2 Viscoplastic parameters

This section presents the results of a parametric study for all of the viscoplastic material parameters from a series of simulations in Abaqus. The results are reported at one integration point subjected to uniaxial strain at constant strain rate $\dot{\epsilon} = 0.0015\,\mathrm{s}^{-1}$ for 60 seconds. In all cases uniaxial compression is simulated and in some cases it was deemed important to present results from simulations of uniaxial tension as well. All material parameters are held constant at the values from Table 2.2 (which may represent reasonable values for asphalt concrete) except the parameter being studied.

Figure 2.9 shows the effect of the yield surface parameter α, which controls

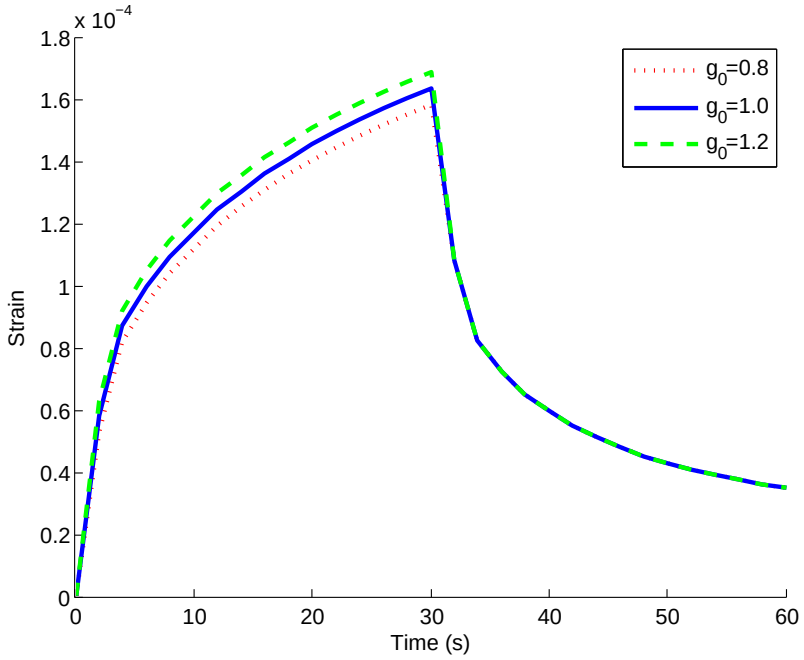

Figure 2.7 Effect of the viscoelastic nonlinear parameter g_0

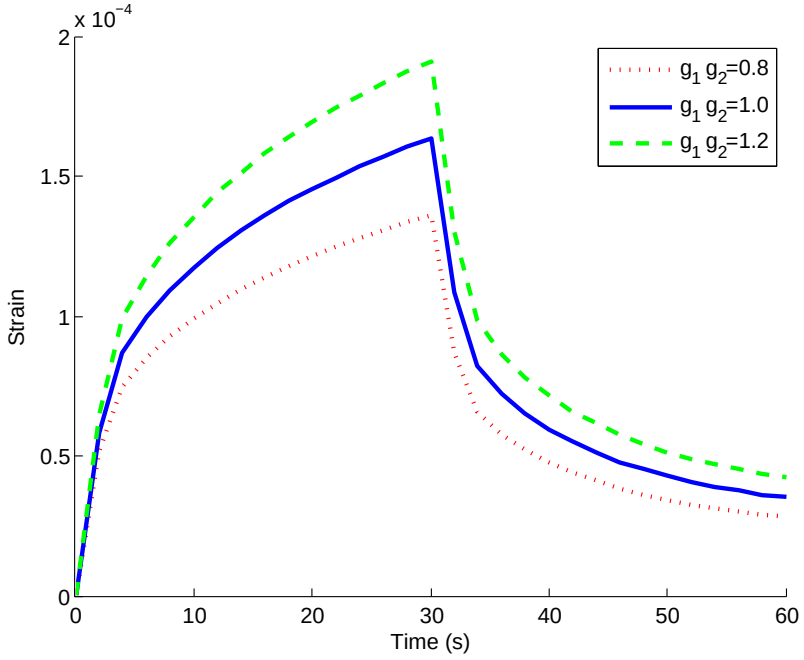

Figure 2.8 Effect of the viscoelastic nonlinear parameters g_1 and g_2

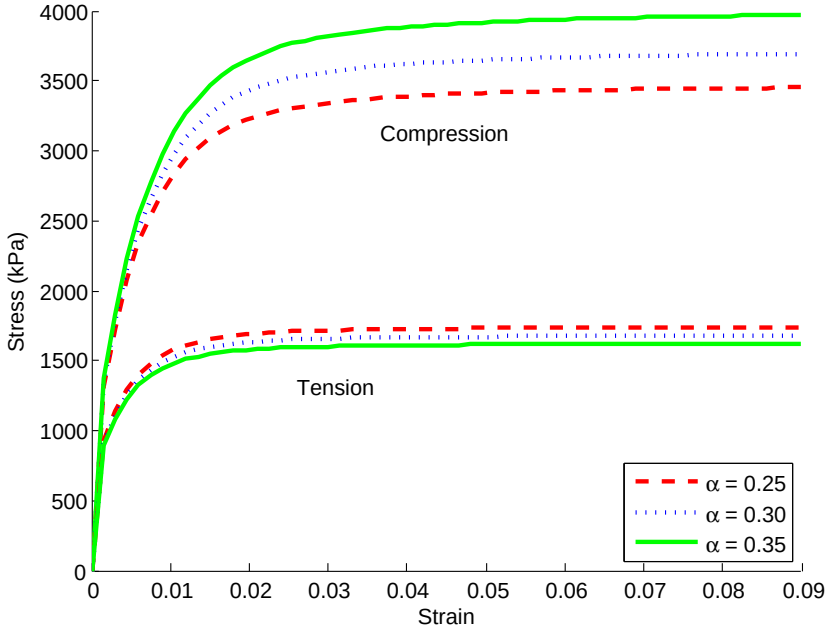

Figure 2.9 Effect of the yield surface parameter α

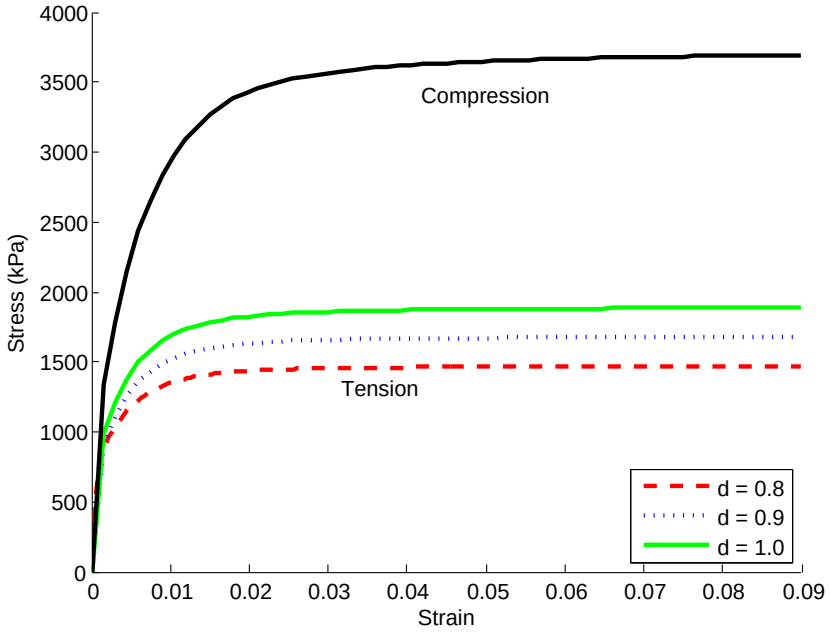

Figure 2.10 Effect of the yield surface parameter d

Table 2.2 Viscoplastic Material Parameters

Property	Value
α	0.3
d	0.9
σ_y^0	35 kPa
β	0.25
Γ	$5 \times 10^{-7}\text{s}^{-1}$
N	2.0
κ_0	35 kPa
κ_1	600 kPa
κ_2	290

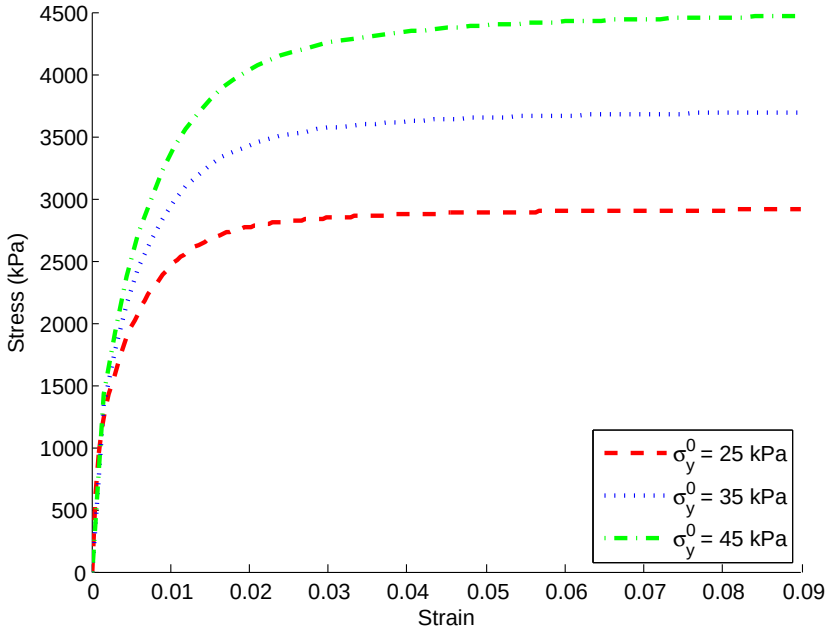

Figure 2.11 Effect of the yield surface parameter σ_y^0

the pressure sensitivity of the yield surface. For lower values of α, the tensile and compressive responses are more similar. Figure 2.10 shows the effect of the yield surface parameter d, which serves to constrict the yield surface while the material undergoes extension, regardless of pressure. Notice that when the material is not

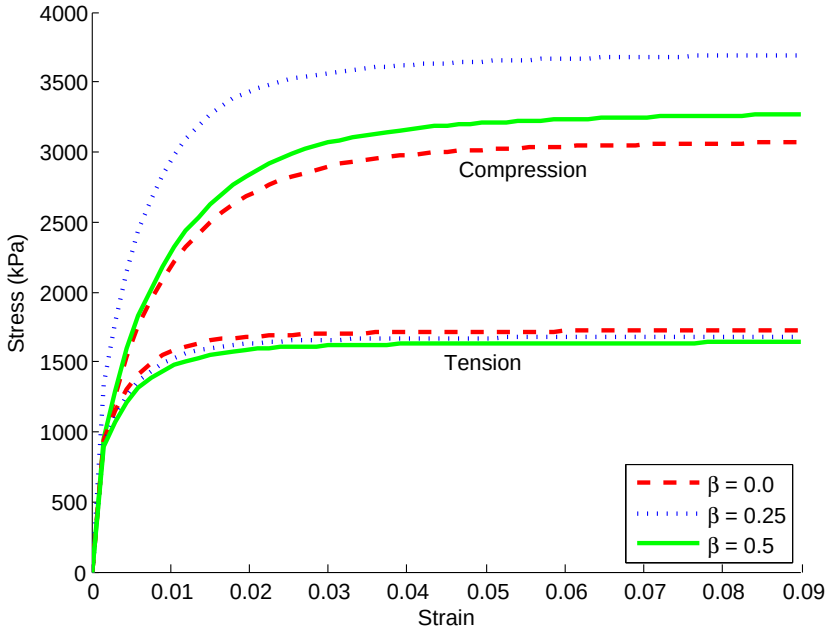

Figure 2.12 Effect of the viscoplastic potential energy parameter β

being extended, d has no effect on the response. Figure 2.11 shows the effect of the yield surface parameter σ_y^0, which simply amplifies the yield surface.

Figure 2.12 shows the effect of the flow function parameter β, which makes the flow function pressure sensitive. As β increases, the plastic strain in compression decreases (i.e. the material is more stiff, as seen on the graph) and the plastic strain in tension increases (and hence the graph shows a more compliant response for higher values of β.) Figure 2.13 shows the effect of the viscosity parameter Γ, which controls the amount of plastic strain based on the energy dissipated. Larger values of Γ correspond to more flow (and therefore smaller stresses). Figure 2.14 shows the effect of the strain rate exponent N; greater values of N result in more flow.

Figures 2.15, 2.16, and 2.17 show the effect of the hardening function parameters κ_0, κ_1, and κ_2, and are best understood by understanding the hardening function κ, which is shown in Figure 2.4. The value of the hardening function $\kappa(\epsilon_e^{vp})$ varies

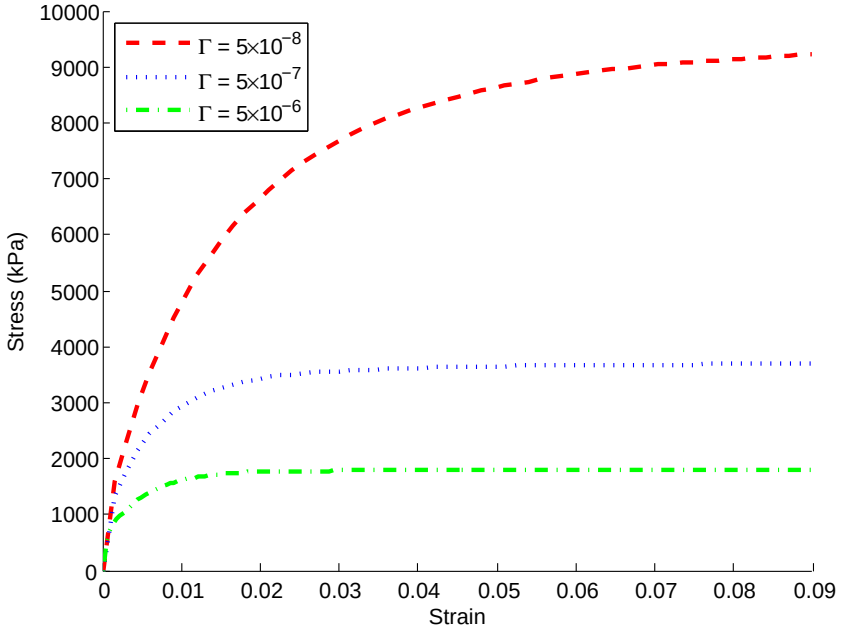

Figure 2.13 Effect of the flow function parameter Γ

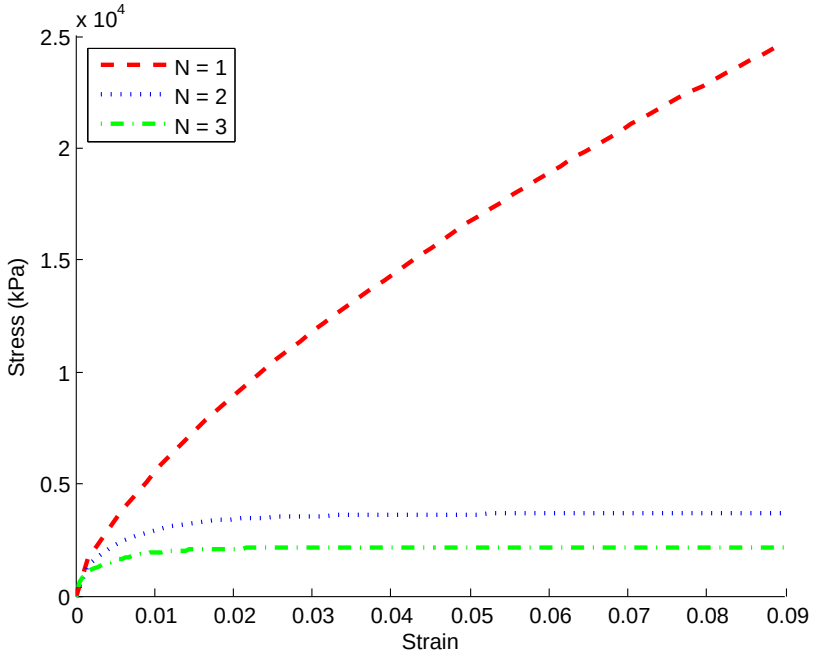

Figure 2.14 Effect of the flow function parameter N

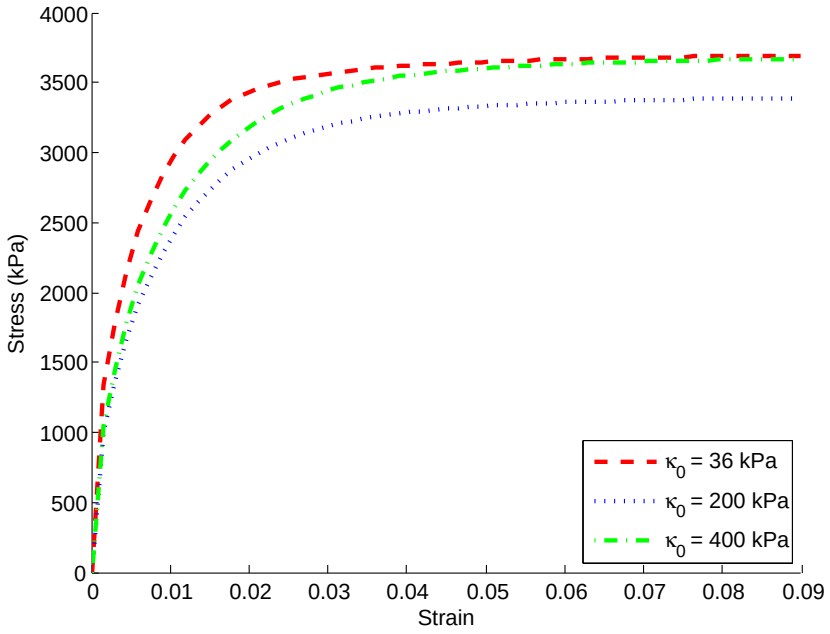

Figure 2.15 Effect of the hardening function parameter κ_0 on the stress–strain response

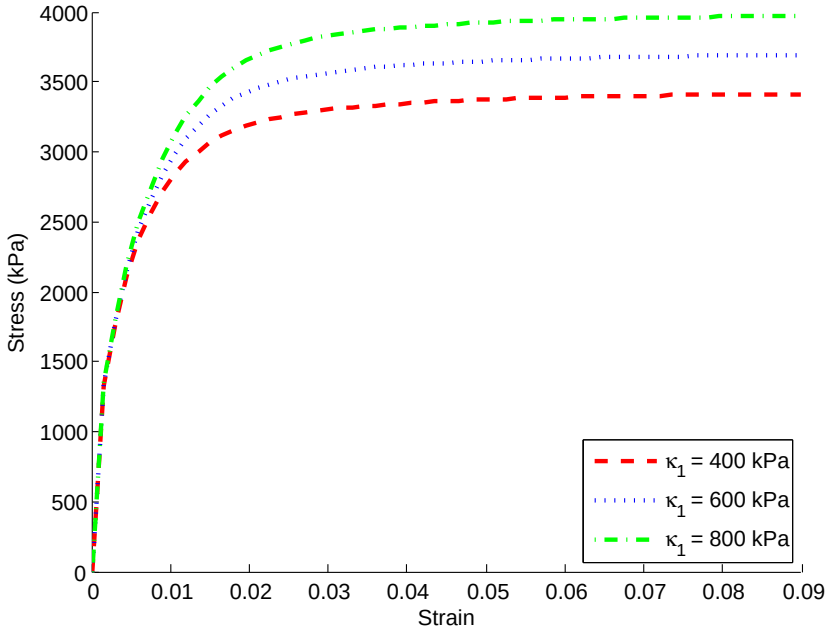

Figure 2.16 Effect of the hardening function parameter κ_1 on the stress–strain response

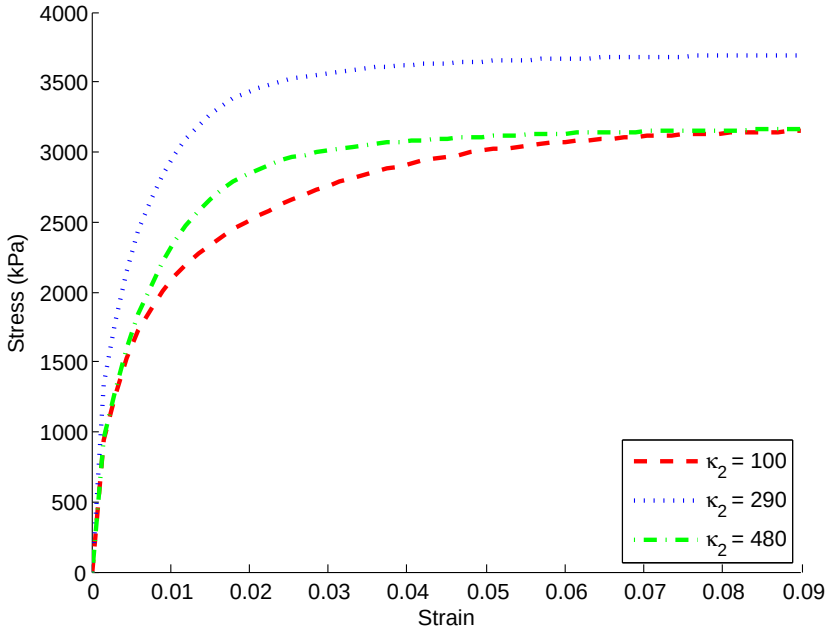

Figure 2.17 Effect of the hardening function parameter κ_2 on the stress–strain response

from κ_0 when $\epsilon_e^{vp} = 0$ (before viscoplasticity occurs) to $\kappa_0 + \kappa_1$ as $\epsilon_e^{vp} \to \infty$, and κ approaches the saturated value $\kappa_0 + \kappa_1$ more quickly as κ_2 increases. Figures 2.15 and 2.16 show the effects of κ_0 and κ_1 on the stress–strain behavior such that a decrease in either κ_0 or κ_1 decreases the value of the hardening function κ and results in a more compliant material. Figure 2.17 shows the effect of κ_2 on the stress–strain behavior, where the material yields more (has more flow) earlier for lower values of κ_2.

3 MECHANICALLY-INDUCED DAMAGE

One major cause of degradation in asphalt pavements is mechanical loading of the pavements, especially due to trucks driving over asphalt roadways, so a thorough model describing the degradation of asphalt pavements must include the effects of mechanical loads. The proposed model uses CDM to model the degradation of an asphalt concrete body subject to mechanical loads.

Modeling asphalt concrete (and composite materials in general) requires some generalization of CDM because the it is unreasonable to assume microcracks and microvoids are distributed completely randomly, since an asphalt mix is very heterogeneous at the scale of microcracks. Further, the phases of asphalt concrete mixes vary greatly in their contributions to the strength and stiffness of a mix, so it is not reasonable to equate the damage variable to the proportion of the material occupied by microcracks and microvoids.

However, asphalt concretes exhibit damage behavior like that predicted by CDM: as loading becomes severe, the material softens and when it is unloaded, its stiffness is reduced compared to the recovery stiffness after less severe loading. Therefore, CDM is used, with the damage variable ϕ^m which does not indicate any specific volumetric distribution of microcracks and voids, but instead arises directly from the energy dissipated through fracture causing loss of strength and stiffness of the material, and is the proper quantity to indicate the amount of stiffness that is lost.

3.1 Damage Law

3.1.1 Modified mechanical response

The mechanically-induced damage relates the predicted response to that of the undamaged material by

$$\sigma_{ij}(t) = \frac{1}{\left(1-\phi^m(t)\right)^2}\,\bar{\sigma}_{ij}(t), \tag{3.1}$$

where σ_{ij} is the *nominal stress* for the body and $\bar{\sigma}_{ij}$ is the *effective stress*, which is the stress level experienced by the material still effective at resisting loads, which is calculated using the material model presented in Section 2.

The Abaqus UMAT subroutine is modified according to this relation: the stress used for the finite element mesh is the nominal stress, but the undamaged material model is used to calculate the effective stress $\bar{\sigma}_{ij}(t)$. The two relate by ϕ^m, which is calculated as described in this section.

3.1.2 Driving force

The driving force for mechanical damage postulated to be

$$Y^m = \bar{\tau} - \alpha \bar{I}_1, \quad \bar{\tau} = \frac{\sqrt{3\bar{J}_2}}{2}\left(1+\frac{1}{d}+\left(1-\frac{1}{d}\right)\frac{\bar{J}_3}{\sqrt{3\bar{J}_2^3}}\right), \tag{3.2}$$

where $\bar{I}_1$, $\bar{J}_2$, and $\bar{J}_3$ are stress invariants (calculated from the *effective stress* $\bar{\sigma}_{ij}$) and α and d are material parameters, and all are defined and described in Section 2. This form resembles the viscoplastic yield surface and is appropriate because its properties reflect the physical behavior of asphalt concrete.

The mechanical damage is based on the state of stress, so the driving force increases more severe states of stress. The mechanical damage is *pressure sensitive*, so that for tensile states of stress, the driving force is greater than for an analogous

compressive state of stress, which in this model is due to the term αI_1, such that (for $\alpha > 0$) compressive pressures $I_1 > 0$, the damage force is less than τ and for tensile pressures $I_1 < 0$, the damage force is greater than τ.. The mechanical damage is sensitive to extension, so that extensions *even under hydrostatic compression*, the damage force is greater for extensions in a compressive case than further compressions; this effect is due to the form of τ and is controlled by the constant d. If $d = 1$, this effect vanishes and τ is exactly the von Mises stress; as d decreases, this effect is amplified. Because the damage surface is analogous to the viscoplastic yield surface, see Figures 2.1, 2.2, and 2.3 on on pages 20–22 for visualizations of the effects of the parameters α and d.

3.1.3 Damage evolution

The evolution of damage is treated similarly to plasticity. To determine whether damage occurs and how it evolves through time, a damage surface G is defined to be

$$G = Y^m - Y^m_{\text{th}} \leq 0, \tag{3.3}$$

where Y^m is the damage force (defined in the previous section) and Y^m_{th} is the *threshold damage force* which is the damage force for which damage starts to occur. Should the damage surface G reach 0, damage occurs, leading to the condition

$$G = Y^m - Y^m_{\text{th}} - \kappa_\phi(\phi^m) = 0, \tag{3.4}$$

where $\kappa_\phi(\phi^m)$ is the *isotropic damage function*, which governs the evolution of the damage. For this study we choose

$$\kappa_\phi(\phi^m) = \frac{Y^m_{\text{th}}}{k^m} \ln(1 - \phi^m), \tag{3.5}$$

where k^m is the *mechanical damage growth parameter*, which governs the evolution rate of damage. To gain greater intuition and for implementation, we substitutive (3.5) into (3.4) and rearrange to yield

$$\phi^m = 1 - \exp\left(k^m \frac{Y_{\text{th}}^m - Y^m}{Y_{\text{th}}^m}\right). \tag{3.6}$$

This model is chosen because it matches the physical expectations that (1) when damage first occurs, its value is $\phi^m = 0$, (2) damage accumulates more and more as loading becomes more severe, and (3) the damage variable will not exceed unity ($\phi^m < 1$) and because exponential damage growth has frequently been observed in experiments for other materials (Cicekli et al. 2007, Abu Al-Rub and Voyiadjis 2009).

3.2 Parametric Study

Two material parameters, Y_{th}^m and k^m, are introduced for mechanical damage, and two more, α and d, affect the mechanical damage and are already defined for viscoplasticity. To understand them, a parametric sensitivity study examines the various parameters' effects on the response and their experimental determination is discussed.

This section presents the results of a parametric study for all of the damage material parameters from a series of simulations in Abaqus. The results are reported at one integration point subjected to uniaxial strain at constant strain rate $\dot{\epsilon} = 0.0015\,\text{s}^{-1}$ for 60 seconds (unless otherwise noted). In all cases uniaxial compression is simulated and in some cases it is deemed important to present results from simulations of uniaxial tension. All material parameters are held constant at the values from Table 3.1 except the parameter being studied.

Figure 3.1 shows how the stress–strain response changes due to varying the mechanical damage parameter k^m, and Figure 3.2 shows the evolution of the mechanical

Table 3.1 Damage Material Parameters

Property	Value
Y_{th}^m	2000kPa
k^m	0.08
α	0.3
d	0.9

damage variable ϕ^m through the simulations varying k^m. After damage begins to accumulate when the damage force Y^m reaches the threshold damage force Y_{th}^m, the mechanical damage parameter controls the severity of damage, where larger values of k^m indicate more damage (larger values of ϕ^m) and hence a less stiff material. Figure 3.3 shows how the stress–strain response changes due to varying the threshold mechanical damage force Y_{th}^m, and Figure 3.4 shows the evolution of the mechanical damage variable ϕ^m through the simulations varying Y_{th}^m. All else held equal, large values of Y_{th}^m cause damage to begin later, and to be less severe.

Remember when examining Figures 3.5–3.8 that varying α and d also affects the viscoplastic response of the material. Figure 3.5 shows how the stress–strain response changes due to varying the parameter α, and Figure 3.6 shows the evolution of the mechanical damage variable ϕ^m through the simulations varying α. As α decreases, the compressive and tensile stress–strain behaviors become more similar, as α introduces pressure sensitivity to the model. Larger values of α result in less mechanical damage in compression and more mechanical damage in tension.

The results for the effect of d are most clearly seen in a stress-controlled regime, so Figures 3.7 and 3.8 present the results of constant stress rate tests with the stress rates $\dot{\sigma} = 58\,\text{kPa/s}$ for compression and $\dot{\sigma} = 28\,\text{kPa/s}$ for tension. Figure 3.7 shows how the stress–strain response changes due to varying the parameter d, and Figure 3.8

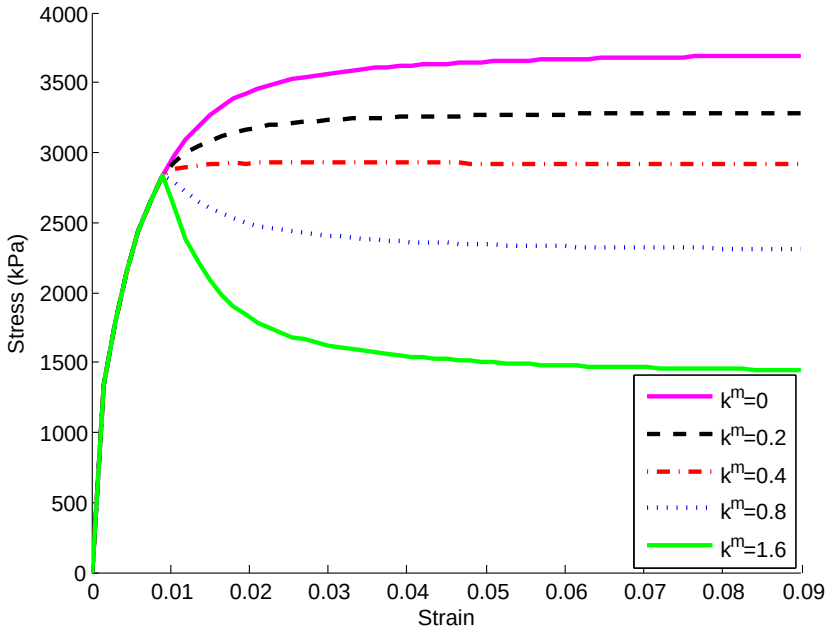

Figure 3.1 Effect of the mechanical damage growth parameter k^m on the stress–strain response from constant strain rate simulations

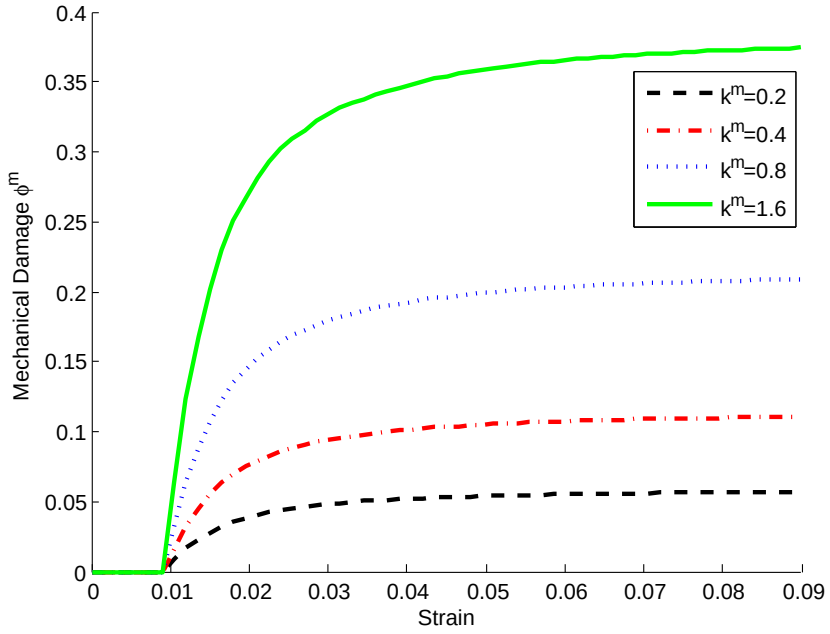

Figure 3.2 Effect of the mechanical damage growth parameter k^m on the mechanical damage ϕ^m from constant strain rate simulations

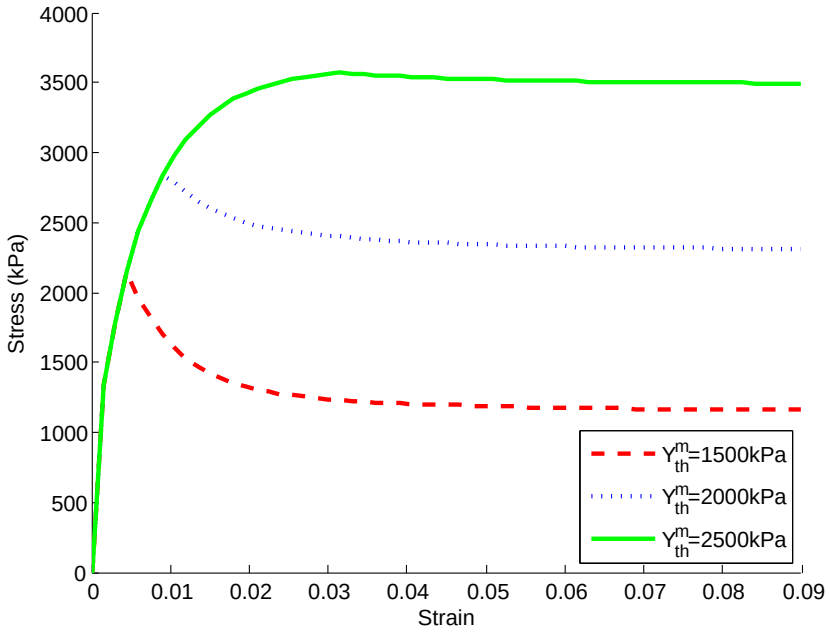

Figure 3.3 Effect of the threshold damage force Y_{th}^m on the stress–strain response from constant strain rate simulations

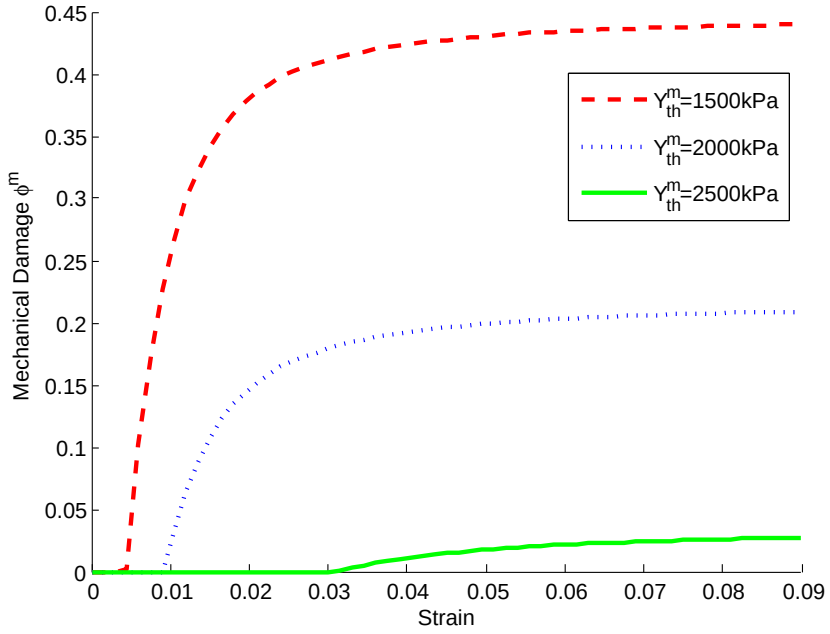

Figure 3.4 Effect of the threshold damage force Y_{th}^m on the mechanical damage ϕ^m from constant strain rate simulations

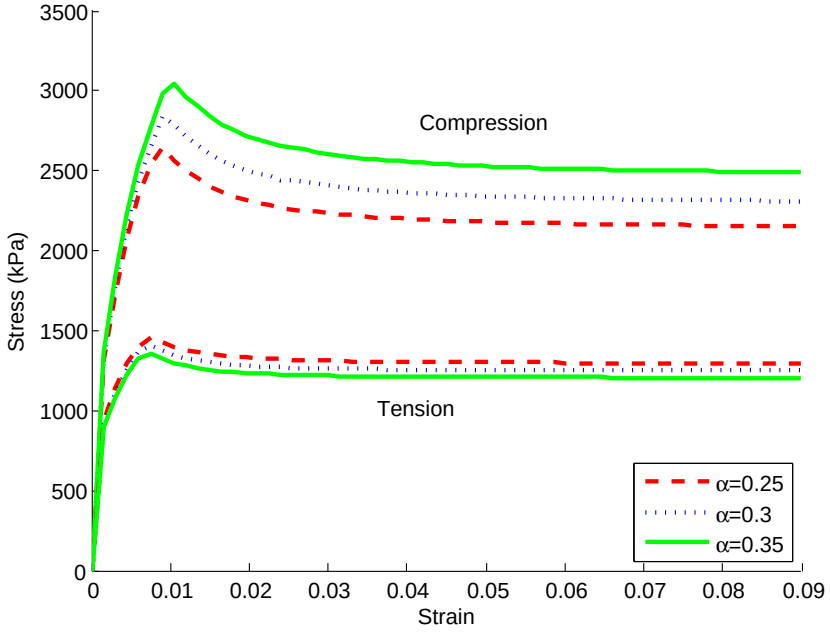

Figure 3.5 Effect of the damage force parameter α on the stress–strain response

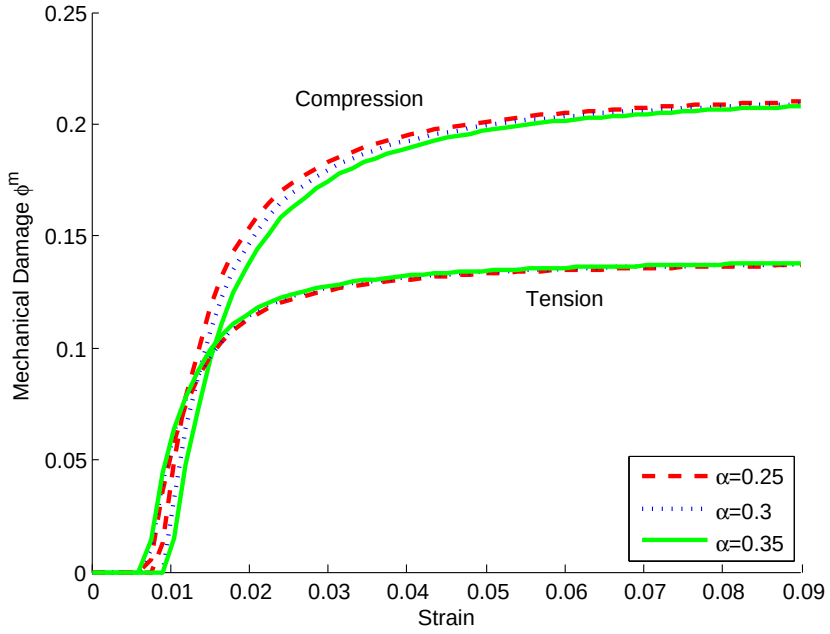

Figure 3.6 Effect of the damage force parameter α on the mechanical damage ϕ^m

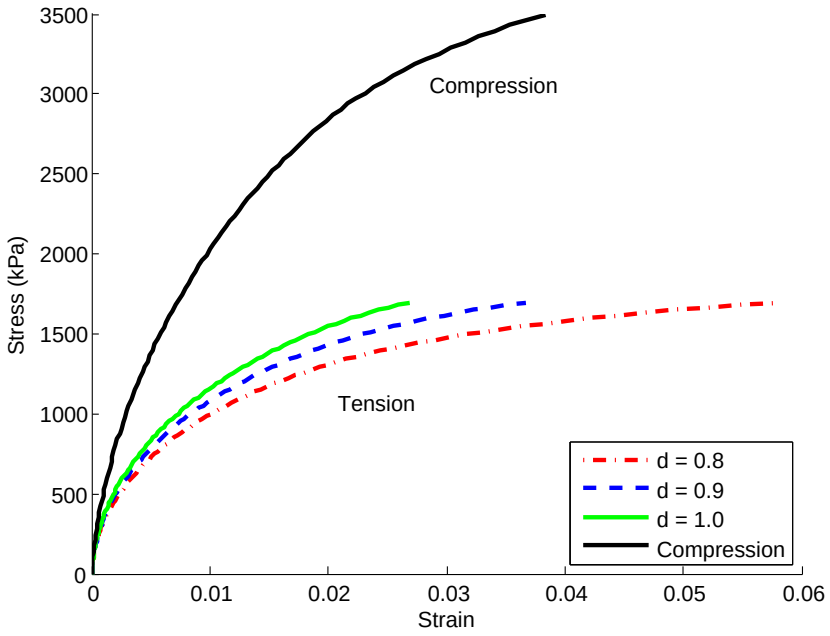

Figure 3.7 Effect of the damage force parameter d on the stress–strain response from constant stress rate simulations

shows the evolution of the mechanical damage variable ϕ^m through the constant stress rate simulations varying d.

3.3 Rate Dependence

Experiments have indicated that the damage accumulation in asphalt concrete is dependent on the load history (Grenfell et al. 2008). Consider the results of uniaxial, compressive constant strain rate laboratory tests shown in Figure 3.9.

At faster strain rates, the asphalt concrete is more resilient in resisting loads. It exhibits stiffer initial (viscoelastic) response, then in the viscoplastic–damaged regime, the same qualitative behavior occurs at higher stresses and slightly higher strains. The maximum peak of the stress–strain graph relates to Y^m_{th} and the rate of softening relates to k^m/Y^m_{th}. An initial attempt to quantify the strain rate effect is a modified

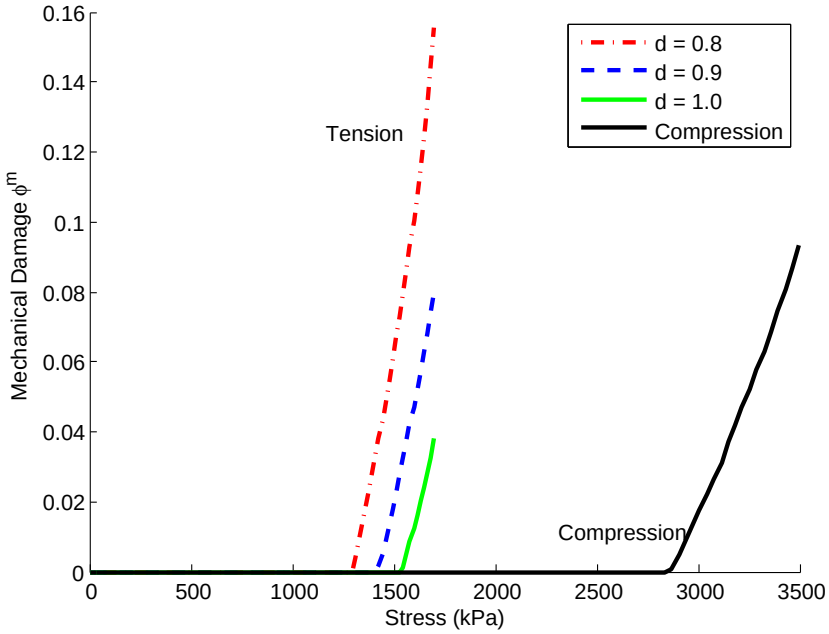

Figure 3.8 Effect of the damage force parameter d on the mechanical damage ϕ^m from constant stress rate simulations

threshold damage force

$$Y_{\text{th}}^m(\dot{\epsilon}_{11}) = \eta_\phi \, 2^{\log_{10} \dot{\epsilon}_{11}}, \tag{3.7}$$

where η_ϕ is a material constant, the characteristic viscosity of mechanical damage. Though this law is probably inappropriate for general loading histories, it provides some insight into rate effects for damage.

Equation (3.7) is developed specifically for the uniaxial case. For general loading, a scalar must represent the strain rate, so we define the *equivalent total strain rate*

$$\dot{\epsilon}_e^{\text{tot}} = \sqrt{\dot{\epsilon}_{ij}\dot{\epsilon}_{ij}}, \tag{3.8}$$

which is analogous to the equivalent viscoplastic strain rate ϵ_e^{vp} in (2.25). The measure of strain used is the total strain ϵ_{ij} in place of the viscoplastic strain ϵ_{ij}^{vp}, because the

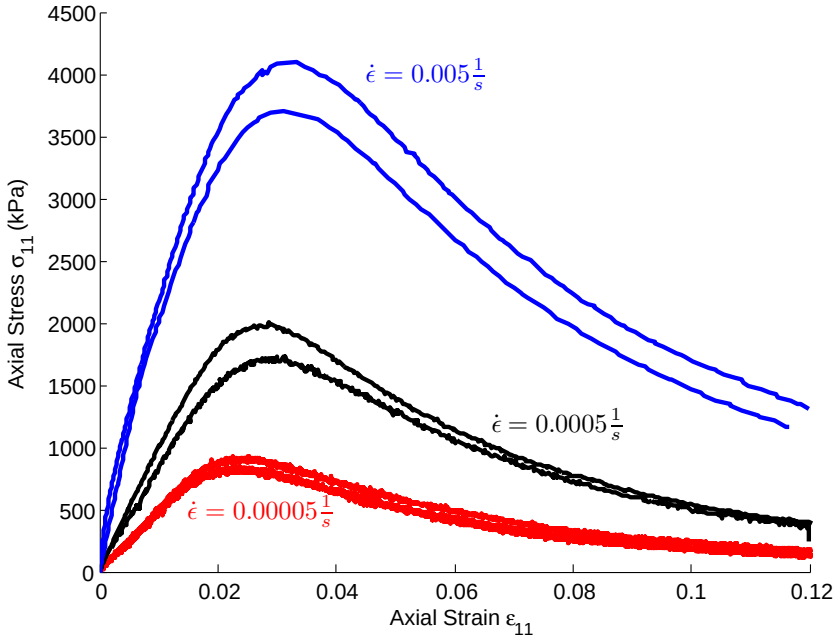

Figure 3.9 Stress–strain relationship for asphalt from a series of uniaxial, compressive constant strain rate tests at various strain rates. The results of two tests at each of the strain rates $\dot{\epsilon}_{11} = 0.005$, 0.0005, and 0.00005 are presented (Grenfell et al. 2008)

total response will contribute to damage in an asphalt mix, not only the viscoplastic component. The threshold damage force is

$$Y_{\text{th}}^{m}(\dot{\epsilon}_{ij}) = A2^{\log_{10}\dot{\epsilon}_{e}^{\text{tot}}}, \tag{3.9}$$

for the case of three-dimensional stress states.

4 MOISTURE-INDUCED DAMAGE

Moisture damage contributes heavily to the premature degradation of asphalt pavements, resulting in expensive rehabilitation and replacement costs for roadways and potential hazard in the case of severely damaged roadways (Kandhal 1994, Copeland 2005, Kringos 2007).

Despite the detrimental effects of moisture damage, no macroscale model exists to model moisture-induced damage in asphalt concrete. The effect of moisture in degrading the mechanical properties is observed in two mechanisms: the loss of the adhesive bond between the aggregates and the mastic and the loss of the cohesive strength of the mastic (Caro et al. 2008a, Kringos et al. 2007). These mechanisms are modeled independently, but with the same method.

4.1 Damage Law

The degrading effect of moisture manifests in two physical phenomena: (1) adhesive moisture damage (corresponding to the damage variable ϕ^a) which is the degradation of the bond strength between the aggregates and the asphalt mastic due to the existence and diffusion of moisture through the thin films surrounding the aggregate particles and along the aggregate-mastic interfaces; and (2) cohesive moisture damage (corresponding to ϕ^c) which is the degradation of the cohesive strength of the asphalt mastic. In this study and for the first time, both of these phenomena are modeled independently, which allows one to introduce fundamental mechanical properties for each process (e.g., bond strength and cohesive strength) and model the transition between adhesive and cohesive damage.

The decay in the aggregate-mastic bond strength and mastic cohesive strength

due to the presence of moisture is modeled using the evolution law

$$X^i(t) = X_0^i + \int_0^t \dot{X}^i(\theta(\xi))\, d\xi, \quad i = a, c \tag{4.1}$$

where $X^i(t)$ is the average aggregate–mastic adhesive strength of the aggregate-mastic bond for $i = a$ (adhesive) and the average mastic cohesive strength for $i = c$ (cohesive) at time t, X_0^i is the initial undamaged adhesive or cohesive strength (for $i = a, c$), and $\dot{X}^i(\theta(\xi))$ is the rate of decay of the average adhesive or cohesive strength for a normalized moisture content θ at time ξ. Time $t = 0$ is some time before moisture diffusion begins.

This evolution equation for degradation of the adhesive and cohesive strength (which will be used to describe the damage of the mix due to moisture) is an improvement over past approaches which describe the moisture-induced damage as dependent on the current state of the moisture only, not the moisture history (Kringos 2007, Kringos et al. 2007). Though some healing is observed for asphalt concrete, this is not accurately described by an instantaneous, full recovery of strength upon the change in moisture state.

For simplicity, the rate of decay $\dot{X}^i(\theta)$ is described by the linear equation

$$\dot{X}^i(\theta(t)) = -k^i \theta(t), \quad i = a, c\ , \tag{4.2}$$

where k^i $(i = a, c)$ are material properties describing the rate of degradation of the adhesive or cohesive strength. Note that the k^i should be positive so that the rate of change in the strength is negative so that the value of the adhesive or cohesive strength in (4.1) is decreasing, i.e. degradation occurs.

The value of the corresponding damage variable is

$$\phi^i = 1 - \frac{X^i(t)}{X_0^i}, \quad i = a, c \ , \tag{4.3}$$

which is the simplest law which performs as expected: if the adhesive or cohesive strength is its initial value $X^i(t) = X_0^i$, there is no damage ($\phi^i = 0$) and when all adhesive or cohesive strength is lost $X^i(t) = 0$, the material is completely degraded ($\phi^i = 1$), and at intermediate values ϕ^i varies from 0 to 1.

4.1.1 Numerical implementation

The Abaqus simulations and UMAT subroutine are modified to consider the effects of moisture damage. To simulate the dispersion of moisture, the diffusion equation is solved using Abaqus's built-in facilities for solving non-steady state heat problems, where relative humidity is used in place of temperature. The diffusion coefficient for hot mix asphalt was determined by Kassem (2006).

Equation (4.1) is solved discretely, so that at time t following a time step of Δt (substituting the material law in Equation (4.2)),

$$X^{i,t} = X^{i,t-\Delta t} - k^i \theta^t \Delta t, \quad i = a, c \ , \tag{4.4}$$

with an initial value

$$X^{i,t=0} = X_0^i, \quad i = a, c \tag{4.5}$$

indicating a material initially undamaged by moisture.

4.2 Moisture Damage–Mechanical Damage Coupling

It is expected that a material will become more susceptible to mechanical damage due to moisture exposure, and since there are no special laws postulated for coupling mechanical and moisture damage is not instantly clear whether this coupling is

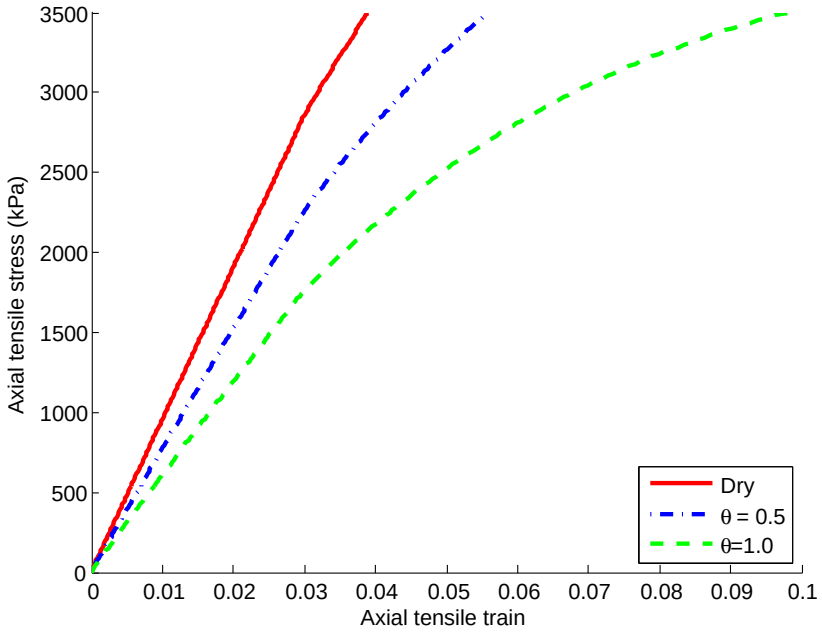

Figure 4.1 Stress–strain diagrams due to stress-controlled loads for various moisture exposures

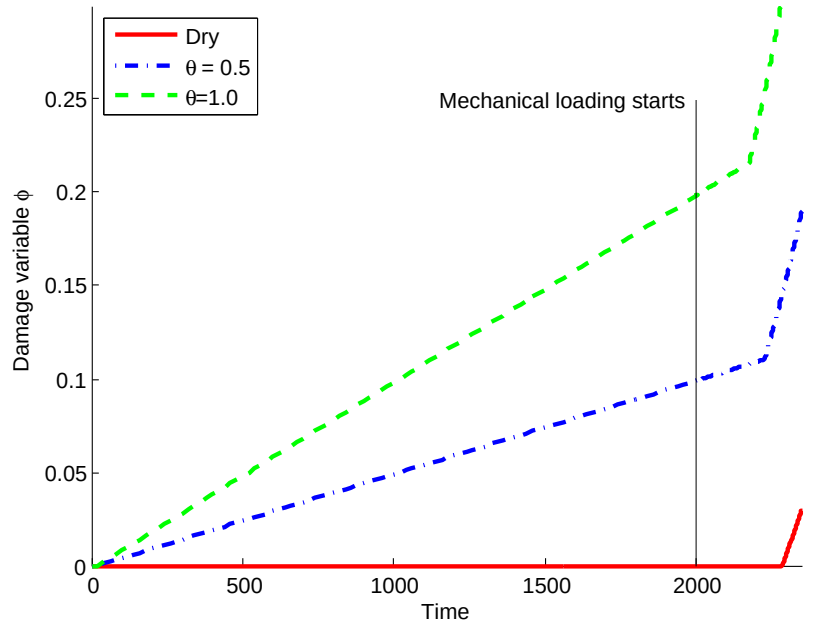

Figure 4.2 The evolution of damage variable ϕ due to stress-controlled loads with time for various moisture exposures

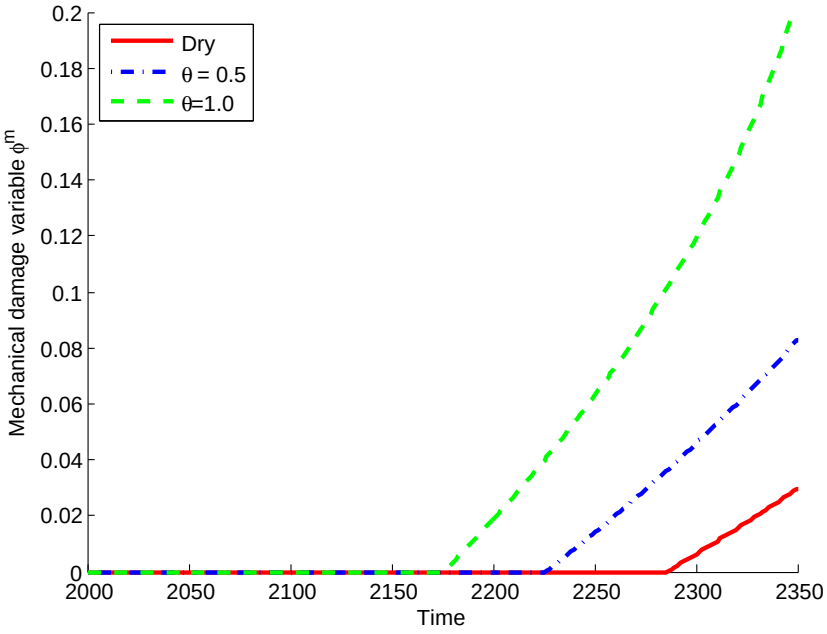

Figure 4.3 The evolution of mechanical damage variable ϕ^m due to stress-controlled loads with time for various moisture exposures

described by the damage model presented here.

In fact, intrinsic coupling exists due to stress-controlled loading, but not strain-controlled loading, because the mechanical damage is driven by the effective stress $\bar{\sigma}_{ij}$ (recall Equation (3.2)). Thus, in the presence of moisture damage an applied stress is amplified (Equation (3.1)) to calculate the damage driving force, but in the case of strain-controlled damage, the effective stress is calculated due to the strain, which does not change because of the formulation $\epsilon = \bar{\epsilon}_{ij}$ (Equation (1.6)).

To illustrate this coupling, several simulations were performed with constant stress rate loading after moisture exposure at various levels. To isolate damage effects, the material law used is elastic–damaged, with material properties Young's modulus $E = 100\,\text{MPa}$, $Y^m_{th} = 2\,\text{MPa}$, $k^m = 0.1$, $X^a_0 = 100.0$, $k^a = 0.01$, and $k^c = 0$. The material is subjected to the specified moisture level for 2000 seconds before loading

in tension at stress rate $\dot{\sigma} = 10\,\mathrm{MPa/s}$.

Figure 4.1 plots the resulting stress–strain diagrams, showing the greater the moisture exposure, the weaker the material is, and that this weakening is more than proportional to the moisture effects. Figure 4.2 plots the evolution of the damage variable ϕ. Before time $t = 2000$ seconds there is no mechanical loading, so all of the damage is due to moisture. Some time after mechanical loading starts, mechanical damage accumulates in all of the samples, with earlier onset and greater growth of the damage for greater moisture exposure. Figure 4.3 shows the evolution of the mechanical damage variable ϕ^m alone to emphasize the differences between the mechanical damage in simulations with the same mechanical loading and different moisture loading.

4.3 Parametric Study

This section presents the results of parametric studies of the material constants governing moisture damage: the initial undamaged adhesion X_0^a and cohesion X_0^c and the rate parameters for adhesion k^a and cohesion k^c. Because the functions proposed for each here are the same, solutions are provided for one X_0^i and one k^i.

A series of simulations loads a material point to saturation and plots the declining bond strength and the moisture induced damage. Figures 4.4 and 4.5 show the bond strength X^i and damage variable ϕ^i as a function of time for various values of the initial bond strength X_0^i; this serves to shift the graphs vertically with no change in slope. Figures 4.6 and 4.7 show the bond strength X^i and damage variable ϕ^i as a function of time for various values of the moisture damage rate parameter k^i; this serves to change the slopes of the graphs.

4.4 Results

Several simulations' results show the function of the complete constitutive model, featuring viscoelasticity, viscoplasticity, mechanical damage, and moisture damage.

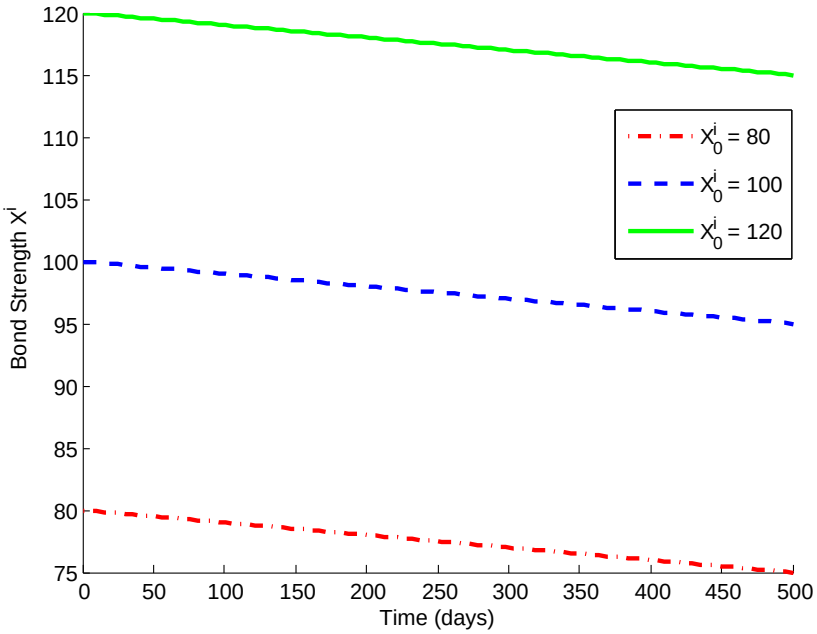

Figure 4.4 Effect of the initial undamaged strength X_0^i on the adhesive or cohesive strength X^i

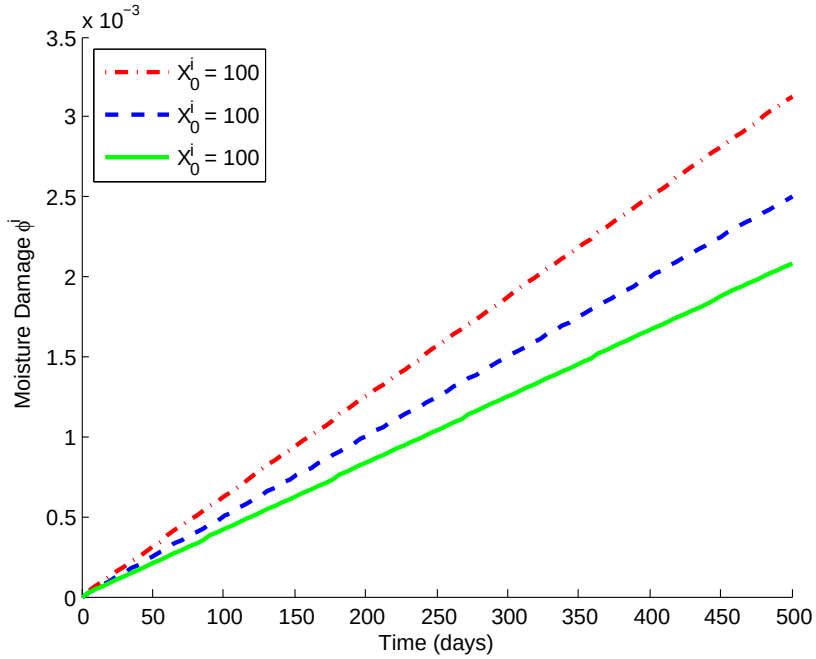

Figure 4.5 Effect of the initial undamaged strength X_0^i on the moisture damage variable ϕ^i

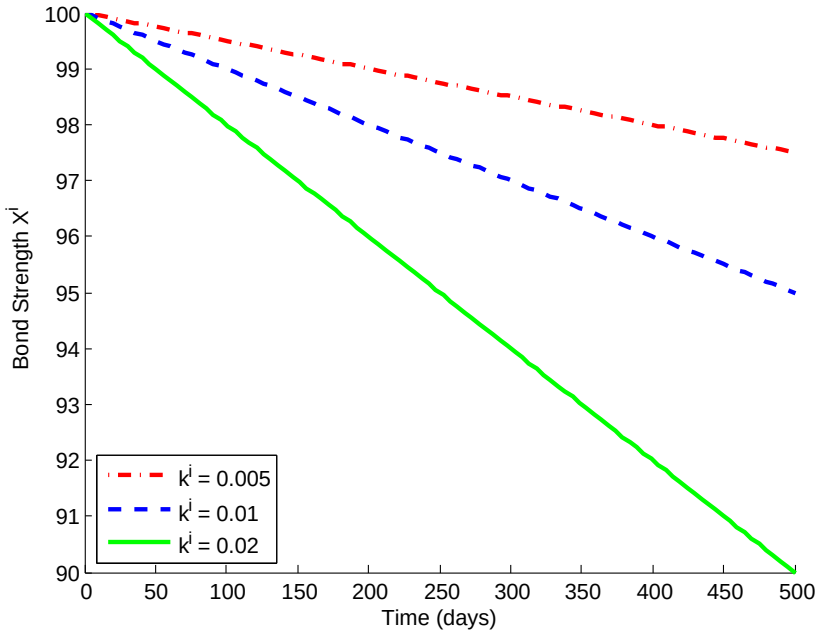

Figure 4.6 Effect of the moisture damage rate parameter k^i on the adhesive or cohesive strength X^i

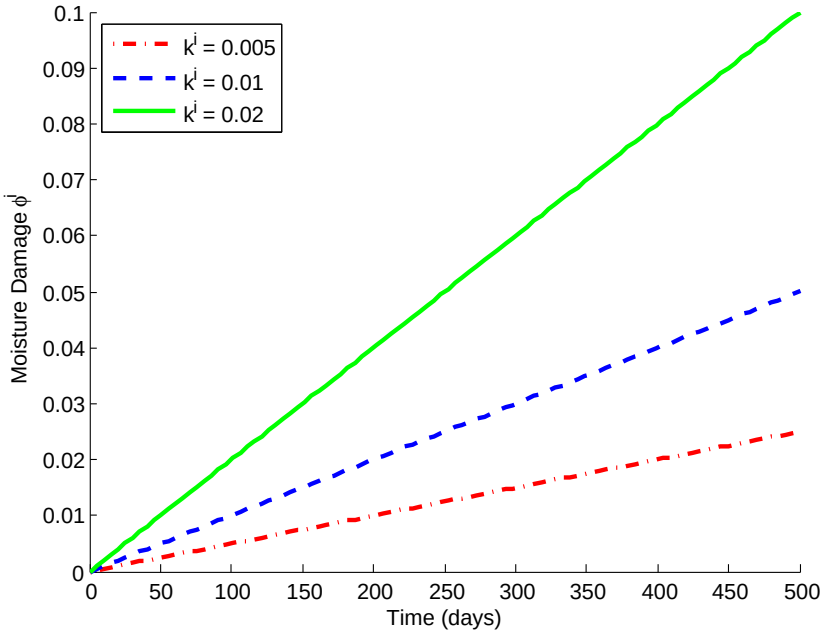

Figure 4.7 Effect of the moisture damage rate parameter k^i on the moisture damage variable ϕ^i

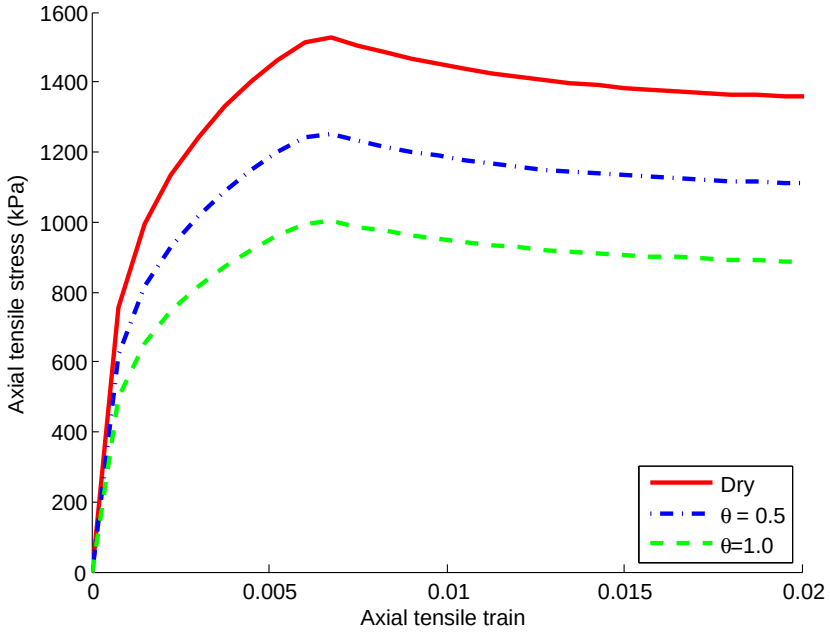

Figure 4.8 Stress–strain diagrams for constant uniaxial strain rate simulations for several moisture conditioning levels

The mechanical material parameters are as reported in past sections, and the moisture damage parameters are as follows: $X_0^a = 100.0$, $k^a = 0.01$, and $k^c = 0$ (i.e. there is no cohesive moisture damage).

4.4.1 Constant strain rate simulations

Figures 4.8 and 4.9 show the results of constant strain rate tests with different moisture exposures. The normalized moisture content θ is held constant for 2000 s and then the material is loaded at constant strain rate $\dot{\epsilon} = 0.0015\,\mathrm{s}^{-1}$. Note the effect of moisture damage, causing the material to become weaker and less stiff. Damage grows due to the presence of moisture and accelerates due to mechanical loading.

4.4.2 Constant stress rate simulations

Figure 4.10 shows the stress–strain curves for constant compressive stress rate simulations with different moisture levels. The material is subjected to the moisture

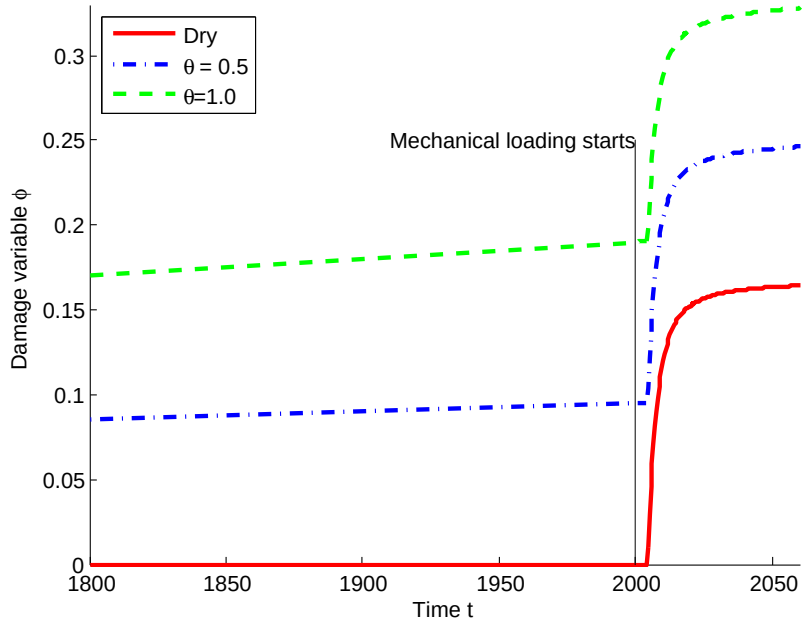

Figure 4.9 Damage growth for constant uniaxial strain rate simulations for several moisture conditioning levels

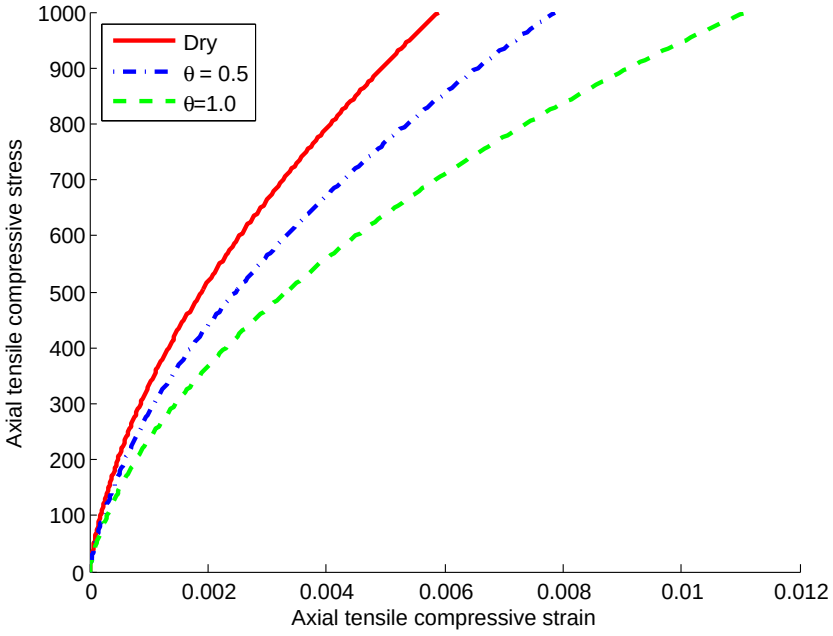

Figure 4.10 Stress–strain diagrams for constant uniaxial stress rate simulations for several moisture conditioning levels

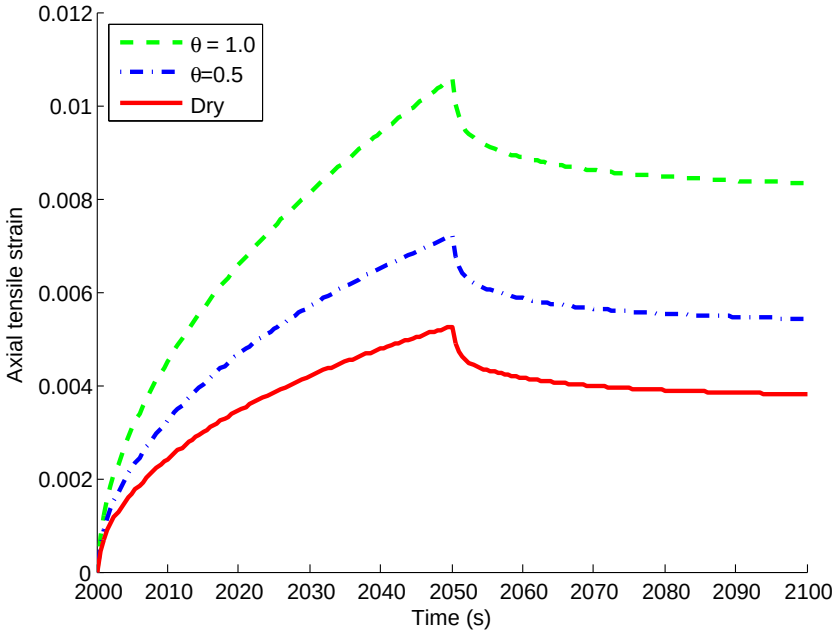

Figure 4.11 Strain vs. time for tensile creep–recovery simulations for several moisture conditioning levels

content specified for 2000 seconds and then subjected to a compressive stress at constant rate $\dot{\sigma} = 10\,\frac{\text{kPa}}{\text{s}}$.

4.4.3 Creep–recovery simulations

Figure 4.11 shows the strain response due to constant tensile stress $\sigma = 500\,\text{kPa}$ for 50 seconds then allowed to recover with the load removed for 50 seconds, all after 2000 seconds of moisture exposure at various levels.

5 CONCLUSION

5.1 Summary

The presented model captures the whole mechanical response of an asphalt mix subjected to mechanical and moisture loads using a continuum model. The nonlinear viscoelastic character of the reversible deformations is modeled using Shapery's theory. The viscoplastic character of the rate-dependent permanent deformations is modeled using Perzyna viscoplasticity, with a modified Drucker–Prager yield surface used to capture the dependence on state of stress anticipated for asphalt concrete and with a nonassociated flow rule to describe the appropriate volumetric viscoplastic response.

Damage is described due to extreme mechanical loads and due to moisture. The mechanically-induced damage model predicts degradation due to the same modified Drucker–Prager surface used for viscoplasticity with an exponential damage evolution function. Rate-dependence of mechanical damage is presented and a basic adaptation of the model is provided. Moisture-induced damage is treated realistically as two mechanisms: degradation of the adhesive bond between the mastic and aggregates and degradation of the cohesive strength of the mastic. The moisture-induced damage model is formulated in a novel way, accounting for the gradual, irreversible degradation of a mix using continuum damage mechanics.

This model is the first continuum model to capture all facets of realistic asphalt mix response, as described. One major simplification within the proposed model is anisotropy; all effects are assumed to be isotropic. In the case of moisture-induced damage this may be realistic, but it is at least somewhat unphysical in the mechanical laws. This assumption is made to keep from overcomplicating the model, and can be relaxed if experiments show anisotropy effects are important.

The nonlinear-viscoelastic–viscoplastic–damage model is implemented numerically for solving 3D and 2D plane strain problems with arbitrary geometries in the finite element method, using a UMAT user subroutine for the finite element code Abaqus. The presented simulation results show the meaning and effect of the various material parameters governing the nonlinear viscoelastic, viscoplastic, and damage behavior in the parametric studies, and show the predicted response for various simulated tests to match the qualitative behavior to experiments.

5.2 Future Work

Fitting experimental data to the model is a nontrivial task, due to the large number of material parameters and their inter-coupling in tests. Work is currently underway at Texas A&M University to develop a systematic way to fit all material parameters in the proposed model for a given asphalt mix.

It has been acknowledged that damage for asphalt concrete has a rate-dependent character. The model presented here describes damage in a way that is analogous to plasticity, with only an *ad hoc* rate dependence in its parameters. It is possible to formulate damage analogous to viscoplasticity to include rate effects (Voyiadjis et al. 2004), which would be much more robust and potentially provide an accurate description of mechanically-induced damage under a wide range of loading conditions.

REFERENCES

Abu Al-Rub, R.K.: Material length scales in gradient-dependent plasticity/damage and size effects: Theory and computation. PhD dissertation, Louisiana State University, Baton Rouge, Louisiana (2004)

Abu Al-Rub, R.K., Voyiadjis, G.: On the coupling of anisotropic damage and plasticity models for ductile materials. International Journal of Solids and Structures **40**, 2611–2643 (2003)

Abu Al-Rub, R.K., Voyiadjis, G.: Gradient-enhanced coupled plasticity-anisotropic damage model for concrete fracture: computational aspects and applications. International Journal of Damage Mechanics (2009). In press

Airey, G., Rahimzadeh, B., Collop, A.C.: Linear viscoelastic limits of bituminous binders. Journal of Associated Asphalt Paving Technologists **17**, 89–115 (2002a)

Airey, G., Rahimzadeh, B., Collop, A.C.: Viscoelastic linearity limits for bituminous materials. Materials and Structures **36**(10), 643–647 (2002b)

Airey, G., Rahimzadeh, B., Collop, A.C.: Linear rheological behavior of bituminous paving material. Journal of Materials in Civil Engineering **16**, 212–220 (2004)

ASTM: Standard test method for indirect tension test for resilient modulus of bituminous mixtures. In: Test Procedure D, E 380-91a. ASTM International, West Conshohocken, Pennsylvania (1995).

Bhasin, A.: Development of methods to quantify bitumen-aggregate adhesion and loss of adhesion due to water. PhD dissertation, Texas A&M University, College Station, Texas (2006)

Bhasin, A., Masad, E., Little, D., Lytton, R.: Limits on adhesive bond energy for improved resistance of hot mix asphalt to moisture damage. Transportation Research Record **1970**, 3–13 (2006)

Caro, S., Masad, E., Bhasin, A., Little, D.: Moisture susceptibility of asphalt mixtures, Part 1: Mechanisms. International Journal of Pavement Engineering **9**, 81–98 (2008a)

Caro, S., Masad, E., Bhasin, A., Little, D.: Moisture susceptibility of asphalt mixtures, Part 2: Characterisation and modeling. International Journal of Pavement Engineering **9**, 99–114 (2008b)

Chehab, G., Kim, Y.R., Schapery, R., Witczak, M., Bonaquist, R.: Characterization of asphalt concrete in uniaxial tension using a viscoelastoplastic model. Journal of Associated Asphalt Paving Technologists **72**, 326–370 (2003)

Chen, J., Lin, K., Young, S.: Effects of crack width and permeability on moisture-induced damage of pavements. Journal in Materials in Civil Engineering **16**(3), 276–282 (2006)

Cheung, C., Cebon, D.: Deformation mechanisms of pure bitumen. Journal of Materials in Civil Engineering **9**, 117–129 (1997)

Chiarelli, A., Shao, J., Hoteit, N.: Modeling of elastoplastic damage behavior of a claystone. International Journal of Plasticity **19**(1), 23–45 (2003)

Cicekli, U., Voyiadjis, G., Abu Al-Rub, R.K.: A plasticity and anisotropic damage model for plain concrete. International Journal of Plasticity **23**(10–11), 1874—1900 (2007)

Collop, A., Scarpas, A., Kasbergen, C., de Bondt, A.: Development and finite element implementation of stress-dependent elastoviscoplastic constitutive model with damage for asphalt. Transportation Research Record **1832**, 96–104 (2003)

Copeland, A.: Moisture in asphalt pavements in the United States: A financial perspective. First International Workshop on Moisture Damage. Delft, The Netherlands (2005)

Dessouky, S.: Multiscale approach for modeling hot mix asphalt. PhD dissertation, Texas A&M University, College Station, Texas (2005)

Di Benedetto, H., Mondher, N., Sauzeat, C., Olard, F.: Three-dimensional thermo-viscoplastic behavior of bituminous materials. Road Material Pavement **8**, 285–316 (2007)

Field, F., Phang, W.: Stripping in asphaltic concrete mixes, observations and test procedures. Canadian Technical Asphalt Association **12**, 61–68 (1967)

Grenfell, J., Collop, A., Airey, G., Taherkhani, H., Scarpas, A.T.: Deformation characterisation of asphalt concrete behaviour. In: Proceedings of the AAPT 2008, pp. 1–34. Engineers' Soc. of Western Pennsylvania, Philadelphia (2008)

Ha, K., Schapery, R.: A three-dimensional viscoelastic constitutive model for particulate composites with growing damage and its experimental validation. International Journal of Solids and Structures **35**(26–27), 3497–3517 (1998)

Haj-Ali, R.M., Muliana, A.H.: Numerical finite element formulation of the Schapery nonlinear viscoelastic material model. International Journal of Numerical Methods in Engineering **59**(1), 25–45 (2004)

Huang, C.W.: Development and numerical implementation of nonlinear viscoelastic–viscoplastic model for asphalt materials. PhD dissertation, Texas A&M University, College Station, Texas (2008)

Huang, C.W., Masad, E., Muliana, A.H., Bahia, H.: Nonlinearly viscoelastic analysis of asphalt mixes subjected to shear loading. Mechanics of Time-Dependent Materials **22**, 91–110 (2007)

Kachanov, L.: On the creep fracture time. Izv Akad, Nauk USSR Otd. Tech. **8**, 26–31 (1958)

Kachanov, L.: A simple technique of stress analysis in elastic solids with many cracks. International Journal of Fracture **28**, R11–19 (1985)

Kandhal, P.: Field and lab investigation of stripping in asphalt pavements: State-of-the-art. Transportation Research Record **1454**, 36–47 (1994)

Kassem, E.A.R.: Measurements of moisture suction in hot mix asphalt mixes. MS thesis, Texas A&M University, College Station, Texas (2006)

Kassem, E.A.R.: Compaction effects on uniformity, moisture diffusion, and mechanical properties of asphalt pavements. PhD dissertation, Texas A&M University, College Station, Texas (2008)

Kringos, N.: Modeling of combined physical-mechanical moisture induced damage in asphaltic mixes. PhD dissertation, Delft University, Delft, The Netherlands (2007)

Kringos, N., Scarpas, A.T.: Raveling of asphaltic mixes due to water damage: Computational identification of controlling parameters. Transportation Research Record **1929**, 79–87 (2005)

Kringos, N., Scarpas, A.T.: Physical and mechanical moisture susceptibility of asphaltic mixtures. International Journal of Solids and Structures **45**, 2671–2685 (2008)

Kringos, N., Scarpas, A.T., Copeland, A., Youtcheff, J.: Modeling of combined physical-mechanical moisture induced damage in asphaltic mixes – Part 2: moisture susceptibility parameters. International Journal for Pavement Engineering **9**, 129–151 (2008a)

Kringos, N., Scarpas, A.T., Kasbergen, C.: Three dimensional elasto-viscoplastic finite element model for combined physical-mechanical moisture induced damage in asphaltic mixes. Journal of Associated Asphalt Paving Technologists **76**, 495–524 (2007)

Kringos, N., Scarpas, A.T., Kasbergen, C., Selvadurai, A.: Modeling of combined physical-mechanical moisture induced damage in asphaltic mixes – Part 1: governing processes and formulations. International Journal for Pavement Engineering **9**, 115–128 (2008b)

Lemaitre, J.: Engineering Damage Mechanics: Ductile, Creep, Fatigue and Brittle Failures. Springer, Berlin (2005)

Lemaitre, J., Chaboche, J.L.: Mechanics of Solid Materials. Cambridge University Press, London (1990)

Levenberg, E., Uzan, J.: Triaxial small-strain viscoelastic-viscoplastic modeling of asphalt aggregate mixes. Mechanics of Time-Dependent Materials **8**(4), 365–384 (2004)

Little, D., Jones, D.: Chemical and mechanical mechanisms of moisture damage in hot mix asphalts pavements. In: Moisture Sensitivity of Asphalt Pavements: A National Seminar pp. 713–754 (2003)

Lu, Y., Wright, P.J.: Numerical approach of visco-elastoplastic analysis for asphalt mixtures. Journal of Computers and Structures **69**, 139–157 (1998)

Luo, R., Lytton, R.L.: Self-consistent micromechanics models of an asphalt mixture. In: Transportation Research Board 2009 Annual Meeting CD-ROM pp. 1–17 (2009)

Lytton, R., Masad, E., Zollinger, C., Bulut, R., Little, D.: Measurements of surface energy and its relationship to moisture damage. Technical Report FHWA/TX-05/0-4524-2, Texas Transportation Institute, College Station, Texas (2005)

Masad, E., Al-Omari, A., Lytton, R.: A simple method for predicting laboratory and field permeability of hot mix asphalt. Transportation Research Record **1970**, 55–63 (2006a)

Masad, E., Castelblanco, A., Birgisson, B.: Effects of air void size distribution, pore pressure, and bond energy on moisture damage. Journal of Testing and Evaluation **34**(1), 1–9 (2006b)

Masad, E., Dessouky, S., Little, D.: Development of an elastoviscoplastic micro-structural-based continuum model to predict permanent deformation in hot mix asphalt. International Journal of Geomechanics **7**, 119–130 (2007a)

Masad, E., Huang, C.W., Airey, G., Muliana, A.: Nonlinear viscoelastic analysis of unaged and aged asphalt binders. Construction and Building Materials **22**, 2170–2179 (2007b)

Masad, E., Zollinger, C., Bulut, R., Little, D., Lytton, R.: Characterization of HMA moisture damage using surface energy and fracture properties. Journal of the Association of Asphalt Paving Technologists **75**, 713–754 (2006c)

Nicholson, V.: Adhesion tension in asphalt pavements, its significance and methods applicable in its determination. Journal of the Association of Asphalt Paving Technologists **3**, 28–48 (1932)

Oeser, M., Moller, B.: 3d constitutive model for asphalt pavements. International Journal of Pavement Engineering **5**, 153–161 (2004)

Park, S., Schapery, R.: A viscoelastic constitutive model for particulate composites with growing damage. International Journal of Solids and Structures **34**(8), 931–947 (1997)

Park, S.W., Kim, Y.R., Schapery, R.A.: A viscoelastic continuum damage model and its application to uniaxial behavior of asphalt concrete. Mechanics of Materials **24**(4), 241–255 (1996)

Perl, M., Uzan, J., Sides, A.: Visco-elasto-plastic constitutive law for bituminous mixture under repeated loading. Transportation Research Record **911**, 20–26 (1983)

Perzyna, P.: The constitutive equations for rate-sensitive materials. Quarterly of Applied Mathematics **20**, 321–332 (1963)

Perzyna, P.: Fundamental problems in visco-plasticity. In: Chernyi, G. (ed.) Advances in Applied Mechanics, vol. 9, pp. 243–377. Academic Press, New York (1966)

Perzyna, P.: Thermodynamic theory of viscoplasticity. In: Yih, C.S. (ed.) Advances in Applied Mechanics, vol. 11, pp. 313–354. Academic Press, New York (1971)

Roels, S., Moonen, P., Proft, K.D., Carmeliet, J.: A coupled discrete-continuum approach to simulate moisture effects on damage processes in porous materials. Computer Methods in Applied Mechanics and Engineering **195**(52), 7139–7153 (2006)

Roy, S., Benjamin, M.: Modeling of permeation and damage in graphite/epoxy laminates for cryogenic fuel storage. Composites Science and Technology **64**(13–14), 2051–2065 (2004)

Roy, S., Xu, W.: Modeling of diffusion in the presence of damage in polymer matrix composites. International Journal of Solids and Structures **38**(1), 115–125 (2001)

Sadd, M., Parameswaran, D., Shukla, A.: Simulation of asphalt materials using finite element micromechanical model with damage mechanics. Transportation Research Record **1832**, 86–95 (2004)

Schapery, R.: On the characterization of nonlinear viscoelastic materials. Polymer Engineering and Science **9**(4), 295–310 (1969)

Schapery, R.: Nonlinear viscoelastic and viscoplastic constitutive equations with growing damage. International Journal of Fracture **97**, 33–66 (1999)

Seibi, A.C., Sharma, M.G., Ali, G.A., Kenis, W.J.: Constitutive relations for asphalt concrete under high rates of loading. Transportation Research Record **1767**, 111–119 (2001)

Sides, A., Uzan, J., Perl, M.: A comprehensive visco-elastoplastic characterization of sand-asphalt under compression and tension cyclic loading. Journal of Testing and Evaluation **13**, 49–59 (1985)

Simo, J., Hughes, T.: Computational Inelasticity, vol. 7. Springer, York, Pennsylvania (1998)

Sousa, J.B., Weissman, S., Sackman, J., Monismith, C.L.: A nonlinear elastic viscous with damage model to predict permanent deformation of asphalt concrete mixtures. Transportation Research Record **1384**, 80–93 (1993)

Sousa, J.B., Weissman, S., Sackman, J., Monismith, C.L.: Modeling permanent deformation of asphalt concrete mixtures. Journal of the Association of Asphalt Paving Technologists **63**, 224–257 (1994)

Tang, X., Whitcomb, J., Li, Y., Sue, H.J.: Micromechanics modeling of moisture diffusion in woven composites. Composites Science and Technology **65**(6), 817–826 (2005)

Tashman, L.: Microstructure viscoplastic continuum model for permanent deformation in asphalt pavements. PhD dissertation, Texas A&M University, College Station, Texas (2003)

Uzan, J.: Viscoelastic–viscoplastic model with damage for asphalt concrete. Journal of Materials in Civil Engineering **17**(5), 528–534 (2005)

Voyiadjis, G., Abu Al-Rub, R., Palazotto, A.: Thermodynamic formulations for non-local coupling of viscoplasticity and anisotropic viscodamage for dynamic localization problems using gradient theory. International Journal of Plasticity **20**(6), 971–1038 (2004)

Voyiadjis, G., Kattan, P.: Advances in Damage Mechanics: Metals and Metals Matrix Composites. Elsevier, Oxford (1999)

Zollinger, C.: Application of surface energy measurements to evaluate moisture susceptibility of asphalt and aggregates. MS thesis, Texas A&M University, College Station, Texas (2005)

APPENDIX A
MICROMECHANICAL SIMULATIONS

Throughout this thesis, a continuum model is used, because continuum models are able to provide simulations of realistic engineering structures (such as a section of a roadway) for much less computational expense than microscale models. However, continuum models are fundamentally incapable of describing effects that are occurring at a scale smaller than continuity is imposed. The effects of composition and geometry at a microscale in asphalt concrete mixes lead to their continuum properties. Micromechanical modeling is beyond the scope of this thesis, but a few simulations are performed and their results presented here to show the model's fitness for micromechanical computational models.

Though the material model presented in this thesis is developed to model asphalt concretes as continua, it is extremely well-suited to asphalt mastic, which exhibits time-dependent recoverable and irrecoverable deformations, and degrades with loading and moisture exposure. The response of aggregates is usually very stiff and time-table, and may be modeled with a simple linear elastic material law. (Recent work by Luo and Lytton (2009) suggests a viscoelastic law might be more appropriate for aggregates, possibly due to binder absorption in the aggregates. This or any other accessible material model for aggregate would also be simple to incorporate in a finite element simulation if necessary.)

For these simulations, finite element meshes were constructed with three types of regions: aggregates, asphalt mastic bulk, and asphalt mastic in the aggregate–mastic bond region, and all are given different material properties. The aggregates are modeled as isotropic linear elastic material with Young's modulus $E_{\text{agg}} = 1\,\text{GPa}$ and

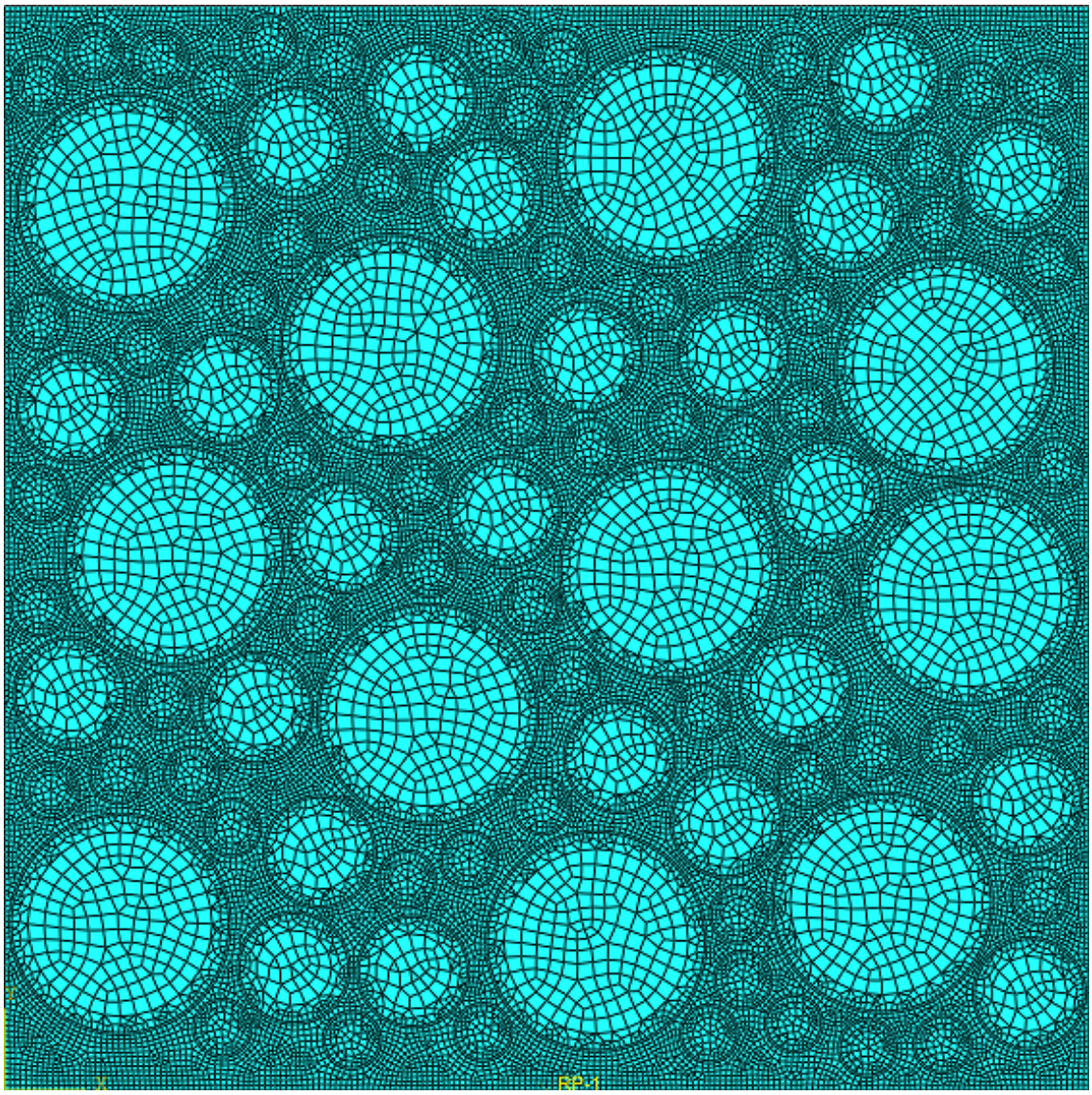

Figure A-1 Undeformed finite element mesh for micromechanical simulations

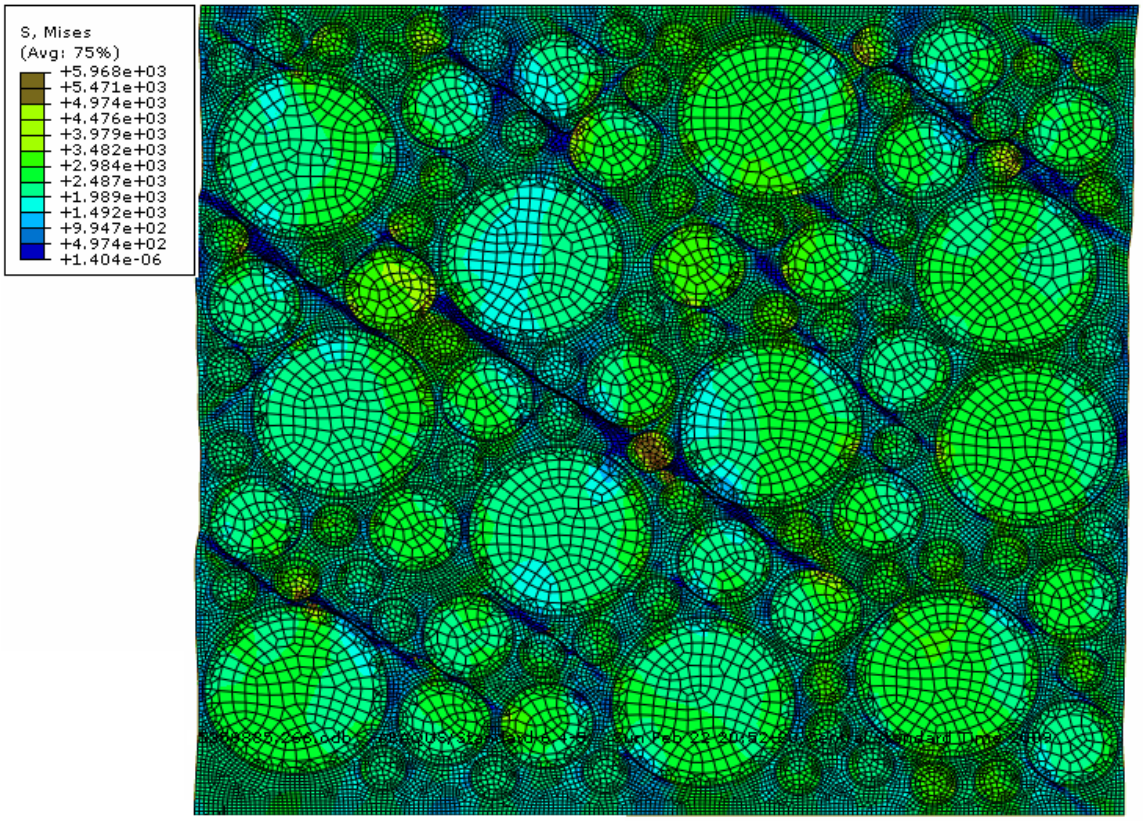

Figure A-2 Von Mises stress distribution due to compressive loading

Poisson's ratio $\nu_{\text{agg}} = 0.16$, and the mastic is modeled with the material parameters in Tables 2.1, 2.2, and 3.1. Additionally for the mastic, $X_0^a = 100$, $X_0^c = 100$, $k^c = 0.01$, and $k^a = 0.02$ in the adhesive zones and $k^a = 0$ outside the cohesive zones. The normalized diffusivities for the mastic and aggregate are $10^{-5}\,\text{m}^2\text{s}^{-1}$ and $10^{-10}\,\text{m}^2\text{s}^{-1}$, respectively.

A.1 Dry Simulations

Figure A-1 shows a sample of a mesh: the round, relatively course meshes are aggregates, one ring of elements surrounding them are interface-zone mastic, and the remaining elements are bulk mastic. Plane-strain linear finite elements model all regions.

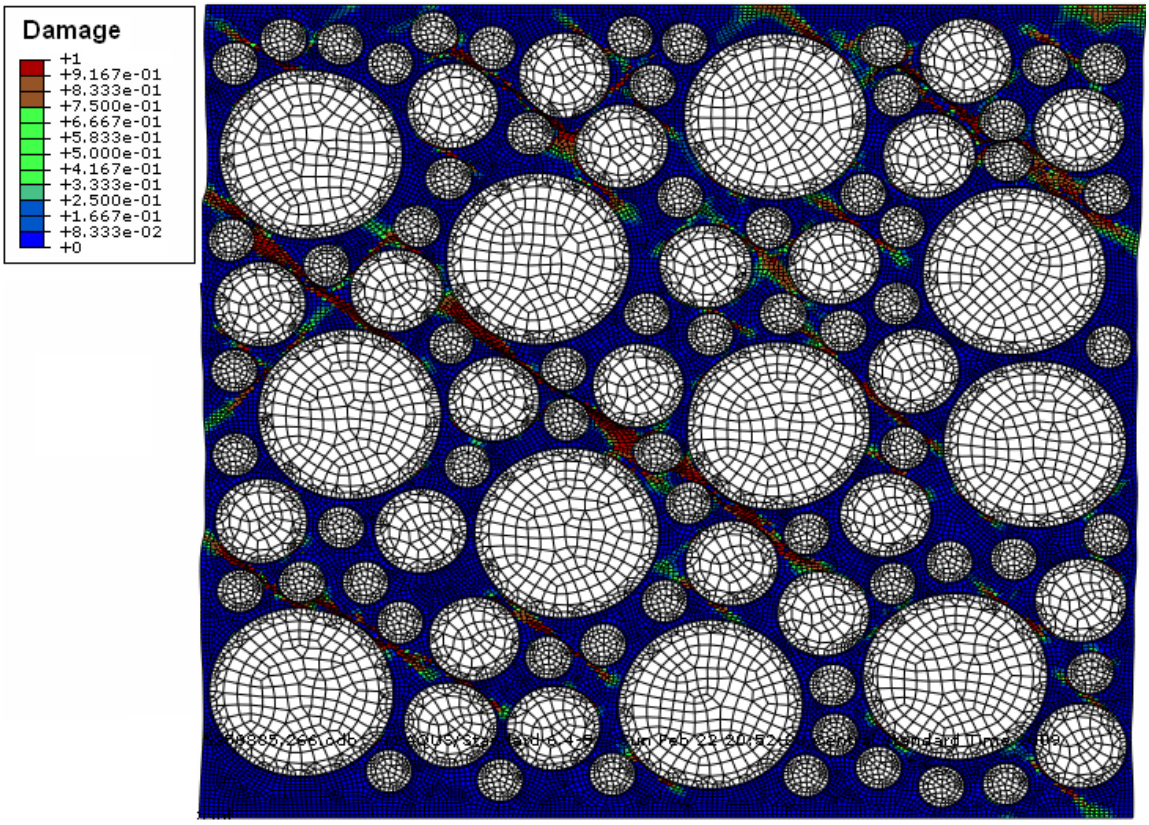

Figure A-3 Damage distribution due to compressive loading

Figures A-2 and A-3 are contour plots showing the distribution of stress and damage due to compressive loading at constant average strain rate $\dot{\epsilon} = 0.0015\,\mathrm{s}^{-1}$, and through the simulation, the geometry of the body causes stress to concentrate in some parts of the mesh. When the stress becomes very high, the material sustains damage, and becomes less stiff. Corresponding to this loss in stiffness, the formerly high-stress material 'attracts' less load, and the areas with high deformation have small values of stress in Figure A-2 and high values of damage in Figure A-3.

Figure A-4 is the resulting average stress–average strain diagram resulting from the load–displacement relation of the body. The most significant thing about this plot is that it exhibits yielding and softening, but in a qualitatively different way

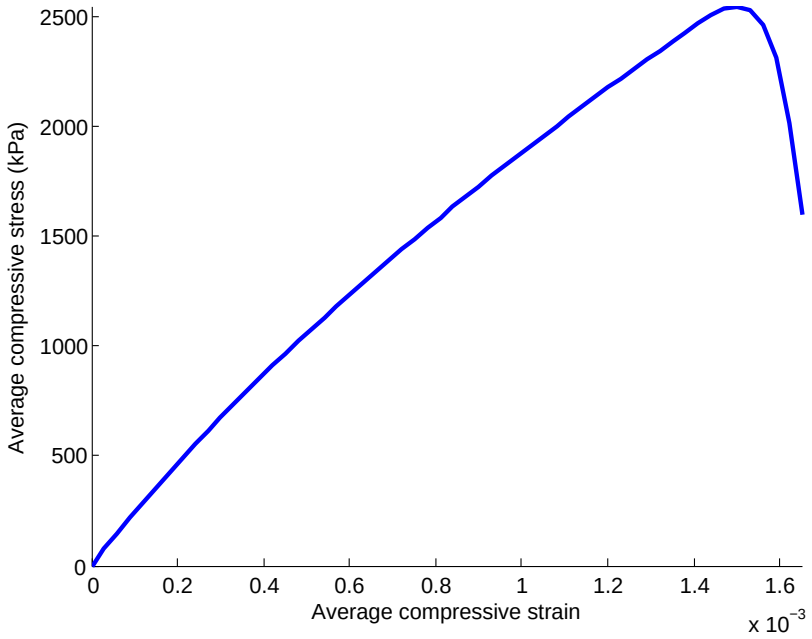

Figure A-4 Average stress–average strain diagram due to compressive loading

than shown in the plots of Section 3.

Figures A-5, A-6, and A-7 are plots with the same meanings as Figures A-2, A-3, and A-4, but due to *tensile* constant average strain rate tests at average strain rate $\dot{\epsilon} = 0.00025\,\mathrm{s}^{-1}$. The average stress–average strain diagram Figure A-7 does not report values into the softening regime.

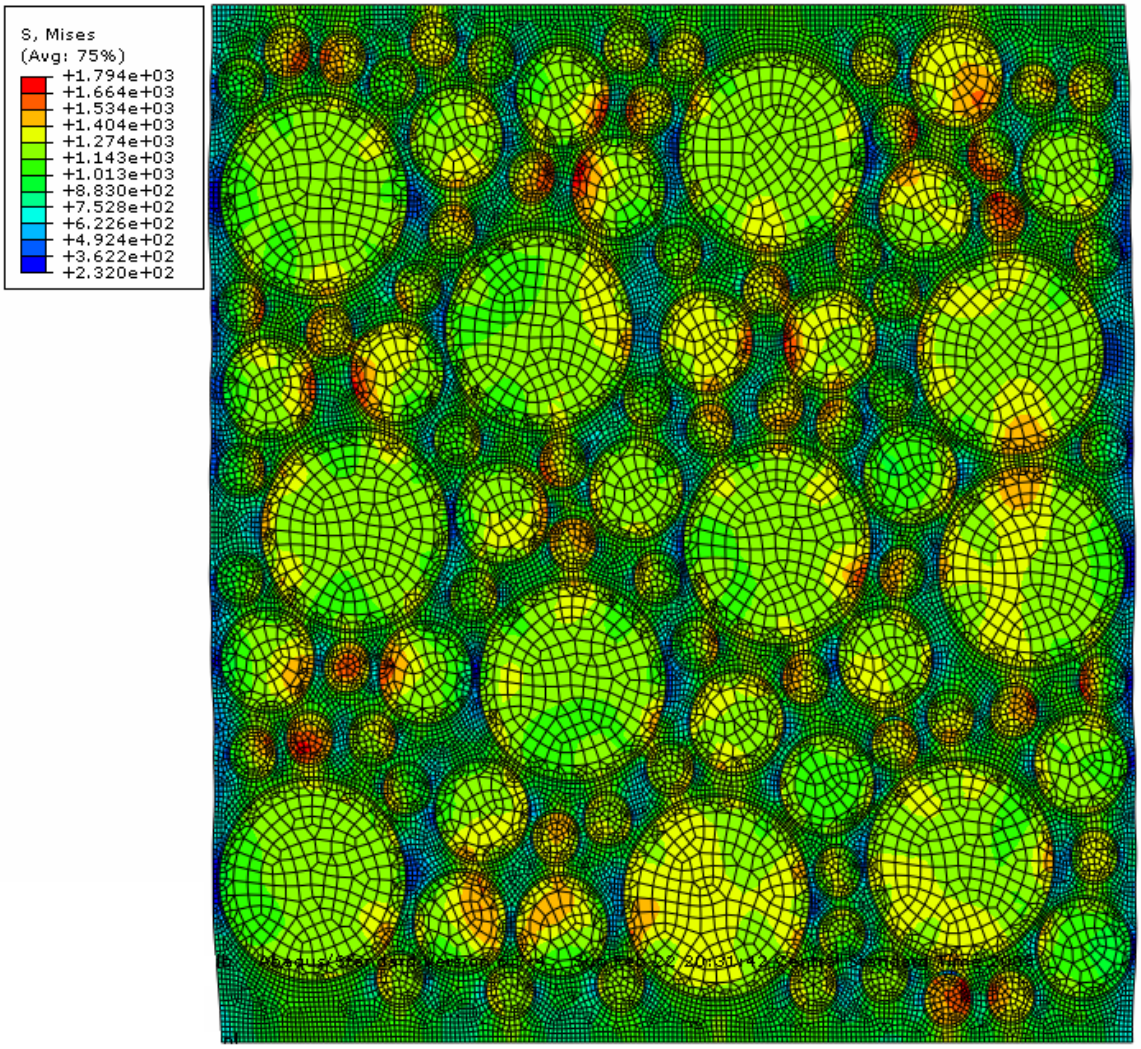

Figure A-5 Von Mises stress distribution due to tensile loading

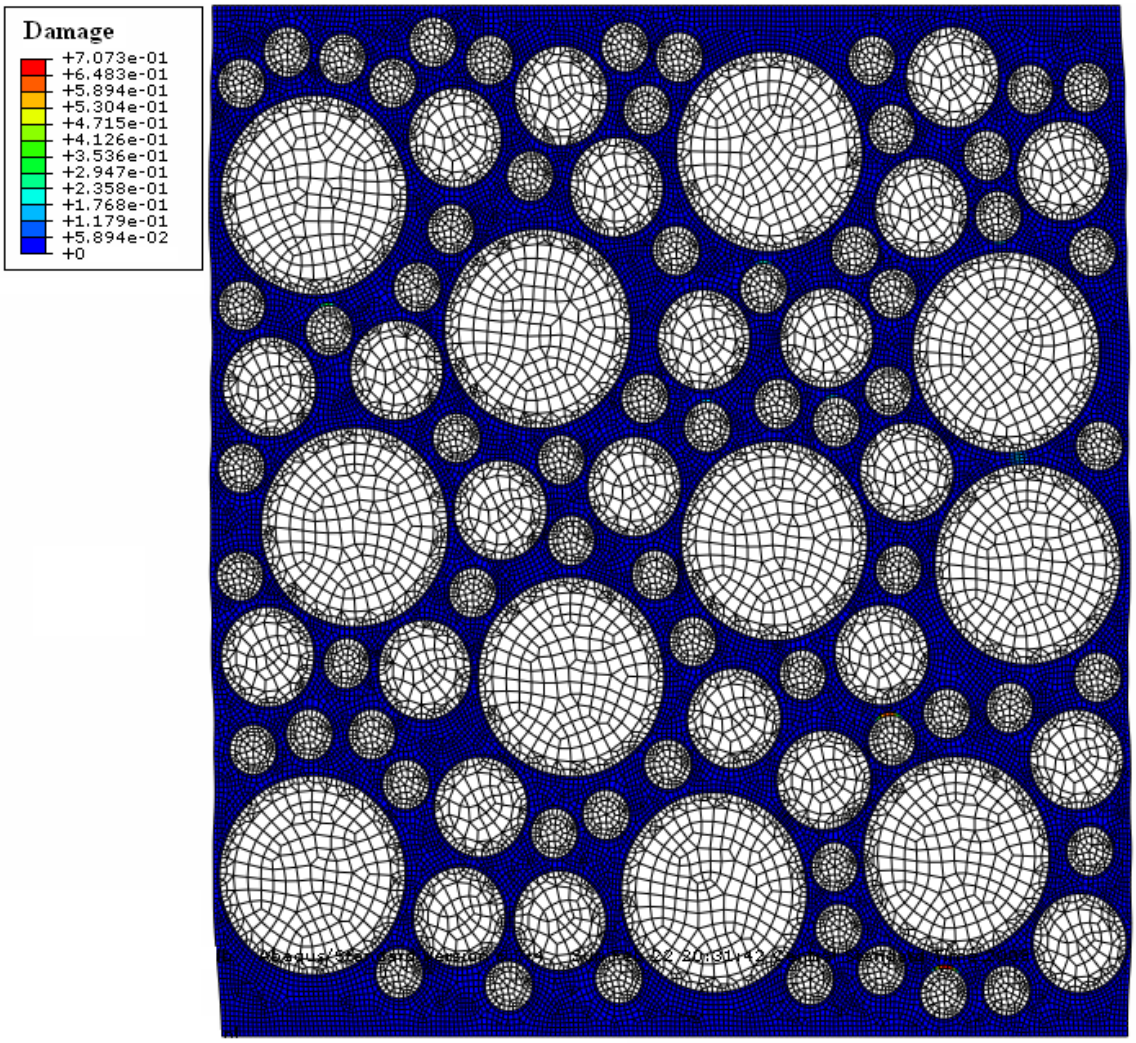

Figure A-6 Damage distribution due to tensile loading

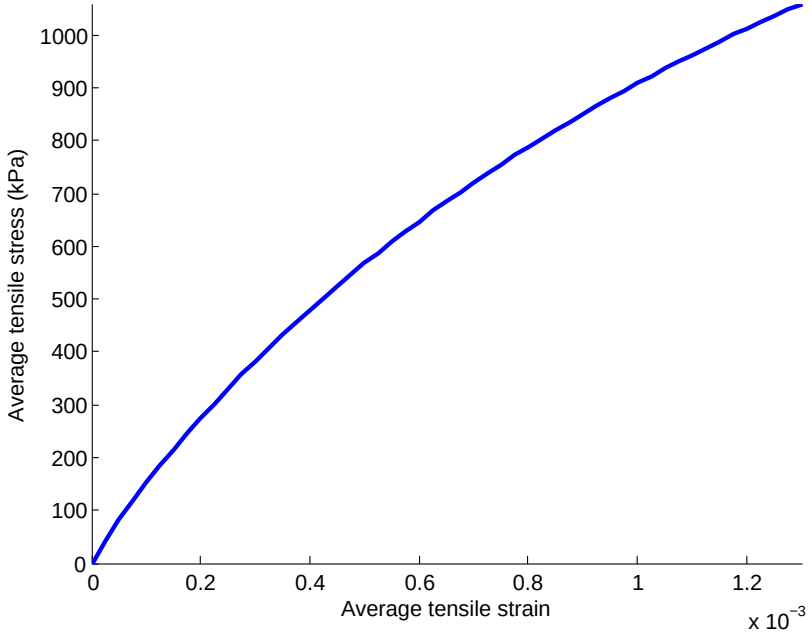

Figure A-7 Average stress–average strain diagram due to compressive loading

A.2 Moisture-Affected Simulations

Several figures show the result of a simulation featuring both moisture and mechanical loading. The body is subjected to constant normalized moisture content $\theta = 1.0$ on its top edge and $\theta = 0.0$ on its bottom edge for 2000 seconds before being loaded in compression at constant average strain rate $\dot{\epsilon} = 0.0015\,s^{-1}$. Figure A-8 shows the final moisture distribution, which leads to the moisture-induced damage.

Figure A-9 depicts the stress distribution after some mechanical loading; stress is concentrated due to geometry and moisture damage effects. Figure A-10 is the total damage distribution and Figures A-11, A-12, and A-13 are the corresponding mechanical, cohesive moisture, and adhesive moisture damage distributions. Compare

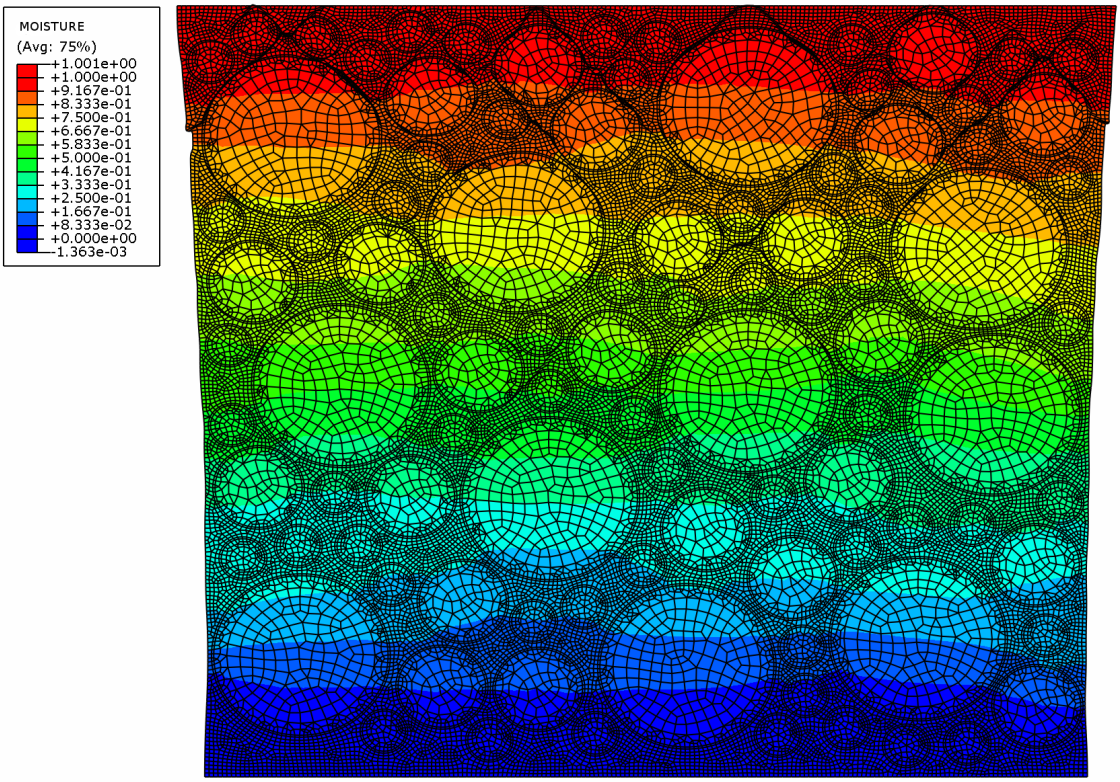

Figure A-8 Final moisture distribution

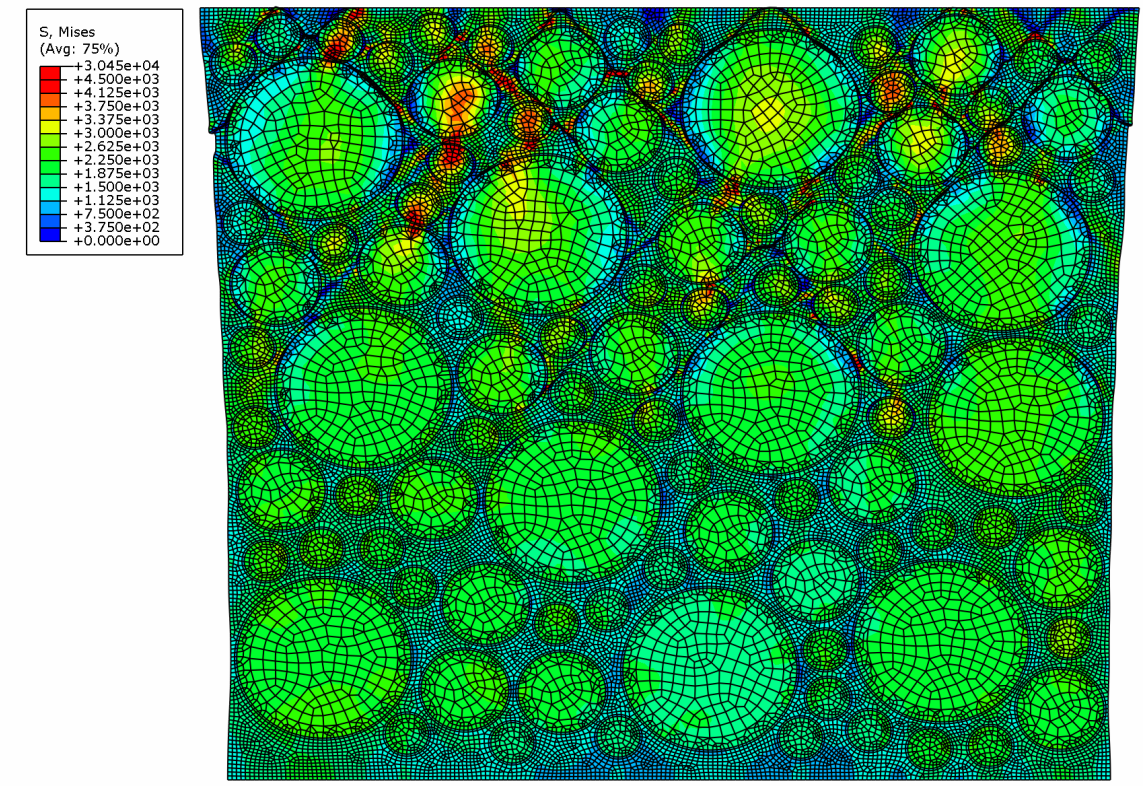

Figure A-9 Von Mises stress distribution due to moisture and compressive loading

Figure A-3 to Figure A-11 on page 82: the degrading presence of moisture has greatly changed the damage's location and distribution. Figure A-3 shows large, continuous damaged regions (cracking) whereas the moisture-exposed body in Figure A-11 shows more compact, isolated, concentrated damaged regions surrounding the aggregates (raveling).

Figures A-12 and A-13 show that the model performs as expected: moisture-induced damage occurs to a greater degree in the areas closer to moisture-exposed surfaces. The loss of strength at the aggregate-mastic interface in particular is severe, and the interface zone attracts much of the degradation as seen by the total damage (Figure A-11).

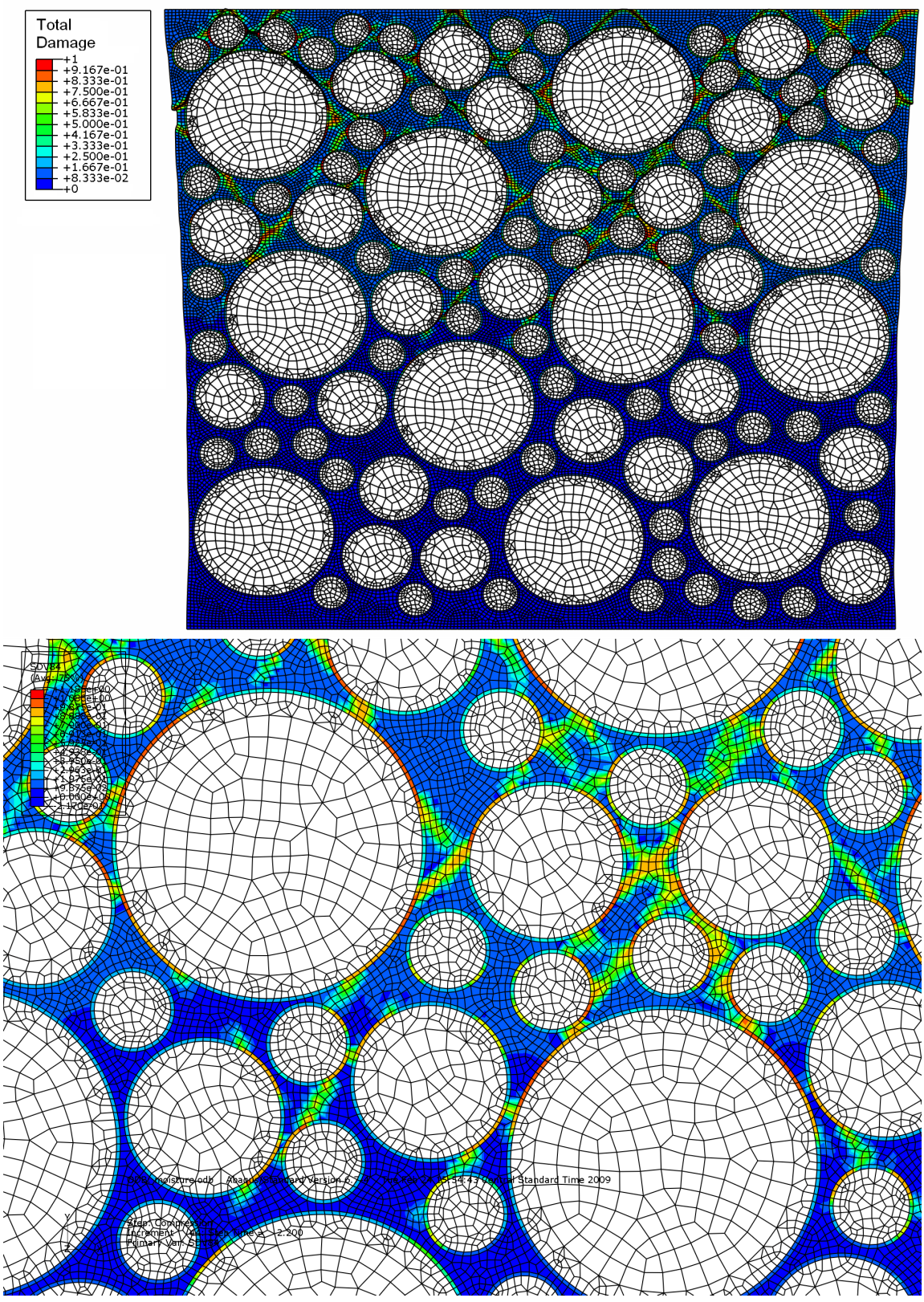

Figure A-10 Damage distribution due to moisture and loading (whole body and inset)

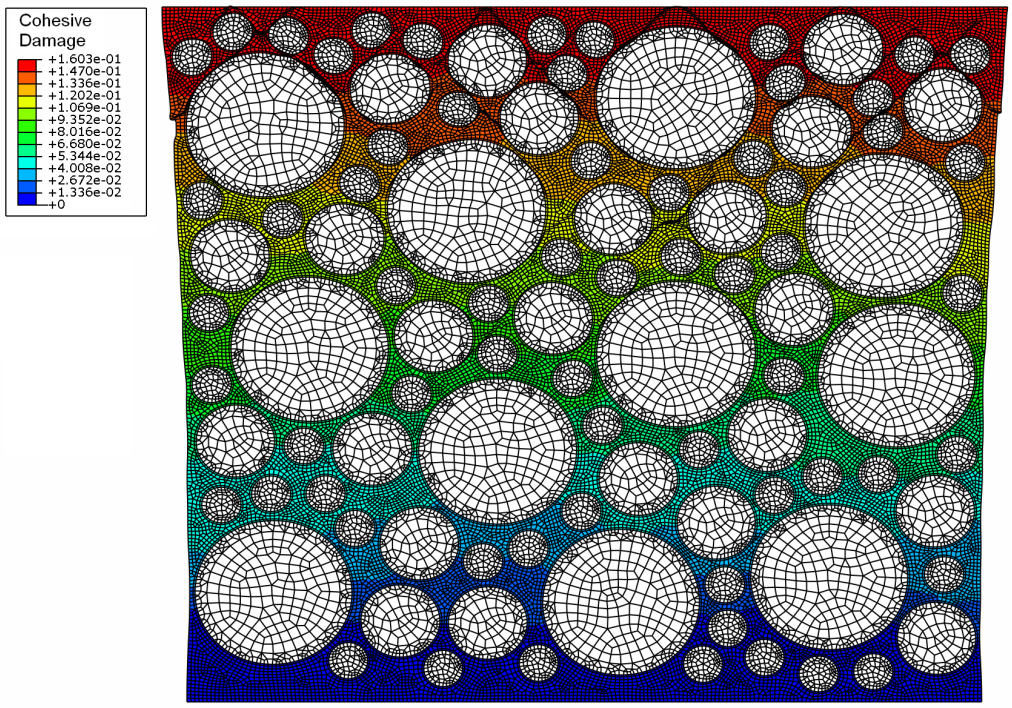

Figure A-11 Cohesive strength damage due to moisture

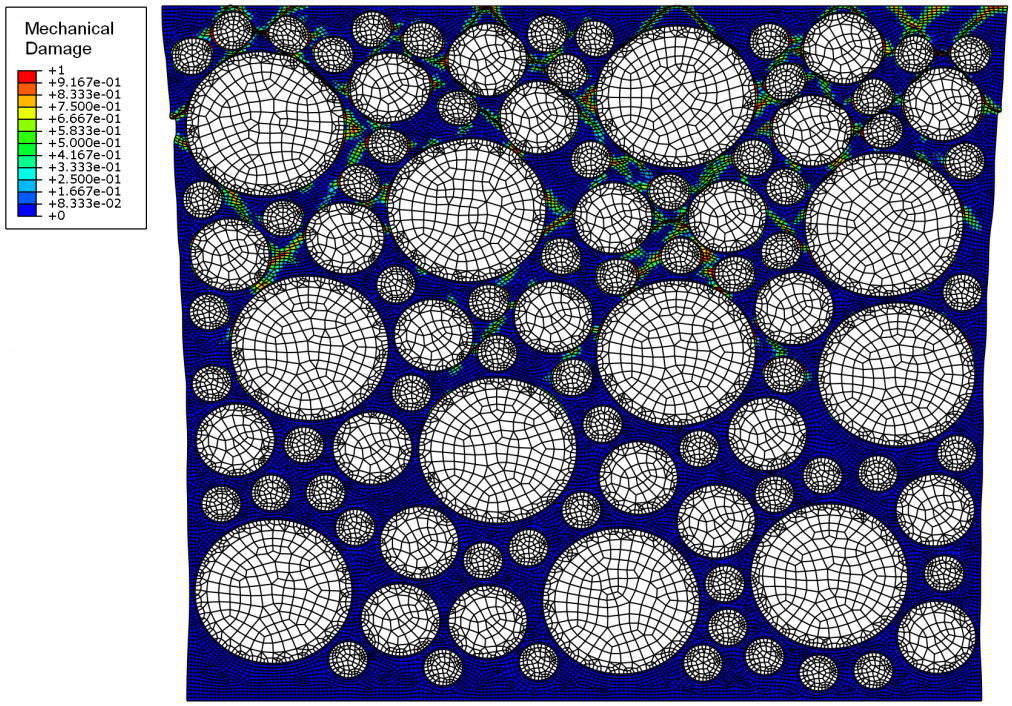

Figure A-12 Mechanical damage distribution due to loading with moisture effects

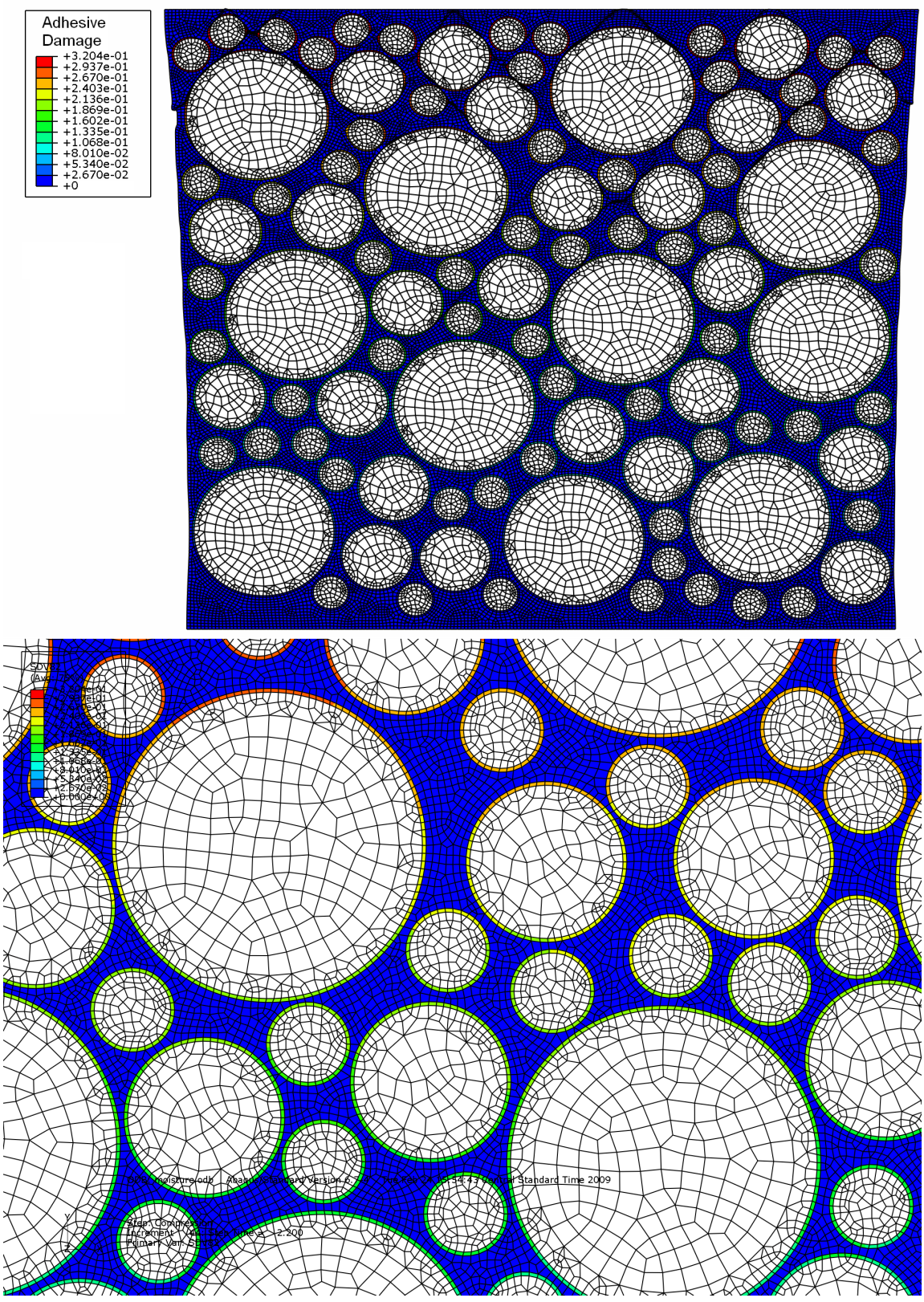

Figure A-13 Adhesive bond strength damage due to moisture (whole body and inset)

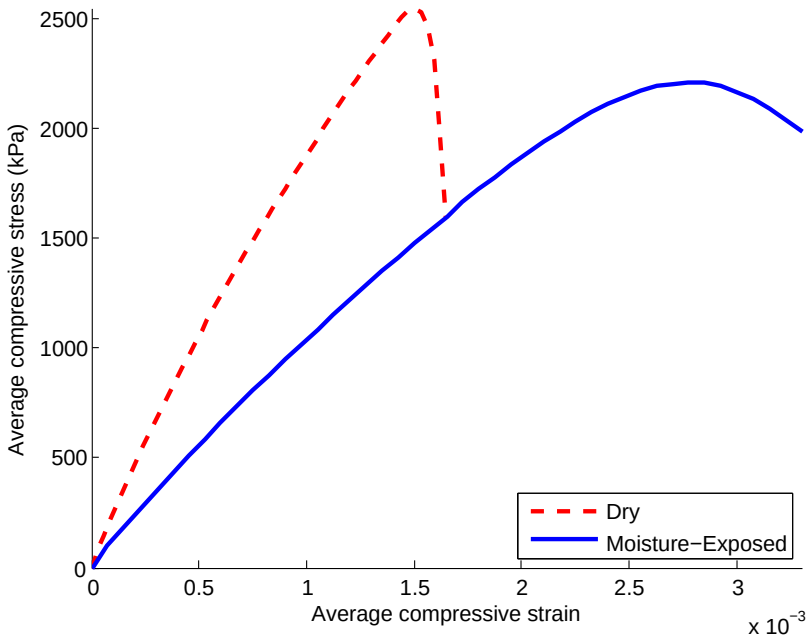

Figure A-14 Average stress–average strain diagram due to compressive loading, with and without moisture present

Figure A-14 is the average stress–average strain diagram for the body, plotted for the moisture damaged body and for dry material. The composite stiffness and ultimate strength are reduced in the moisture-exposed case.

A.3 Conclusions

The results presented here show that the mechanical/moisture damaged non-linear-viscoelastic–viscoplastic material model presented in this thesis is well-suited to microscale simulations of asphalt concrete. Future models can use this model with experimentally-determined material parameters for the constituents to predict the bulk response of asphalt concrete.

VITA

Michael Anthony Graham received his Bachelor of Science degree in civil engineering with a specialty in structures and a minor in mathematics from Texas A&M University at College Station, TX in May 2007. This thesis marks the completion of the requirements for his Master of Science degree in civil engineering with a specialty in structures from Texas A&M University, received in August 2009.

Michael is an experienced engineering researcher and structural engineering consultant and an Engineer in Training in the state of Texas. Contact Michael by postal mail at the address

Michael Graham
3135 TAMU
College Station, TX 77843–3135
USA

or by email at the address mikegraham@gmail.com.